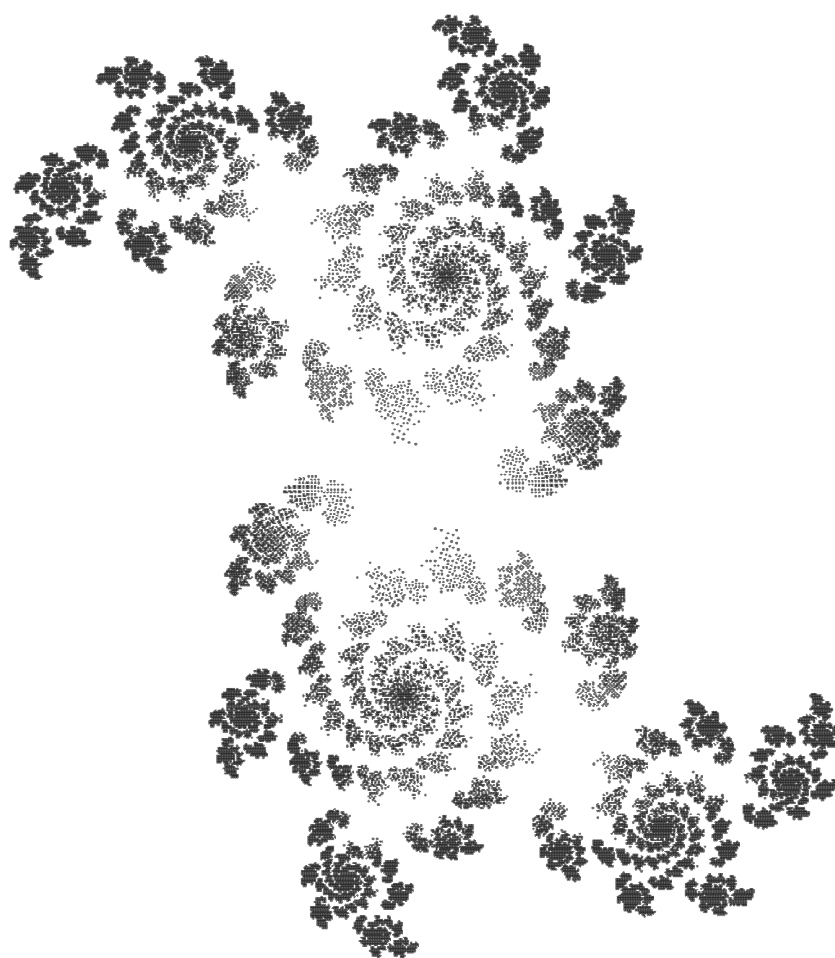


Quantum Control of Interacting Spins

Master's Thesis



Yuning Zhang

Quantum Control of Interacting Spins

THESIS

submitted in partial fulfillment of the
requirements for the degree of

MASTER OF SCIENCE

in

APPLIED PHYSICS

by

Yuning Zhang



QuTech

Dobrivitski Group
QuTech, Delft University of Technology
Delft, the Netherlands

© 2022 Yuning Zhang.

Cover picture: Fractal Flower.

Quantum Control of Interacting Spins

Author: Yuning Zhang

Abstract

Quantum decoherence is one of the most substantial challenges on the way to fully-fledged quantum technology. Noise mitigation based on dynamical control techniques, aside from error correction, is known to be another effective approach to protect qubits from decoherence. In this thesis, we studied the dynamics of a spin qubit interacting with a disordered spin bath in different dimensions. By modeling the environmental spins from fundamental dipolar couplings and employing Monte-Carlo simulations, this research provides an insight into the precise driving and control of a noisy spin qubit, including the noise distribution, decoherence mechanism, driving error, gate fidelity, and performance of dynamical decoupling sequence. This knowledge will be helpful to the future design of noise-robust quantum gates and potential decoupling protocols of spin qubits.

Thesis Committee:

University Supervisor: Dr. Vatcheslav V. Dobrovitski
Committee Member: Prof. dr. A. F. Sander Otte
Committee Member: Prof. dr. Yaroslav M. Blanter

Preface

Information is physical.

–Rolf Landauer

The universe as a quantum computer.

–Seth Lloyd

Nature exists at the edge of of order and chaos.

– Mitchell Waldrop

Many years later, I can still remember that starry night in a small mountain village of Shandong, grandmother was cooking in the room, while I was gazing at the galaxy on the roof, shocked by the magnificent beauty of the universe. I chose science in high school, with a dream that I can understand the world one day. Today, I am still studying physics, on the other side of the world, feeling lucky that I can still be surprised by the fantastic puzzles of nature. Yet, the more I learned, the more I realized how insignificant is my understanding of nature. After so many years, I stand at the cross land of quantum, information, and complexity, having no idea about where to go.

Whatever, I am going to finish my little thesis today. At the end of this long journey, I want to thank my family, who fund my whole master study. Without their love and support, I would never be here. Also the best thanks to my good friends, they are always by my side in these tough times. At last, I want to sincerely express my gratitude to my supervisor, Dr. Dobrovitski, for his guidance, patience, and encouragement. His training and professional knowledge made this thesis possible.

– Yuning Zhang,
May 11th, 2022

Contents

Preface	iii
Contents	v
1 Introduction	1
1.1 A Brief History of Quantum Control	1
1.2 Quantum Control for Quantum Information Processing	2
1.3 Many-body Noise and Control of Interacting Spins	3
2 Spin Qubit in Bath	5
2.1 Spin as a Qubit	5
2.2 Cluster of Interacting Spins	6
2.3 Hamiltonian in the Rotating Frame	8
2.4 Thermalized Spin Bath	9
2.5 Decoherence	10
2.6 Equivalent Noise	11
3 Ensemble of Spins	13
3.1 Ensemble of Disorder Realizations	13
3.2 Averaged Dephasing in Dilute Ensemble	16
3.3 Nondimensionalization	19
3.4 Normalized Coherence Time	20
4 Driving a Bath-Coupled Qubit	25
4.1 Control Hamiltonian	25
4.2 Rabi Driving with Effective Noise	26
4.3 Rabi Driving from Numerical Sampling	28
4.4 Damping of Continuous Driving	29
5 Noisy Quantum Gate	35
5.1 Driving Error	35
5.2 Combined Error Distribution	42
5.3 Fidelity of Quantum Gate	44
6 Decoupling Protocols	49
6.1 Periodic Driving System	49
6.2 Dynamical Decoupling Sequence	51
6.3 Carr-Purcell Typed Sequences	52
6.4 Long-lived Coherence	54

7 Conclusion	61
7.1 Summary and Discussion	61
7.2 Outlook	62
Bibliography	63
A Monte-Carlo Methods	67
B Supplementary Derivations	69
B.1 Transformation of Joint Rotating Frame	69
B.2 Two-Spin Interaction Hamiltonian in Rotating Frame	70
B.3 Effective Field	72
B.4 Free Induction Decay	72
B.5 Equivalent Noise	74
B.6 Observable on Subspace Eigenstates	74
B.7 Van Vleck Momentum	76
B.8 Driving Hamiltonian in Rotating Frame	77
B.9 Ensemble Averaged FID	77
B.10 Ensemble Average Noise	80
B.11 Rabi Driving with Approximate Noise	80
B.12 Exact solution of Rabi driving	81
B.13 Weak Driving	82
B.14 State Fidelity	83
B.15 Average Gate Fidelity	84
C Supplementary Figures	85
D Supplementary Table	99
E Reproducibility: Data and Code	101

Chapter 1

Introduction

1.1 A Brief History of Quantum Control

Quantum mechanics has the distinguished fame of being the most successful and the most mysterious scientific theory. Since the founding of quantum theory in the 1920s, manipulating quantum systems at molecular and atomic levels has become one of the most exciting dreams of physicists. The earliest attempt to drive a quantum system is realized by Isidor Rabi in 1938[38] when he found nuclear magnetic momentums can be manipulated and measured using pulses of resonant RF or microwave radiation. Rabi was awarded the Nobel Prize in 1944 for this work and his famous discovery is known as Rabi driving today, as one of the most fundamental ideas in quantum science and technology.

It is quite an astonishing fact that many of the basic concepts and tools that are widely used in quantum information processing were already invented in the 1950s. Aside from Rabi driving, the two typical time scales for qubit characterization, relaxation time T_1 and dephasing time T_2 , also originated from energy absorption and free induction decay experiments in NMR, following the discovery of Purcell et al[37][42]. The well-known concept of Bloch sphere was proposed in 1946 by Felix Bloch[7]. The idea of coherent quantum control also emerged during the time, when physicists developed a series of noise mitigation methods to achieve better spectroscopic characterization of molecules. In 1948, Erwin Hahn demonstrated that a simple $\pi/2$ pulse could mitigate the impacts of magnetic field inhomogeneities and refocus the nuclear spin by equivalently reversing its time evolution[18]. The discovery is now known as the Hahn echo. More coherent control sequences, such as Carr-Purcell sequence[11], were later developed to extend the dephasing time of typical NMR systems[42].

The wide application of NMR techniques in quantum information science is not a coincidence. Decades of research in magnetic resonance and spin dynamics provided a sophisticated understanding about how to characterize, control, and manipulate quantum systems. However, no one realized that quantum systems can be used for information processing until 1980s, when Charles Bennett[6], Paul Benioff[5], and Feynman[17] pioneered the thoughts, that information can be stored in the state of a quantum system, and processed by programmable unitary operations constructed from time evolutions of Hamiltonian. The building block of such a quantum system is naturally proposed to be a quantum bit, or qubit, a two-level artificial quantum system mimicking its classical adversary[39]. Due to the equivalence between the qubit and the two-level system from spin magnetization, techniques developed in NMR research can be directly used to drive and control qubits built from various types of physical systems[46], thus emerged the discipline of quantum control.

1.2 Quantum Control for Quantum Information Processing

Back to today, the last decade has witnessed the explosive growth of quantum information science and technology. Coherent control and manipulation of many physical systems have been achieved and utilized to perform information processing, ranging from photons, cold atoms, and trapped ions, to superconducting circuits and electronic spin in solids. Universities, research institutes as well as tech giants, and startup companies supported by venture investors, are all pursuing ambitious new progress in quantum technologies. One of the most famous examples might be the claim of “quantum supremacy” by Google[2]. Other achievements include the distribution of entanglement over remote quantum internet[57][23] and the fast progress and applications of quantum metrology in many fields[12]. Yet, it’s quite hard to turn these pioneering achievements into a practical advantage of quantum technology. The power of quantum hardware is limited due to the noise existing in artificial quantum systems, and the problem of decoherence will become vital as the system size goes larger. In fact, even the most cutting-edge quantum computing platform still can’t beat its classical adversary in any practical task. For other applications like quantum communication and quantum sensing, decoherence and noise also impose severe restrictions in terms of channel fidelity[54], or measurement sensitivity[12].

In a fundamental view, quantum information processing involves dynamical processes of quantum systems, which is inherently non-unitary due to the couplings between the system and its environment. The information stored in qubits will therefore decay over time. To make information processing possible, the coherence time of a quantum system must be extended to a considerable scale, such that a meaningful sequence of quantum operations can be executed before the information is lost.

Realizing that quantum decoherence is inevitable, physicists developed a series of techniques targeting the correction or mitigation of error and noise. One approach is the quantum error correction proposed by Peter Shor in 1995[41][40], following the idea of error correction in classical computer science. Error correction has become an active research field in recent years and it has been experimentally demonstrated in physical systems such as superconducting qubits[35][31]. Yet, building a fault-tolerant quantum computer with error correction code is still quite challenging. First, an error-corrected logical qubit requires multiple noisy physical qubits, depending on different protocols. Then, the fidelity of physical qubits must be higher than a threshold to make error correction possible. It’s estimated that due to these limitations, millions of physical qubits will be needed to perform useful tasks under the current noise level, and the effect of quadratic quantum speedup can’t compensate for the cost[3]. To reduce the cost of error correction, the noise level of physical qubits must be further suppressed.

Therefore, reducing the noise of physical qubits via quantum control techniques would be important to achieve fault-tolerant quantum computers. This approach is also known as quantum noise mitigation. As inspired by the Hahn Echo, precisely manipulating the evolution of qubits with a sequence of control pulses can effectively decouple the qubit from its environment, and thus mitigate the noise and decoherence. These techniques has been widely used in major physical platforms, such as NV-center[51][25][59], neutral atoms array[26], superconducting circuit[10], or ion trap[30], and significantly improved the performance of these systems. However, it’s not clear whether noise mitigation alone will be sufficient to satisfy the hardware requirement of modern quantum technology. More exploration is still needed to characterize the noise in quantum systems and design proper protocols to mitigate them.

1.3 Many-body Noise and Control of Interacting Spins

As one of the most fundamental elements in the quantum world, spins play a major role in various quantum information processing platforms. Spin qubit in silicon quantum dots is regarded as one of the potential approaches to general quantum computing [52][56]. Electronic spins associated with NV-centers in diamond are widely used for nano-scale sensing and imaging[8][44]. Other application based on solid-state spins includes photonic quantum networks[54] and quantum memory[9].

Spin systems are also troubled by noise and decoherence. General sources of noise include magnetic field inhomogeneities and spin-spin interactions such as magnetic dipolar interactions. Mitigating these noises and improving the coherence time of spin qubits will directly benefit all potential applications based on spin systems. Thanks to the research in NMR fields, coherent control techniques have been developed to handle different types of noises. The magnetic field inhomogeneities in NV systems can be effectively mitigated by the CP(Carr-Purcell) like sequences or more advanced XY-8 sequence[25], while magnetic dipolar interactions can be mitigated by WAHUHA(Waugh-Huber-Haeberlen) sequence [53].

Yet, these traditional dynamical decoupling techniques are usually less efficient when disorder and strong spin-spins interactions are present[59], despite their great success in applications to NMR and other weakly coupled spin systems. Besides, the control pulse imperfections, such as the finite duration of pulses and the imperfect shape of pulses, will also deteriorate the performance of the control protocols. Small errors in the control pulses (treated as high order terms in the averaged Hamiltonian theory) may accumulate with time, and lead to unexpected behaviors such as long-lived coherence[20][28]. Furthermore, the dynamics and noise features of low dimensional interacting spin systems (2D, 1D) are not so clear, compared with the well studied 3D case[14].

In brief, precise control of a disordered, strongly interacting spin system remains an open problem. More research and exploration are needed to understand the many-body dynamics and achieve a more sophisticated control. In the view of physics, characterizing the many-body noise can also provide insight into a diverse array of physical phenomena, ranging from Cooper-paired super-fluidity to quantum criticality and many-body localization[15][33][22].

Chapter 2

Spin Qubit in Bath

2.1 Spin as a Qubit

Spin is one of the most fundamental elements of quantum mechanics. We start with the most simple case of spins, spin-1/2. In a background field \vec{B} , its magnetic energy is described by the Hamiltonian

$$\mathcal{H} = -\vec{\mu} \cdot \vec{B} = -\hbar\gamma B_0 I_z. \quad (2.1)$$

The z axis is along the quantizing field, and B_0 is the field strength. γ is the gyromagnetic ratio of the particle, and I_z is the normalized angular momentum operator in the \hat{z} direction. Angular momentum for spin-1/2 are given by Pauli matrices $I_j = \sigma_j/2$, $j = x, y, z$, where

$$\sigma_x \equiv \begin{pmatrix} 0 & 1 \\ 1 & 0 \end{pmatrix}, \quad \sigma_y \equiv \begin{pmatrix} 0 & -i \\ i & 0 \end{pmatrix}, \quad \sigma_z \equiv \begin{pmatrix} 1 & 0 \\ 0 & -1 \end{pmatrix}, \quad (2.2)$$

Spin-1/2 particles naturally satisfy the definition of a qubit, which can be clearly seen in the matrix form,

$$\mathcal{H} = -\hbar\omega_0 I_z = \begin{bmatrix} -\hbar\omega_0/2 & 0 \\ 0 & \hbar\omega_0/2 \end{bmatrix}, \quad (2.3)$$

The Hamiltonian marks a two-level quantum system with energy splitting $\omega_0 = \gamma B_0$, as shown in Fig. 2.1.

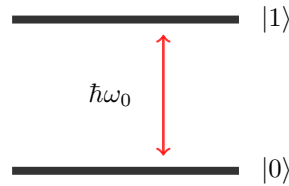


Figure 2.1: Two-level system as a qubit

The states $|0\rangle$ and $|1\rangle$ represent the two energy levels of the system, which are also referred as spin up $|\uparrow\rangle$ and spin down $|\downarrow\rangle$. For single spins, the energy splitting between the two levels, which is just Zeeman splitting, is determined by the Larmor frequency ω_0 .

Any state of such a two-level system can be expressed as

$$|\psi\rangle = e^{i\delta} \left[\cos\left(\frac{\theta}{2}\right) |0\rangle + e^{i\phi} \sin\left(\frac{\theta}{2}\right) |1\rangle \right], \quad (2.4)$$

where θ and ϕ are the two parameters on the sphere, δ is a global phase. It can be visualized with the Bloch sphere, as shown in Fig. 2.2.

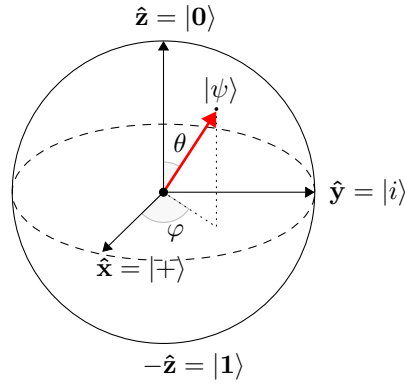


Figure 2.2: Bloch sphere

The vector from the origin to the quantum state marks the direction of its magnetic momentum, as the momentum is characterized by Pauli matrices. Spin-1/2 particles are a natural candidate for qubits. Higher-order spins are not addressed in this thesis since qubit is more relevant in the field of quantum information.

2.2 Cluster of Interacting Spins

Nucleus and electrons are everywhere in nature, and so are spins. Those basic fermion particles are identical and possess odd spin numbers. Electron is spin-1/2 particle, while different species of nuclear spins have different spin quantum numbers, such as 1/2, 3/2, etc. Yet, the abundance of spins in nature is not good news for artificial quantum devices based on spins qubits. An interacting spin cluster can be viewed as a spin qubit in a spin bath, where the impact from the bath on the qubit can be treated as environmental noises. Decoherence and dynamics of the spin qubit can be further studied based on this picture. In order to manipulate spin qubits and protect them from noise and decoherence, the interactions between spins must be taken into consideration. Constructing the basic many-body Hamiltonian for such a spin cluster is the first step to understand the system.

2.2.1 Magnetization

For a cluster of spins in a background quantizing field B_0 , their total Zeeman energy is given by the static Hamiltonian

$$\mathcal{H}_Z = \hbar \sum_i \gamma_i (B_0 + \Delta B_i) S_i^z. \quad (2.5)$$

in which ΔB_i is the inhomogeneity of local magnetic field.

2.2.2 Dipolar Coupling

The most intrinsic interaction between spins is the *magnetic dipole-dipole interaction*, which is also known as dipolar coupling. Consider a cluster of spins, in which two spins are labeled by i and j . The dipolar interaction can be written as a pair-wise summation over all possible (i, j) ,

$$\mathcal{H}_D = \sum_{i < j} \frac{\hbar \gamma_i \gamma_j}{|\vec{r}_{ij}|^3} [3(\vec{I}_i \cdot \vec{n}_{ij})(\vec{I}_j \cdot \vec{n}_{ij}) - \vec{I}_i \cdot \vec{I}_j]$$

μ_0 is the magnetic permeability of free space, and γ_i is the gyromagnetic ratio of i -th spin. \vec{n}_{ij} is the normalized vector between the location of spin i and the location of spin j . \vec{I}_i is a vector of all Pauli matrices of the spin $\vec{I}_i = (I_i^x, I_i^y, I_i^z)$.

The dipolar coupling originated from the electromagnetic force and is thus a long-range interaction. It exists between both electron spins and nuclei spins.

2.2.3 Qubit in a Spin Bath

Given the Hamiltonian of a single spin and the spin interactions, we can model the spin qubit in an interacting spin bath, as shown in Fig. 2.3. The cluster contains two parts, the central spin qubit, and the environmental spins as a noisy bath. Interactions between the bath spins and the central spin qubit will lead to decoherence of the qubit.

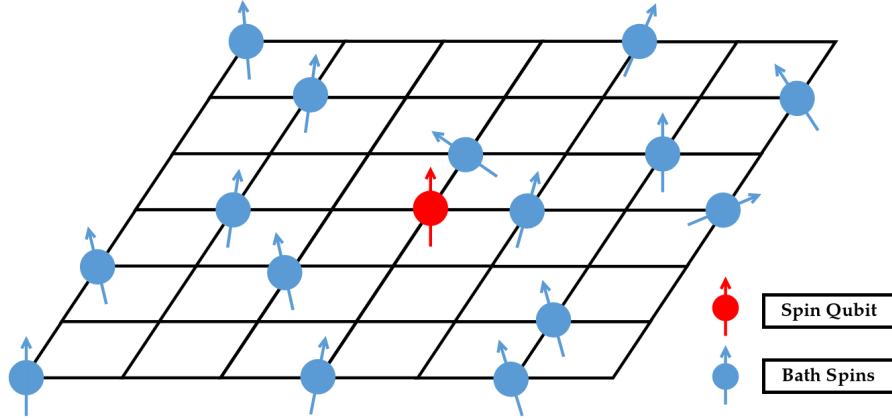


Figure 2.3: A solid spin qubit in a bath of interacting spins

For nitrogen-vacancy centers in diamonds, dipolar interaction between the spin qubit and nuclear spins (^{13}C), and paramagnetic impurities (N) in its environment is a major source of the noise. NV-associated electronic spin will inevitably interact with these spins in the environment and thus suffer from decoherence[32][21]. Due to the low density of bath spins, the average distance between two bath spins is much larger than the lattice constant. Thus the long-range dipolar coupling will be dominant, while scalar couplings and hyperfine couplings can be safely ignored.

Situations are more complicated for spin qubits in semiconductor quantum dots. Dipolar coupling between the electron spin in dots and bath spins, such as ^{71}Ga and ^{75}As in GaAs quantum dot[24], is still an important source of decoherence, but other types of noise such as hyperfine coupling between the nuclei and electron spins or charge noise originated from the Coulomb interaction will also affect the performance of the qubit[36].

Among all the spin interactions given above, dipolar interactions between spins is the most general one. A model of interacting spins cluster based on dipolar couplings will be useful to study various topics in spin dynamics and quantum information processing, the Hamiltonian of which can be given as

$$\mathcal{H}_{sys} = \mathcal{H}_Z + \mathcal{H}_D = \hbar \sum_i \gamma_i (B_0 + \Delta B_i) S_i^z + \sum_{i < j} \frac{\hbar^2 \mu_0 \gamma_i \gamma_j}{4\pi |\vec{r}_{ij}|^3} [3(\vec{S}_i \cdot \vec{n}_{ij})(\vec{S}_j \cdot \vec{n}_{ij}) - \vec{S}_i \cdot \vec{S}_j]. \quad (2.6)$$

The interaction is written in SI unit thus there is a prefactor of $\mu_0/4\pi$. We use a dimensionless spin operator S , thus an extra \hbar is appended. This norm will follow in the coming chapters.

We will focus on the many-body Hamiltonian given in Eqn. 2.6 and explore the coherent control of such a system. Sophisticated interactions of electron spins will not be covered in this thesis.

2.3 Hamiltonian in the Rotating Frame

As a basic discovery in magnetic resonance, spins precess around the z axis in a quantizing field[42]. In a many-spin system, the precessions, considering the inhomogeneity as well, can be fully eliminated by using a joint rotating frame of all spins.

2.3.1 Rotating Frame Transformation

A transformation to the joint rotating frame of multiple spins is

$$|\psi\rangle \rightarrow \prod_j e^{-it\tilde{\omega}_j S_j^z} |\psi\rangle_R \quad (2.7)$$

in which $\tilde{\omega}_j$ is the angular velocity for each spin. Substitute the transformation into the Schrodinger equation will give the Hamiltonian in the rotating frame, as shown in the appendix B.1

$$\mathcal{H}^{\text{rot}} = V^\dagger \mathcal{H}^{\text{lab}} V - \hbar \sum_j \tilde{\omega}_j S_j^z, \quad V = e^{-it \sum_j \tilde{\omega}_j S_j^z}. \quad (2.8)$$

The product $\prod_j e^{-it\tilde{\omega}_j S_j^z}$ can be contracted to a exponential summation since S_j^z is commutative with each other.

Apply the transformation to the system Hamiltonian given by Eqn. 2.6,

$$\mathcal{H}^{\text{rot}} = V^\dagger \mathcal{H}_Z^{\text{lab}} V + V^\dagger \mathcal{H}_D^{\text{lab}} V - \hbar \sum_j \tilde{\omega}_j S_j^z. \quad (2.9)$$

2.3.2 Secular/Non-Secular Hamiltonian

For the dipolar coupling, most terms are oscillating after the rotating frame transformation, as $S_i^+ S_j^- e^{i(\tilde{\omega}_i - \tilde{\omega}_j)t}$, while others, such as $S_i^z S_j^z$ are not. Those terms which are oscillating at the Larmor frequencies of spins, can not be observed with a low-frequency measurement since their time integral during the measuring period goes to zero[42]. These oscillating terms are called non-secular terms, and those non-oscillating terms are called secular. Here we need to decide which terms are secular that should be preserved and which terms are non-secular and thus should be dropped.

It can be shown that all the other terms in $(\vec{S}_i \cdot \vec{n}_{ij})(\vec{S}_j \cdot \vec{n}_{ij})$ are oscillating with Larmor frequencies, with proof given in the appendix B.1. Here all the crossing terms are non-secular that should be dropped, while further discussions are needed for flip-flop terms $n_x^2 S_i^x S_j^x + n_y^2 S_i^y S_j^y$.

Like Spins

We start from the case of like spins, which means the two spins have quite similar Larmor frequencies. In this case, the difference between Larmor frequencies can be ignored compared with the dipolar interaction strength $|\omega_i - \omega_j| \ll D_{ij}$. This condition can be extended to multiple spins, $|\omega_i - \omega_j| \ll \sqrt{\sum_{ij} D_{ij}^2}$ for any pair of spins in a spin cluster. An ideal example of this situation is a cluster of homonuclear spins in a uniform global magnetic field, where all spins have the same Larmor frequency given by the quantizing field $\omega_i = \omega_j = \omega_0$.

The Hamiltonian of likes spins in the rotating frame is given by

$$\mathcal{H}^{\text{rot}} = \mathcal{H}_Z^{\text{rot}} + V^\dagger \mathcal{H}_{D,ij} V = \sum_{i < j} \frac{\hbar^2 \mu_0 \gamma_i \gamma_j}{4\pi} \frac{3n_z^2 - 1}{2|\vec{r}_{ij}|^3} (3S_i^z S_j^z - \vec{S}_i \cdot \vec{S}_j) \quad (2.10)$$

in which the constant coefficients are dropped and we used that $n_x^2 + n_y^2 + n_z^2 = 1$. Write elementary vector in spherical coordinate, $(n_x, n_y, n_z) = (\sin \theta \cos \phi, \sin \theta \sin \phi, \cos \theta)$, then you can get the formula of dipolar coupling strength

$$D_{ij,\text{like}} = \frac{\hbar \mu_0 \gamma_i \gamma_j}{4\pi} \frac{3 \cos^2 \theta_{ij} - 1}{2|\vec{r}_{ij}|^3}. \quad (2.11)$$

Unlike Spins

If the difference between Larmor frequencies of spins is much larger than the dipolar coupling strength, $|\omega_i - \omega_j| \gg D_{ij}$, then the two spins are called unlike spins. This is a typical case when a strong inhomogeneity of magnetic field is present in the system. Therefore the oscillating terms related with $e^{-it(\omega_i - \omega_j)}$ are non-secular. In this case, all the flip-flop terms are dropped and only Ising zz terms are preserved.

$$\mathcal{H}^{\text{rot}} = \mathcal{H}_Z^{\text{rot}} + V^\dagger \mathcal{H}_{D,ij} V = \sum_{i < j} \frac{\hbar^2 \mu_0 \gamma_i \gamma_j}{4\pi} \frac{3n_z^2 - 1}{|\vec{r}_{ij}|^3} S_i^z S_j^z \quad (2.12)$$

with a coupling strength

$$D_{ij,\text{unlike}} = \frac{\hbar \mu_0 \gamma_i \gamma_j}{4\pi} \frac{3 \cos^2 \theta_{ij} - 1}{|\vec{r}_{ij}|^3} \quad (2.13)$$

The approximation of unlike spins is more useful in practical quantum devices. For an example, the Larmor frequency of ^{13}C at $B_0 = 7.04 \text{ T}$ is 75.47 MHz . While in a diamond lattice the unit cell length is approximately $a = 3.56 \text{ \AA}$. The dipolar coupling strength between two neighboring ^{13}C spins is then $(\mu_0 \gamma^2 \hbar) / (4\pi a^3) \approx 13.45 \text{ Hz}$. The noise linewidth of multiple interacting spins is given by $b = \sqrt{\sum_j D_j^2}$. Taking this into consideration, the effective magnitude of dipolar coupling is still much smaller than the Larmor frequency even at a lower magnetic field.

Summary

Define the dipolar coupling strength of like spins $D_{ij,\text{like}}$ as a new D_{ij} , then $D_{ij,\text{unlike}} = 2D_{ij}$. We can rewrite the Hamiltonians given in Eqn. 2.12 as

$$\mathcal{H}_{\text{like}} = \sum_{i < j} \hbar D_{ij} (3S_i^z S_j^z - \vec{S}_i \cdot \vec{S}_j), \quad \mathcal{H}_{\text{unlike}} = \sum_{i < j} 2\hbar D_{ij} S_i^z S_j^z.$$

In practice, the approximation of unlike spins is a better description of the experimental system due to strong local field inhomogeneity.

2.4 Thermalized Spin Bath

In the picture of a spin qubit and a noisy bath, we must first know the basic properties of the bath before analyzing the dephasing of the qubit. First, we assume that the qubit is surrounded by a bath at a constant temperature, such that the system can be described by a canonical ensemble[42]. Then we assume that the spin bath is large enough and fully thermalized such that the bath should stay at its equilibrium state.

In a canonical ensemble, the equilibrium distribution of possible energy eigenstates obeys the Boltzmann statistics

$$P(|p\rangle) = \frac{1}{Z} \exp\left(-\frac{E_p}{k_B T}\right), \quad E_p = \langle p | \mathcal{H} | p \rangle, \quad Z = \sum_p \exp\left(-\frac{E_p}{k_B T}\right). \quad (2.14)$$

in which T is the temperature of the spin bath, Z is the canonical partition function given by The energy eigenstate $|p\rangle$ is defined by the configurations of spins, which takes a form $|\uparrow\uparrow\downarrow\uparrow\dots\rangle$. Due to the orthogonality of eigenstates, non-diagonal terms will be zero, $\langle i|\mathcal{H}|j\rangle = 0$, $i \neq j$. Thus the equilibrium density matrix of the bath is given by

$$\rho_B = \frac{1}{Z} \sum_p \exp\left(-\frac{E_p}{k_B T}\right) |p\rangle\langle p|. \quad (2.15)$$

in which N is the volume of all possible states. The expectation of any observable in such a quantum system is given by

$$\langle \hat{A} \rangle = \sum_{i=1}^N p_i \hat{A}_i = \frac{1}{N} \sum_{i=1}^N \langle i|\rho_B \hat{A}|i\rangle, \quad (2.16)$$

which i labels an eigen states $|i\rangle$ and $A_i = \langle i|\hat{A}|i\rangle$, $N = 2^n$ is the total number of the possible states. This formulation enables a Monte-Carlo based numerical simulation of the quantum dynamics, which will be introduced in later chapter of the thesis.

In reality, the energy scale of E_p is mainly characterized by the Zeeman energy of bath spins. $E_p = \langle p|\mathcal{H}|p\rangle \simeq \hbar \gamma_n B_0 \langle p|\sum_j S_j^z|p\rangle$, in which γ_n is the gyromagnetic ratio of bath spins and B_0 is the strength of quantizing field. For example, we can choose γ_n as the gyromagnetic ratio of ^{15}N , and $B_0 = 1 \text{ T}$, then $|\hbar \gamma_n B_0| \approx 4.2 \cdot 10^{-9} \text{ eV}$.

Since $k_B T \approx 8.6 \times 10^{-5} \text{ eV}$ at $T = 1 \text{ K}$, we can always assume that $|\hbar \gamma_n B_0|/k_B T \approx 4 \times 10^{-5}$. Assuming the bath is dilute, then we can consider only a limited amount of spins $n < 1000$ in the bath that are close to the qubit as the dipolar couplings decay with $|r|^{-3}$. In this condition, we can say that $\epsilon \ll 0$ in general. Therefore,

$$P(|p\rangle) \leq \exp(-n|\hbar \gamma_n B_0|/k_B T) = \lim_{\epsilon \rightarrow 0} e^{-\epsilon} \approx 1 - \epsilon, \quad (2.17)$$

in which n is the total number of spins, and $\epsilon = n|\hbar \gamma_n B_0|/k_B T$. The density matrix can be given as

$$\rho = \frac{1}{\sum_p (1 - \epsilon_p)} \begin{pmatrix} 1 - \epsilon_1 & & \\ & \ddots & \\ & & 1 - \epsilon_N \end{pmatrix} \approx \frac{1}{N} \mathbb{1}, \quad (2.18)$$

in which $\mathbb{1}$ is an identity matrix of $N \times N$ dimension. This case usually appears at a high temperature, where $k_B T \gg E_p$. It's a quite interesting fact that 1 Kelvin is already quite "hot" for nuclear spins.

2.5 Decoherence

Quantum decoherence indicates a dynamical quantum process where phase information of a system is gradually lost due to its coupling to the environment. While noisy qubits can be treated as an open system with a master equation governing its dynamics, a more intuitive approach to understand the decoherence is to model the noisy qubits as a closed system with both qubits and noisy bath. Knowing the interacting Hamiltonian of cluster spins, we can build the model of a central spin qubit interacting with a noisy spin bath. The noise spectrum and quantum decoherence process can then be derived from the system dynamics.

2.5.1 Free Induction Decay

Long before the concept of decoherence was introduced into physics in 1970[58], physicists in NMR fields already found that the signal generated from transverse nuclear polarization

will decay over time, known as the *free induction decay* (FID)[19]. This experiment is one of the earliest demonstrations of T_2 relaxation, which shows a quite intuitive picture of quantum decoherence.

The experiment initializes a spin at transverse axis $|+\rangle$ and then observes the spontaneous decay of the polarization. Consider a spin cluster of $n + 1$ unlike spins, in which the central spin qubit is labeled by '0', and the spin bath labeled 'b'. The Hamiltonian of the system is then given by Ising-type interactions that can be exactly solved.

$$\mathcal{H} = \sum_{j=1}^n 2\hbar D_j S_j^z S_0^z \quad (2.19)$$

The transverse polarization $f(t) \propto \langle S_0^x(t) \rangle$ will decay with time, which can be solved using Eqn. 2.16.

$$\langle S_0^x(t) \rangle = \frac{1}{N} \sum_{p=1}^N \langle p | S_0^x(t) | p \rangle = \frac{1}{N} \sum_{p=1}^N \langle p | U S_0^x U^\dagger S_0^x | p \rangle. \quad (2.20)$$

In the above expression, $|p\rangle$ is one eigenstate of the bath spins, and the total number of bath eigenstates is $N = 2^n$. An effective magnetic field operator can be defined as

$$\hat{B} = \sum_j 2D_j S_j^z = \mathbb{1} \otimes \hat{B}_b. \quad (2.21)$$

\hat{B}_b is an effective operator on the bath subspace. Its eigenvalue can be easily found as

$$\beta_p = \langle p | B_b | p \rangle = \sum_j p_j D_j = \vec{P}_p \cdot \vec{D} \quad (2.22)$$

with $\vec{P}_p = (p_1, p_2, \dots, p_n)$, $p_j = \pm 1$; $j = 1, 2, 3 \dots$ is a state of spin configurations, and $\vec{D} = (D_1, D_2, \dots, D_n)$ is the set of dipolar coupling strengths.

It can be shown that the FID curve is given by,

$$\langle S_x(t) \rangle = \frac{1}{2} \frac{1}{N} \sum_{p=1}^N \cos(\beta_p t) = \frac{1}{2} \prod_j \cos(D_j t). \quad (2.23)$$

with detailed derivation given in Appendix. B.3, B.4. The formula contains a set of cosine Fourier components, in which the effective frequencies of each component is given by β_p . Here we should notice that the β_p is not in the dimension of field strength, but in the dimension of frequency, just like $\{D_j\}$. β_p/γ is in the actual effective field.

2.6 Equivalent Noise

The dephasing process can also be characterized as relaxation with noise, from an equivalent fluctuation of the background field. This equivalence between noise and decoherence is a key insight that enables the modeling of decoherence from a statistical approach.

2.6.1 Continuous Spectrum Approximation

We start from the basic formula for free induction decay and prove that it equals an Gaussian type fluctuation of the background field. In the microcanonical ensemble, any observable is given by the unweighted average, as given by Eqn. 2.16. This is also true for the FID observable given in Eqn. B.22. **If we look at the formulas more carefully, we will realize that the discrete expectation, which is a summation labeled by p , can be well approximated by an**

integral over a continous probability distribution. Rewrite the expectation of observable, it can be transformed into

$$\begin{aligned}\langle S_0^x(t) \rangle &= \frac{1}{N} \sum_{p=1}^N \text{Tr} \left[S_x U(\beta_p; t) S_x U(\beta_p; t)^\dagger \right] \\ &= \int_{-\infty}^{\infty} \langle S_x(t; \beta) \rangle P(\beta) d\beta,\end{aligned}\quad (2.24)$$

in which the discrete expectation is transformed into an continuous one, as shown in B.5. The derivations above demonstrates the equivalence between the dephasing and effective fluctuation of field, subject to a static noise distribution $P(\beta)$. The effective unitary is given by $U(\beta; t) = \cos(\beta t/2) - i \sin(\beta t/2) \sigma_z = e^{-i \mathcal{H}_\beta t/\hbar}$, from which we can get the effect Hamiltonian

$$\mathcal{H}_\beta = \hbar \beta S_z = \hbar \gamma \delta B S_z. \quad (2.25)$$

Now the physical meaning of β is clear, it equals a fluctuation of the local field with a constant prefactor $\delta B = \beta/\gamma$.

2.6.2 Distribution of Noise

The statistical properties of the distribution can be obtained from the Van Vleck method[45], by analyzing the momentum of its characteristic function (Fourier transform).

$$f(t) = \int_{-\infty}^{\infty} P(\omega) e^{-i\omega t} d\omega \quad (2.26)$$

And the k-th order momentum is given by

$$M_k = \left(\frac{d^k f(t)}{dt^k} \right) = (-i)^k \int_{-\infty}^{\infty} \beta^k P(\beta) e^{-i\beta t} d\beta \quad (2.27)$$

Substitute in Eqn. 2.22, $\beta = \sum_{j=1}^n p_j D_j$, then we can get the second order momentum and fourth order momentum

$$M_2 = \sum_i D_i^2, \quad M_4 = 3 \left(\sum_i D_i^2 \right)^2 - 2 \sum_j D_j^4. \quad (2.28)$$

A detailed derivation is given in B.7 The fact $M_4 < 3M_2^2$ indicates that $P(\beta)$ is similar to Gaussian distribution. This can be seen by deriving the Van Vleck momentum of Gaussian distribution,

$$\mathcal{N}(0, b) = \frac{1}{\sqrt{2\pi b}} e^{-\frac{x^2}{2b^2}}. \quad (2.29)$$

At $t = 0$, the second and forth order momentum are $M_2|_{t=0} = -b^2$, $M_4|_{t=0} = 3b^4$. Thus the forth order momentum of the Gaussian distribution is three times to the second order momentum, $M_4 = 3M_2^2$, at $t = 0$. Compare it with the result we get from the spin noise, we can get the standard deviation, or linewidth b , of the Gaussian distribution

$$b = \sqrt{\sum_i D_i^2} \quad (2.30)$$

If we assume the noise distribution is precisely a Gaussian noise, then we can get the free induction decay curve from its Frouier transform.

$$\langle S_x(t) \rangle = \int_{-\infty}^{\infty} \langle S_x(\beta, t) \rangle P(\beta) d\beta = \frac{1}{2} \text{Re} \int_{-\infty}^{\infty} e^{-i\beta t} P(\beta) d\beta = \frac{1}{2} e^{-\frac{1}{2} b^2 t^2} \quad (2.31)$$

The integral part is exactly the characteristic function of the noise spectrum $P(\beta)$. The coherence time is given by $T_2 = b^{-1}$.

Chapter 3

Ensemble of Spins

3.1 Ensemble of Disorder Realizations

The model of a cluster of interacting spins has been discussed in the previous chapter. Yet, there is still one question to answer – how could we choose a specific cluster of spins? A spins cluster is defined by a variety of global parameters such as the species of spins, the natural abundance of these spin-possessing isotopes, the crystal structure in which they are placed, or the chemical bonds in a molecule if we are looking into an NMR system. These parameters can be specified by a given experimental setup. However, there always exist local variables that can't be controlled experimentally. In the context of a spin qubit in a noisy bath, the properties of the bath are one problem that can't be addressed by engineering efforts. The noise spectrum produced by the bath spins can vary significantly even in the same calibrated system. Advanced nano-fabrication skills may reduce flaws and noise in a quantum device, but full elimination of environmental couplings is almost impossible.

As a result, randomness is inevitably introduced into the system. This kind of randomness, or *disorder* as known by condensed-matter physicists, is an intrinsic property of nature.

In our simplified model, a cluster of interacting spins is characterized by a set of coupling strengths $\{D_j\}$ of the magnetic dipolar interactions. The distribution of $\{D_j\}$ depends on the positions as well as the species of spins. We can write it in a concise form

$$\vec{D}_\xi = \vec{D}(\{\vec{r}_j^{(\xi)}\}, \{\gamma_j^{(\xi)}\}) \quad (3.1)$$

in which $\{\vec{r}_j^{(\xi)}\}$ is a set of positions for the spin cluster, and $\{\gamma_j^{(\xi)}\}$ is their gyromagnetic ratios. A **disorder realization** (DR) of our spin cluster is uniquely specified by the two set of parameters, which is labeled by ξ .

The positions of spins $\{\vec{r}_j^{(\xi)}\}$ is a key issue to be addressed. In solids, spins are associated with nuclei placed on a crystal lattice. A simple case is that the lattice is fully occupied by spins, then $\{\vec{r}_j^{(\xi)}\}$ is just a set of fixed positions of lattice sites with geometrical symmetry. If the natural abundance of the spins-possessing atoms is smaller than 1, then a random subset of sites must be chosen to place spins. In this case, the symmetry of the crystal lattice is no longer present, as shown in Fig. 3.1. Such an absence of symmetry, or disorder, is a key feature to be considered in our system. The dynamics of the system may change drastically due to the significant statistical fluctuation of random spin distribution.

Since the local magnetization of a spin is affected by its surrounding spin-bath, the disorder of spin positions will lead to a fluctuation in local field strength. Thus if an external transverse magnetic field is applied to drive a spin cluster, the Rabi frequency will be different for each spin. Some spins with a very large local magnetization can't be effectively driven by external fields. In this way, disorder brings extra complexity to the system and makes the precise control of a quantum system more challenging.

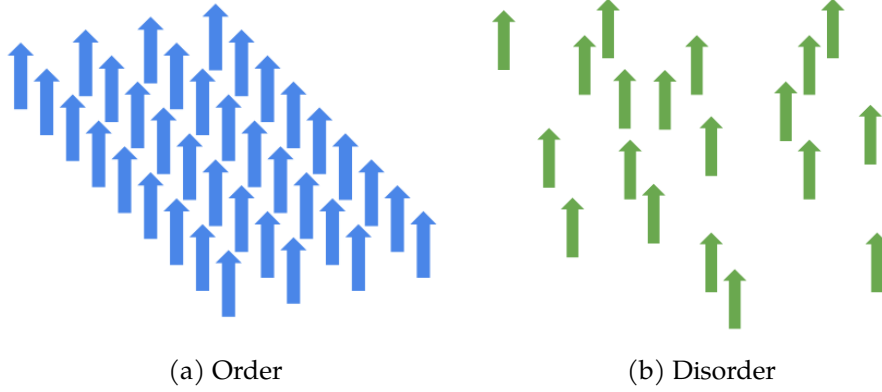


Figure 3.1: Comparison between ordered and disordered spin clusters

In principle, there are infinitely many possible realizations of a spin cluster, given that the bath spins can be randomly distributed. Thus it doesn't make much sense if we only study one specific cluster. Statistical approaches will be necessary to provide more insights into the system. We define a spin ensemble as a collection of all the possible realizations of a spin cluster, $\Omega(\xi) = \{\vec{D}_\xi\}$, where ξ labels a realization of spin cluster. Since there is no difference between one disorder realization and another. The probability of reaching each realization will be equal,

$$P(\xi) = \frac{1}{|\Omega(\xi)|}. \quad (3.2)$$

The properties of such an ensemble are defined by various parameters.

Spin Species

The configuration of gyromagnetic ratios $\{\gamma_j\}$ is decided by the species of spins. For homonuclear spins, γ is just a fixed parameter. Assume that we have k different types in n spins, the number of which is n_k respectively, then the configuration can be represented by a integer string $\{\theta_i\}$, $\theta_i = 1, 2, \dots, k$. The total number of combinations is given by

$$N_\theta = \binom{n}{n_1} \binom{n-n_1}{n_2} \dots \binom{n-\sum_{i=1}^{k-1} n_i}{n_k} = \binom{n}{n_1, n_2, \dots, n_k} = \binom{n+k-1}{k-1} \quad (3.3)$$

There is only one species of spins, then positional disorder will be the only parameter as shown in Eqn. 3.1 and $N_\theta = 1$.

Crystal Lattice

If spins are placed on a crystal lattice, then their positional disorder can be characterized by a bitstring $\{\phi_i\}$, where $\phi_i = 0/1$ indicates whether a lattice site i is filled. Thus filling fraction is therefore given by

$$f = \frac{\sum_i \phi_i}{|\{\phi_i\}|} = \frac{n}{m} \quad (3.4)$$

in which m is the total number of sites on lattice, and n is the number of spins. The crystal lattice can be treated as a mapping from the bitstring $\{\phi_i\}$ to a set of spin positions $\{\vec{r}_j\}$.

$$L : \{\phi_i\} \mapsto \{\vec{r}_j\} \quad (3.5)$$

Then the size of a homonuclear ensemble is given by the combination $N_\phi = \binom{m}{n}$. If we consider the configuration of spin species, then the total number of possible disorder realization

(DR) is

$$M = |\Omega(\xi)| = \binom{m}{n} \binom{n+k-1}{k-1} = N_\phi \cdot N_\theta \quad (3.6)$$

Dimension

Dimensionality plays an important role in the world of condensed-matter physics, governing many interesting phenomena like phase transition and localization. For example, the Ising model, as a close variant of our system, demonstrates phase transition in two dimensions but is trivial in one dimension.

In our system, dimension is another intrinsic parameter. This can be shown by a simple calculation. Consider a d dimensional cubic lattice with cell constant a . If the filling fraction is f , then the density of spins will be $\rho = f/a^d$, the average distance between two spins is

$$\bar{r} = \sqrt[d]{\bar{V}} = \frac{a}{f^{1/d}} \quad (3.7)$$

For a fixed filling fraction f , the average distance between spins is completely different. As a result, the statistical distribution of coupling strengths $\{D_j\}$ varies significantly with dimensions, leading to completely different effective noises and relaxation curves for different dimensions[16].

Dimension can be regarded as a meta-parameter of the crystal lattice, since lattice has different symmetries in different dimensions.

$$L^{(d)} : \{\phi_i\} \mapsto \{\vec{r}_j\}$$

Abundance

Here, the spin abundance, or the filling fraction f , which is the average spin per lattice site, plays an important role since it directly decides how much randomness will be here in the system. When filling fraction is approximately $f \approx 0$, the average distance between each pair of spins will be very large such that $\bar{r} \gg a$. Then the lattice structure can be ignored and positions of spins can be treated as quasi-continuous. In this situation, the number of total lattice sites is also much more larger than the filling sites, $m \gg n$, so the combinational number will go to infinity as f approaching zero,

$$\lim_{f \rightarrow 0} |\Omega(\xi)| = \lim_{m \rightarrow \infty} \binom{m}{n} = \infty. \quad (3.8)$$

As shown in Eqn. 3.7, the filling fraction for a dilute ensemble, $\bar{r} \gg a$ vary with the dimension of the system. For example if we want $\bar{r}/a = 10$ then the filling fraction would be $f = 0.1$ for a one dimensional spin chain, but $f = 0.001$ for a 3D spin cluster.

On the opposite, if the filling fraction is higher, the lattice structure can no longer be ignored when considering the spin positions. A particularly interacting situation is when the lattice is fully occupied by spins $f \approx 1$. In this case, the system Hamiltonian will degenerate to an Ising model, which exhibits many fascinating phenomena such as ferromagnetism and phase transition.

In this thesis, we only focus on *dilute spin system* where the filling fraction is quite small $f \ll 1$. A dilute ensemble is a reasonable approximation to practical experimental systems since purified spin-free isotopes are used in the fabrication process to reduce the environmental coupling[47][4]. Thus the abundance of nuclear spins in solids can be reduced to a very low level. When multiple types of spins exist in the system, providing all of them are sufficiently dilute, the system can be regarded as a simple superposition of many randomly

distributed spin clusters. Therefore, the combinations of different types of spins are not a concern to our system. Positions of spins will be the only parameter of coupling strengths.

$$\vec{D}_\xi = \vec{D}(\{\vec{r}_j^{(\xi)}\})$$

3.2 Averaged Dephasing in Dilute Ensemble

The formula of free induction decay (FID) of a central spin is given in Section. 2.5.1. From this formula we can derive the the cluster average FID on a specific spin cluster is given by

$$\langle G(t) \rangle_c = \frac{1}{n} \sum_{k=1}^n \prod_{j \neq k} \cos(D_{jk}t) \quad (3.9)$$

following the formalism in previous section, in which n is the number of spins, D_{jk} is the coupling strength. We dropped the prefactor $\frac{1}{2}$, which is from the spin $1/2$.

Define the ensemble average of an observable G , following the same formalism,

$$\langle G \rangle_\xi = \frac{1}{M} \sum_{\{\phi_i\}} G(\{\phi_i\}) \quad (3.10)$$

in which M is the number of possible disorder realization $|\{\phi_i\}|$.

According to statistical physics, if the spin ensemble is large enough (macroscopic), then the macro properties of the system should converge to their statistical expectations, $\lim_{n \rightarrow \infty} |\langle G \rangle_c - G(\{\phi_i\})| = 0$, providing that filling fraction f is fixed. Here n is the number of particles(spins) in the system. That means the observable from any two disorder realization $\{\phi_i\}_A$ and $\{\phi_i\}_B$ would be the same when n or equivalently M is large enough and statistical fluctuation of spin configuration is eliminated. This property is called **self-averaging**. Therefore, the observable from a very large spin cluster is equivalent to the ensemble average over disorder realizations at the macroscopic limit.

Using the self-averaging theorem we can find that the cluster average equals the ensemble average when the cluster size n is very large.

$$\lim_{n \rightarrow \infty} \langle G \rangle_c = G(\{\phi_i\}) = \frac{1}{M} \sum_{\{\phi_i\}} G(\{\phi_i\}) \quad (3.11)$$

As shown in the last section, we can assume the spins are distributed in a continuum space and drop the lattice structure providing the spin ensemble is dilute ($f \ll 1$). At the dilute limit, the species of spins are also irrelevant, and thus degenerate to a constant γ . Replace the discrete spin configurations $\{\phi_i\}$ with a a set continuous positions $\{\vec{r}_j\}$, where \vec{r}_j denotes the location of j -th particle. The ensemble average of FID can be rewritten as

$$\langle G(t) \rangle_c = \int \dots \int \frac{d^D r_1}{V} \frac{d^D r_2}{V} \dots \frac{d^D r_{N-1}}{V} G(t; \{\vec{r}_j\}) \quad (3.12)$$

Substitute in the Eqn. 3.9 and we get

$$\begin{aligned} \langle G(t) \rangle_c &= \frac{1}{N} \sum_k \int \dots \int \frac{d^D r_1}{V} \frac{d^D r_2}{V} \dots \frac{d^D r_{N-1}}{V} \prod_{j \neq k} \cos(D_{jk}t) \\ &= \frac{1}{N} \sum_k \int \frac{\cos(D_{1k}t)}{V} d^D r_1 \int \frac{\cos(D_{2k}t)}{V} d^D r_2 \dots \int \frac{\cos(D_{jk}t)}{V} d^D r_j \end{aligned} \quad (3.13)$$

The series of integrals is the average over the locations of $N - 1$ spins, labeled by j , around a central spin k . Then the label k is averaged.

In a macroscopic ensemble, the spins are indistinguishable from each other. Thus we can swap the indices of any two spins and $\langle G(t) \rangle_c$ should remain the same. The symmetry implies quantities labeled by an index j should be statistically equivalent,

$$\int \frac{\cos(D_{ik}t)}{V} d^D r_i = \int \frac{\cos(D_{jk}t)}{V} d^D r_j$$

With this approximation, the Eqn. 3.13 can be further simplified

$$\begin{aligned} \langle G(t) \rangle_c &= \frac{1}{N} \sum_k \left[\frac{1}{V} \int \cos(D_{jk}t) d^D r_j \right]^{N-1} \\ &\approx \frac{1}{N} \sum_k \left[1 - \frac{1}{V} \int (1 - \cos[D_{jk}t]) d^D r_j \right]^{N-1} \\ &\approx \frac{1}{N} \sum_k \exp \left\{ -\frac{N}{V} \int [1 - \cos(D_{jk}t)] d^D r_j \right\} \end{aligned}$$

in which we used the formula in last step.

$$\lim_{n \rightarrow \infty} \left(1 + \frac{a}{n}\right)^n = \lim_{n \rightarrow \infty} \exp \left[n \ln \left(1 + \frac{a}{n}\right) \right] = e^a$$

We can invoke the indices symmetry again to drop the average over k

$$\langle G(t) \rangle_c = \exp \left\{ -\frac{N}{V} \int [1 - \cos(D_{jk}t)] d^D r_j \right\} \quad (3.14)$$

The physical picture of the above formula is quite similar to mean-field theory (MFT), where the FID of a central spin k is affected by the mean-field average of all bath spins labeled by j . It should be noticed that Eqn. 3.14 only works for macroscopic, ($N \rightarrow \infty$) dilute ($f \ll 1$) spin ensemble.

In the following derivations, the dimension is labeled by D to distinguish from the derivative symbol d , the particle number is labeled by N instead of n . Substitute D_{ij} into the Eqn. 3.14 and assume that the average position of central spin k is zero, then

$$\langle G(t) \rangle_c = \exp \left\{ -\frac{N}{V} \int \left[1 - \cos \left(\frac{1 - 3 \cos^2(\theta)}{2r^3} \mu_0 \gamma^2 \hbar t \right) \right] r^{D-1} dr dA \right\} \quad (3.15)$$

in which we used that $d^D \vec{r} = dv = r^{D-1} dr dA$ and dA is the area element in $D-1$ dimension.

Evaluate Eqn. 3.15 will give the ensemble-averaged FID curves in different dimensions. The detailed derivation is shown in the Appendix. B.9.

1D

The ensemble averaged FID curve in 1D is given by,

$$\langle G(t) \rangle_c = \exp \left\{ \frac{\sqrt{3}\rho}{3} \Gamma \left(-\frac{1}{3} \right) \left| \frac{1 - 3 \cos^2(\theta)}{2} \mu_0 \gamma^2 \hbar t \right|^{1/3} \right\} \quad (3.16)$$

in which θ is the angle between the 1D spin chain and the external field. $\rho = N/V$ is the density of the spin cluster.

2D

The ensemble averaged FID cruve in 2D is given by,

$$\langle G(t) \rangle_c = \exp \left\{ -\frac{\rho}{3} \left(\frac{\mu_0 \gamma^2 \hbar t}{2} \right)^{2/3} \Phi(\theta) S_2 \right\}. \quad (3.17)$$

in which $\Phi(\theta)$ is an integral about θ , given by

$$\Phi(\theta) = \int_0^{2\pi} |1 - 3 \cos^2(\theta) \cos^2(\varphi)|^{2/3} d\varphi. \quad (3.18)$$

Here θ is the angle between the external field and the 2D plane. $\theta = 0$ when the external field is parallel to the plane. $\theta = \pi/2$ when the external field is perpendicular to the plane. For these two case we get $\Phi(0) \approx 6.01$ and $\Phi(\pi/2) = 2\pi$

When $\theta = \pi/2$, we get

$$\langle G(t) \rangle_c = \exp \left\{ \frac{\pi \rho}{3} \Gamma \left(-\frac{2}{3} \right) \left(\frac{\mu_0 \gamma^2 \hbar t}{2} \right)^{2/3} \right\} \quad (3.19)$$

3D

The ensemble averaged FID cruve in 2D is given by,

$$\langle G(t) \rangle_c = \exp \left\{ -\frac{1}{6} \rho \pi^2 \mu_0 \gamma^2 \hbar t \cdot \frac{8}{3\sqrt{3}} \right\}. \quad (3.20)$$

The formula is not related to the direction of the external field since 3D space is isotropic so the z-axis can always be chosen along the external quantizing field. The derivation for the ensemble-averaged FID curve in arbitrary D dimension is put in Appendix. ??.

General D dimensional situations

The general expression for D dimensional FID is given by Eqn. 3.15,

$$\langle G(t) \rangle_c = \exp \left\{ -\frac{N}{V} \int \left[1 - \cos \left(\frac{1 - 3 \cos^2(\theta)}{2r^3} \mu_0 \gamma^2 \hbar t \right) \right] r^{D-1} dr dA \right\}$$

Following the same approach we used in 1/2/3 dimensions, we can get

$$\langle G(t) \rangle_c = \exp \left\{ -\frac{\rho}{3} \left(\frac{\mu_0 \gamma^2 \hbar t}{2} \right)^{D/3} \Phi_D S_D \right\} \quad (3.21)$$

$$S_D = \int_0^\infty (1 - \cos u) u^{-(1+D/3)} du = -\cos \left(\frac{D\pi}{6} \right) \Gamma \left(-\frac{D}{3} \right) \quad (3.22)$$

We should notice that this formula comes from Gamma integral, Eqn. B.41, which requires that $-2 < \text{Re } \alpha < 0$. Thus $\langle G(t) \rangle_c$ converges for all dimensions $1 \leq D \leq 5$. One special case is $D = 3$, in this case the $\Gamma(-1)$ gives complex infinity. But the integral itself is still convergent, since

$$\lim_{\alpha \rightarrow -1} \cos \left(\frac{\alpha\pi}{2} \right) \Gamma(\alpha) = -\frac{\pi}{2}.$$

$$\Phi_D = \int_{V_{D-1}} |1 - 3 \cos^2(\theta)|^{D/3} dA \quad (3.23)$$

Here dA is the surface element in $D - 1$ dimension.

3.3 Nondimensionalization

Nondimensionalization is a widely used technique in numerical simulation. By removing physical dimensions, physical problems can be better parameterized and simplified, and scaling-irrelevant features can be better observed. In a spin ensemble, a set of natural scales can also be chosen and set as basic units, in order to get a dimension-free system.

3.3.1 Coherence Time

The free induction decay is also known as T_2 processes, as the dephasing is characterized by a coherence time T_2 . A general decoherence curve in d dimension is given in Eqn. 3.21. It can be written in a more concise form

$$f(t) \propto \exp\left[-\left(\frac{t}{T_2}\right)^{d/3}\right] \quad (3.24)$$

From Eqn. 3.16, Eqn. 3.19 and Eqn. 3.20, the T_2 in 1D/2D/3D can be obtained,

$$3\text{D} : T_2 = \frac{2}{A_0} \frac{9\sqrt{3}}{8\rho\pi^2}, \quad (3.25)$$

$$2\text{D} : T_2 = \frac{2}{A_0} \left[\frac{\rho\pi}{2} \Gamma\left(\frac{1}{3}\right) \right]^{-3/2}, \quad (3.26)$$

$$1\text{D} : T_2 = \frac{2}{A_0} \left[\frac{\rho}{\sqrt{3}} \Gamma(-1/3) \right]^{-3}, \quad (3.27)$$

in which $A_0 = \mu_0\gamma^2\hbar$ is a combined constant. Here it's assumed that the external quantizing field is perpendicular to the spin chain in 1D, and the spin grid in 2D. We can find an interesting property, that the decoherence time of dilute spin ensembles only depends on dimensionality and spin density. The higher the spin density, the shorter the coherence time. In reality, temperature is also a key factor affecting the coherence time[4]. It is not considered in our model as a closed system based on microcanonical ensemble is assumed.

3.3.2 Units Scaling

The coherence time T_2 can be normalized to an arbitrary time unit t_0 , in order to get a dimensionless numerical system. Set $T_2 = 1$ in the unit $\hat{t} = t_0$, then a normalized ρ_0 can be given as

$$3\text{D} : \rho_0 = \frac{2}{A_0 t_0} \frac{9\sqrt{3}}{8\pi^2} \approx 0.39486 [A_0 t_0]^{-1}, \quad (3.28)$$

$$2\text{D} : \rho_0 = \frac{2^{5/3}}{\pi \Gamma(\frac{1}{3})(A_0 t_0)^{2/3}} \approx 0.37723 [A_0 t_0]^{-2/3}, \quad (3.29)$$

$$1\text{D} : \rho_0 = \frac{\sqrt[3]{2}\sqrt{3}}{\Gamma(-\frac{1}{3})(A_0 t_0)^{1/3}} \approx 0.53712 [A_0 t_0]^{-1/3} \quad (3.30)$$

Thus, unit for the density in d dimensions can be rescaled as $[A_0 t_0]^{-d/3}$. Respectively, the unit of length will be $\hat{r} = [A_0 t_0]^{1/3}$. The dipolar coupling strength D_{ij} and effective fluctuation of the magnetic field β_ζ both have a dimension in frequency, thus their units should be $\hat{\omega} = t_0^{-1}$. All the numerical in the following chapters of this thesis will be given in such a system of units.

Minimal Threshold

A threshold for minimal distance, a , is needed for continuum approximation to avoid singularity in coupling strength. It should be characterized by the minimum lattice constant, which is at the scale of angstroms in solids. The rescaled unit of length \hat{r} depends on the choice of time unit t_0 and is thus an arbitrary variable. But we can still give a rough estimation about what should be the scale of a .

Typical nuclear T_2 in solid system is usually at the scale of microseconds [43]. Assume that $t_0 = 1 \mu s$, then the unit length will be $\hat{r} = [\mu_0 \gamma^2 \hbar t_0]^{1/3} \approx 7.4 \times 10^{-9}$, thus a minimum threshold at $a = 0.1 \sim 0.05$ is resonable.

Filling Fraction

The filling fraction can be calculated as $f = \rho a^d$ providing that a approximately equals lattice constant. At $a = 0.1$, $d = 3$, $f \simeq 500$ ppm. This is a reasonable approximation. In practice, the residual concentration of ^{29}Si spins in purified isotopes is typically $800 \sim 900$ ppm [47][36], while the natural abundance of ^{15}N is approximately 0.4%, the spin concentration in NV center system can be lower after fabrication process like chemical vapor deposition.

3.4 Normalized Coherence Time

The technique of rescaling can be used to choose a fixed set of parameters for the spin ensemble. In our model, an ensemble consisting spin clusters of all possible disorder realizations can be defined by a set of parameters, including spin density, number of spins, or equivalently the max range of spin distribution, and minimum distance threshold between the central qubit and the bath spins. These parameters must be properly defined to make the model meaningful to experiments.

Given the discussions about , a set dimensionless parameters of the model can be choosed as shown in Table. 3.2. The ensembles are normalized in terms of coherence time. We choose

dimension [d]	spin density [ρ]	lattice const [a]	max range [R]	spin number [n]
3	0.39486	0.1	10	1653
2	0.37723	0.05	30	1066
1	0.53719	0.05	200	214

Table 3.2: Parameters of Spin Ensembles in 1D/2D/3D

this approach of normalization because that dynamic processes will be the main focus of this thesis. Dynamical processes and effects of quantum control protocols can be better observed in such a time scale.

The ensemble-averaged T_2 relaxations from the normalized models can be checked as a verification of the model. As shown in Fig. 3.3, the numerical results acquired from Monte-Carlo sampling match well with analytical predictions.

3.4.1 Ensemble Averaged Noise

As shown in the Section. 2.6.2, the effective noise of a typical spin cluster should be quasi-Gaussian. Assume the noise is exactly Gaussian, then the ensemble-averaged effective noise can be given as

$$P(B) = \frac{1}{\sqrt{2\pi b^2}} \exp\left(-\frac{B^2}{2b^2}\right) \quad (3.31)$$

For an ensemble of clusters given by different disorder realizations, their noises are given by a set of Gaussians. It's proved that linewidths of the Gaussians b follow the distribution

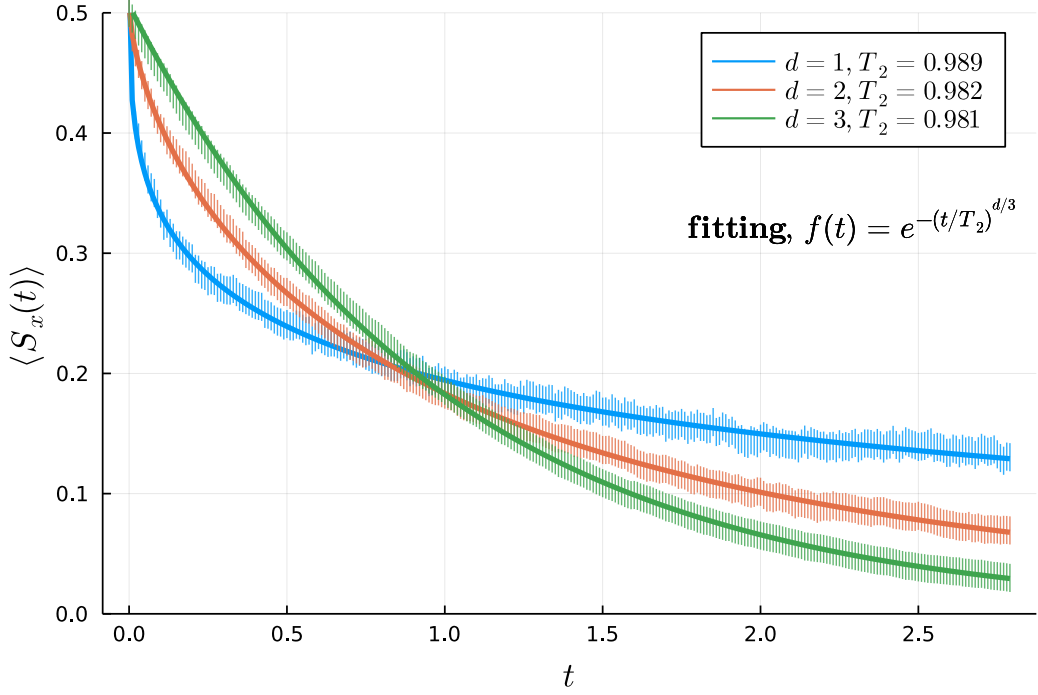


Figure 3.3: Fitted analytical T_2 relaxations compared with Monte-Carlo sampled results.

The relaxation curves are evaluated by Monte-Carlo sampling, with $M' = 4000$ disorder realizations (DRs) and $N' = 1000$ spin configurations. The numerical data points are plotted as vertical lines and the fitting of analytical result is plotted as solid curves. The original figure without fitting is attached in C.7.

below in three dimension[13],

$$P(b) = \frac{1}{b^2} \sqrt{\frac{2}{\pi}} \Gamma \exp\left(-\frac{\Gamma^2}{2b^2}\right). \quad (3.32)$$

in which Lorentzian linewidth Γ is determined by the parameters of the ensemble (abundance, etc). Take the ensemble average of the noise,

$$P(B) = \int_0^\infty P(b)P(B)db = \frac{\Gamma}{\pi(B^2 + \Gamma^2)}, \quad (3.33)$$

the result is a Cauchy distribution characterized by Lorentzian linewidth Γ . Derivation of the above formulas is given in the Appendix. B.10. Numerical results acquired from Monte-Carlo sampling match well with the Lorentzian noise, which is shown in Fig. 3.4. It should be noticed that the Lorentzian distribution is only an approximation to the real noise distribution in the 3D system because the cluster distribution is not precisely Gaussian, as shown by the Van Vleck momentum methods. There is also a small deviation between Lorentzian prediction and the numerical result at $|\beta| < 1$.

For 3D ensemble, the corresponding ensemble averaged free induction decay curve is given by the Fourier transform of the noise distribution.

$$\langle S_x(t) \rangle = \int_{-\infty}^{\infty} \langle S_x(B; t) \rangle P(B)dB = \frac{1}{2} \text{Re} \int_{-\infty}^{\infty} e^{-iBt} P(B)dB \quad (3.34)$$

The characteristic function of Lorentzian noise is

$$F(t) = \int_{-\infty}^{\infty} e^{-iBt} \frac{\Gamma}{\pi(B^2 + \Gamma^2)} dB = e^{-\Gamma|t|}. \quad (3.35)$$

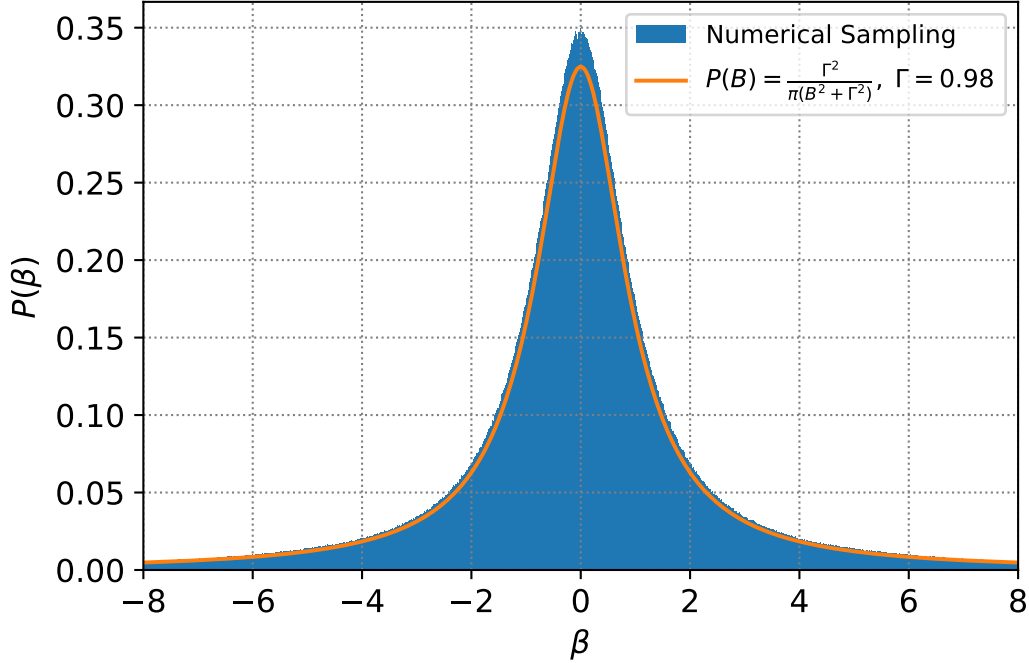


Figure 3.4: Effective noise distribution in 3D compared with analytical prediction.

The coherence time T_2 is defined as $F(t) = e^{-|t|/T_2}$. Thus $T_2 = 1/\Gamma$ for a Lorentzian noise. This result is verified by the previous analytical solution given by Eqn. 3.20.

In 2D and 1D, analytical approximations of the noise is not available. Numerical simulation is needed to analyze the system in low dimension. The effective noise distribution obtained from Monte-Carlo sampling in low dimensions is displayed in Fig. 3.6 and Fig. 3.5. The distributions of effective noise are heavily tailed, which can be characterized by the statistical indicator kurtosis,

$$\text{Kurt}[X] = \text{E} \left[\left(\frac{X - \mu}{\sigma} \right)^4 \right] \quad (3.36)$$

in which μ is the mean value and σ is the standard deviation. Normal distribution is regarded as a standard for non-tailed, with $\text{Kurt}[X] = 3$. Based on this condition, excess kurtosis $\mathcal{K}[X] = \text{Kurt}[X] - 3$ is used to characterize the tailedness of a distribution.

As given in Fig. 3.5, the excess kurtosis of the effective noise is much larger than zero. Hence there is a large probability to produce outliers or anomalies in sampling, which makes the numerical approach more unstable. Yet, it's a quite counter-intuitive fact that $\mathcal{K}_{3D} > \mathcal{K}_{2D} > \mathcal{K}_{1D}$, while $\sigma_{3D} < \sigma_{2D} < \sigma_{1D}$ in terms of deviation. The 1D distribution is much sharper in shape compared with the 3D case, and it owns a fatter tail compared with the 3D. However, its kurtosis is lower than the quasi-Lorentzian distribution of 3D.

$$\lim_{a \rightarrow \infty} \int_{-a}^a x^2 \frac{\Gamma}{\pi(\Gamma^2 + x^2)} dx = \lim_{a \rightarrow \infty} \frac{2\Gamma}{\pi} \left(a - \Gamma \tan^{-1} \left(\frac{a}{\Gamma} \right) \right) = \infty \quad (3.37)$$

providing $\Gamma > 0$, similarly

$$\lim_{a \rightarrow \infty} \int_{-a}^a x^4 \frac{\Gamma}{\pi(\Gamma^2 + x^2)} dx = \lim_{a \rightarrow \infty} \frac{2\Gamma}{3\pi} \left(a^3 + 3\Gamma^3 \tan^{-1} \left(\frac{a}{\Gamma} \right) - 3a\Gamma^2 \right) = \infty. \quad (3.38)$$

In fact, the Cauchy-Lorentzian distribution owns infinite second-order momentum and fourth-order momentum, which makes the distribution much harder to predict, as shown above. **The tail extremity is a key feature of our system, strong singularities will be present due to such kind of long-tailed distribution.**

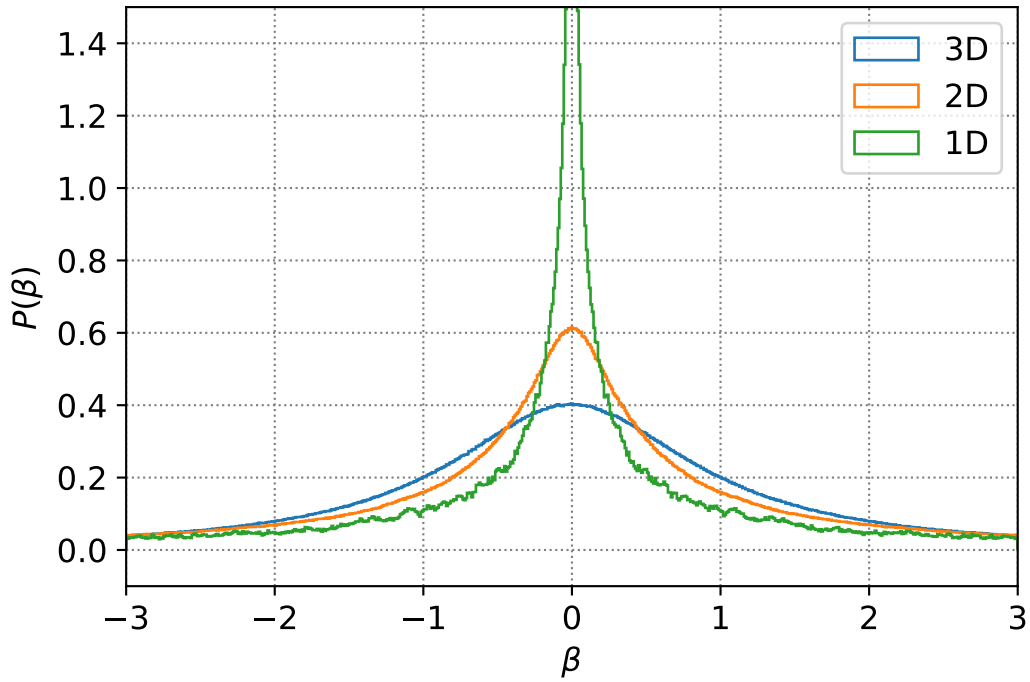


Figure 3.5: Distribution of ensemble averaged noise at different dimensions.

Distribution of effective noise in linear scale, with sampling size $M' = 2 \times 10^5$ and $N' = 1000$. The standard deviations of the distributions are $\sigma_{3D} = 17.639$, $\sigma_{2D} = 153.783$ and $\sigma_{1D} = 419.558$ for 3D, 2D, 1D, separately. Relative kurtosis of the distributions are $\mathcal{K}_{3D} = 419.972$, $\mathcal{K}_{2D} = 265.065$, $\mathcal{K}_{1D} = 39.948$.

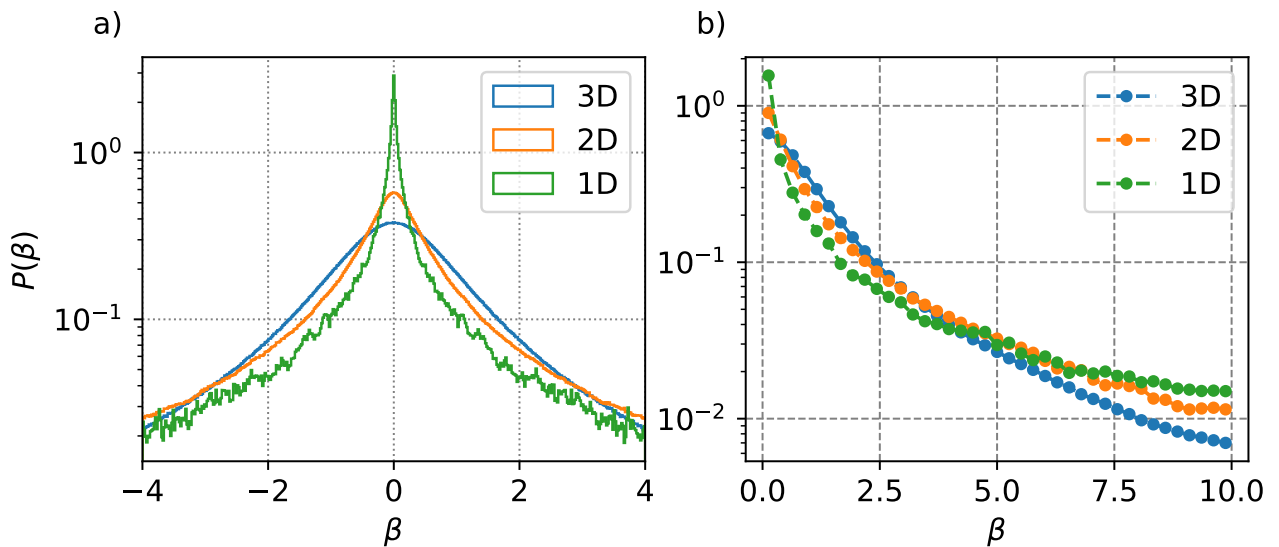


Figure 3.6: Distribution of ensemble averaged noise at different dimensions, log scale.

a): Distribution of effective noise in log scale. b): Long tails of the same noise in log scale, taken absolute value.

Chapter 4

Driving a Bath-Coupled Qubit

4.1 Control Hamiltonian

This chapter will introduce the control of spin qubits with driving pulses, and then study how the driving will be affected by the coupling between qubits and the environment. As mentioned in Chapter. 1, Rabi driving is the key approach for manipulating spins and can be generalized to many other modern quantum hardware. Rabi driving on spin qubits is achieved via an external AC magnetic field, which is resonant with the Larmor frequency ω_0 of the target qubit. The Hamiltonian for a cluster of spins under the driving field can be given as

$$\mathcal{H}_C(t) = -\hbar \sum_j \gamma_j B [\cos(\omega_c t + \phi) I_j^x + \sin(\omega_c t + \phi) I_j^y]. \quad (4.1)$$

in which ϕ is the phase of the AC field, and B is the amplitude. Then the total Hamiltonian for the cluster under a driving field is $\mathcal{H} = \mathcal{H}_Z + \mathcal{H}_D + \mathcal{H}_C(t)$, in which the \mathcal{H}_Z is the magnetization energy and \mathcal{H}_D is the dipolar interactions, $\mathcal{H}_C(t)$ is the oscillating driving field. Here we need to notice that we are discussing the Hamiltonians in the laboratory frame. Perform the rotating frame transformation then we can get the rotating frame Hamiltonian.

For a spin cluster representing a spin qubit in bath, the external global field drives not only the spin qubit, but also the bath spins in the environment. Yet, only the spin qubit is concerned in experiment. Assume the qubit we want to control is labeled by 0, its Hamiltonian in the rotating frame can be given by

$$\begin{aligned} \mathcal{H}_0 = & \hbar(\omega_0 - \tilde{\omega}_0) I_0^z + \sum_{j=1}^N 2D_j I_j^z I_0^z \\ & - \hbar\gamma_0 B [I_0^x \cos((\omega_C - \tilde{\omega}_0) t + \phi) + I_0^y \sin((\omega_C - \tilde{\omega}_0) t + \phi)]. \end{aligned} \quad (4.2)$$

Derivation of the equation is listed in Appendix. B.8

Resonant Driving

Ignore the environmental coupling. Then the driving frequency ω_C can be set at a resonant frequency to $\omega_C = \tilde{\omega} \simeq \omega_0$, such that the time-dependent control Hamiltonian is equivalent to a static driving in the rotating frame, as shown below.

$$\mathcal{H} = -\hbar\gamma_0 B (I_0^x \cos \phi + I_0^y \sin \phi). \quad (4.3)$$

The Zeeman term is eliminated. The Larmor frequencies of nuclear spins range from approximately 40MHz to 170MHz, which is in the range of radiofrequency. This case is known as *resonant driving*.

The evolution unitary of such a driving Hamiltonian is given by

$$U(t) = e^{-i\mathcal{H}t/\hbar} = e^{\gamma_0 B t/2 (\vec{\sigma} \cdot \vec{n})} = \cos\left(\frac{\gamma_0 B t}{2}\right) + i \sin\left(\frac{\gamma_0 B t}{2}\right) (\vec{\sigma} \cdot \vec{n}) \quad (4.4)$$

in which $\vec{n} = (\cos \phi, \sin \phi, 0)$ is a unit vector on the X-Y equator defined by the direction of the driving field ϕ . $\vec{\sigma} = (\sigma_x, \sigma_y, \sigma_z)$ is the vector of Pauli matrices. From the view of physical images, the state of a qubit equals a unit vector on the Bloch sphere. Then the unitary represents a rotation of the state vector along the driving direction \vec{n} , which can be visualized as

In the ideal situation of resonant driving, any single-qubit gate can be perfectly constructed from such a Hamiltonian with properly tuned parameters (ϕ, B, t) . The driving is also known as XY driving since the driving axis \vec{n} lies on the XY equator. More details of quantum gates will be covered in later chapters of the thesis.

Non-Resonant Driving

In reality, the driving is always *non-resonant* since the driving frequency can't be precisely set at the Larmor frequency of qubit. In reality, Larmor frequency is shifted by both the local field inhomogeneity ΔB_0 and an effective magnetization β produced by the dipolar coupling, $\omega'_0 = \gamma_0(B_0 + \Delta B_0) + \beta$.

$$\mathcal{H}' = \hbar(\gamma_0 \Delta B_0 + \beta) I_0^z - \hbar \gamma_0 B (I_0^x \cos \phi + I_0^y \sin \phi). \quad (4.5)$$

Suppose that β is static and there is no fluctuation, then the driving is still a unitary process. Denote $\gamma_0 \Delta B_0 + \beta$ as $\Delta\omega$, the unitary can be given as

$$U'(t) = e^{-i\mathcal{H}'t/\hbar} = e^{\Omega t/2 (\vec{\sigma} \cdot \vec{n}')} = \cos\left(\frac{\Omega t}{2}\right) + i \sin\left(\frac{\Omega t}{2}\right) (\vec{\sigma} \cdot \vec{n}') \quad (4.6)$$

in which $\Omega = \sqrt{(\gamma_0 B)^2 + \Delta\omega^2}$ is a shifted Rabi frequency, with

$$\vec{n}' = \left(\cos \phi \frac{\gamma_0 B}{\Omega}, \sin \phi \frac{\gamma_0 B}{\Omega}, \frac{\Delta\omega}{\Omega} \right).$$

Obviously, there will be a small shift in the Rabi frequency as well as the driving direction. The state will not precisely rotate along the axis \vec{n} on the XY plane, but along a new twisted axis \vec{n}' .

Yet, if we consider the fluctuation of effective field β produced by the environment, then the evolution of the qubit will be a noisy quantum process instead of a unitary. This is introduced in the following sections.

When a global driving field is applied on a cluster of spins, only the spin(qubit) at the frequency of the driving field will be driven resonantly under the ideal condition, while all other spins will be driven non-resonantly.

4.2 Rabi Driving with Effective Noise

Rabi driving is always a noisy quantum process in reality, which can be modeled using the same approach given in Section. 2.5.1. Environmental coupling between the spin qubit and bath spins can be treated as a continuous noise β , which obeys the Gaussian/Lorentzian distribution. Integrating over the noise density will provide a damped Rabi driving curve.

Gaussian noise for a spin cluster

From the above results, we have seen that the effective noise from environmental spins obeys a Gaussian distribution. Thus we can study the Rabi oscillation starting with the noisy Hamiltonian of the central spin, given by a modified version of Eqn. 4.5

$$\mathcal{H} = \beta S_z + h S_x.$$

in which h characterizes the driving strength γB , in the dimension of frequency. Here we dropped all the irrelevant constants such as \hbar and γ to make the derivation more concise. As shown in the discussion of Van Vleck momentums, section 2.6, the distribution of β is approximately Gaussian,

$$P(\beta) = \frac{1}{\sqrt{2\pi}b} e^{-\frac{\beta^2}{2b^2}} \quad (4.7)$$

In a strong driving limit, $h \gg b$, an analytical description of Rabi driving is available.

$$S_z(t) = \frac{1}{2} \operatorname{Re} F(t) = A \cos(ht + \phi), \quad S_y(t) = \frac{1}{2} \operatorname{Im} F(t) = -A \sin(ht + \phi), \quad (4.8)$$

in which $F(t)$ is

$$F(t) = \int_{-\infty}^{\infty} e^{-i\Omega t} P(\beta) d\beta = \frac{e^{-iht}}{\sqrt{1 + i\frac{b^2 t}{h}}}, \quad (4.9)$$

and

$$A = \frac{1}{2} \left(1 + \frac{b^4 t^2}{h^2}\right)^{-1/4}, \quad \phi = \frac{1}{2} \arctan\left(\frac{b^2 t}{h}\right) \quad (4.10)$$

Lorentzian noise for an ensemble average

The ensemble average Rabi curve can also be derived from the Lorentzian distribution

$$\begin{aligned} S_z(t) &= \frac{1}{2} \operatorname{Re} \int_{-\infty}^{\infty} P(B) e^{i\Omega t} dB = \frac{1}{2} \operatorname{Re}\{F(t)\} \\ S_y(t) &= \frac{1}{2} \operatorname{Im} \int_{-\infty}^{\infty} P(B) e^{i\Omega t} dB = \frac{1}{2} \operatorname{Im}\{F(t)\} \end{aligned}$$

The function $F(t)$ is given by

$$F(t) = \int_{-\infty}^{\infty} P(B) e^{i\Omega t} dB \approx e^{iht - \frac{i\Gamma^2 t}{2h}} \operatorname{erfc}\left(\frac{1-i}{\sqrt{2}} \sqrt{\frac{t}{2h}} \Gamma\right). \quad (4.11)$$

The derivation of the above equations is given in B.11. A more precise approximation in the regime of weak driving can be given using Mathematica, as appended in B.13

As a verification, the analytical Rabi curve is compared with the numerical result obtained from Monte-Carlo methods, which is given in the later Section. 4.3. The numerical results match well with the analytical approximation at $h = 50$. Yet, there is still a small discrepancy at the crests and troughs of the wave, due to the truncation of high order terms in the approximation. It should be noticed that the Lorentzian distribution is just an approximation of real noise density in 3D ensembles. In 2D and 1D cases, no analytical solution is available yet. Thus numerical approach will be necessary.

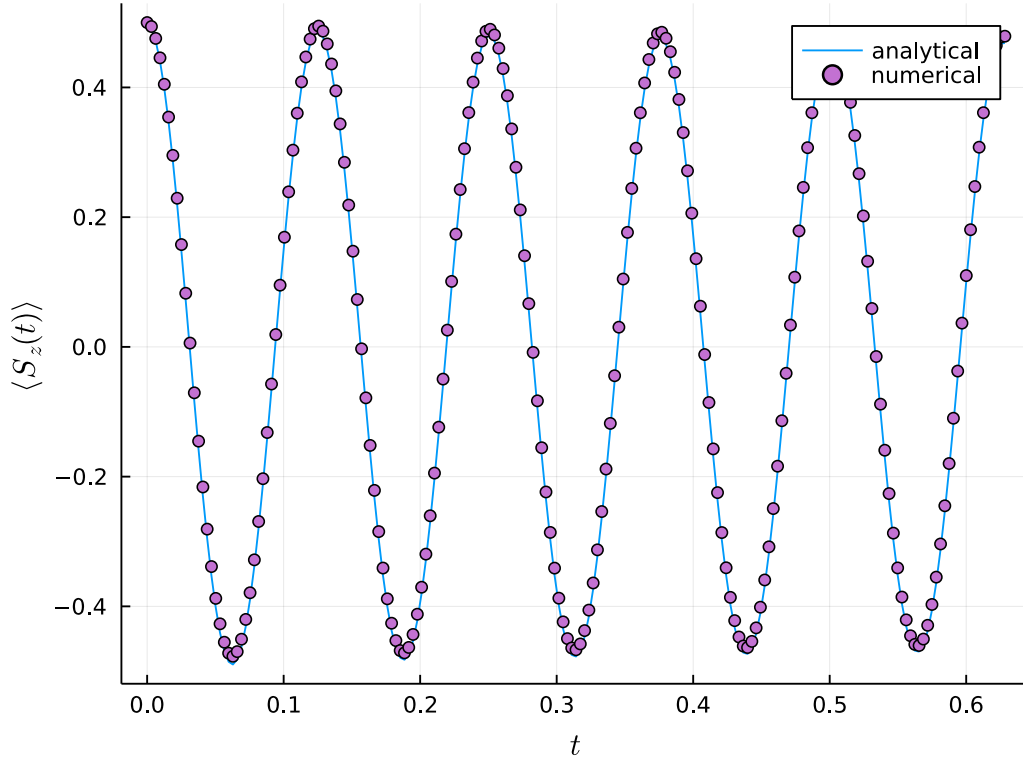


Figure 4.1: Averaged Rabi oscillation over an ensemble of 3D spin clusters at $h = 50$. The numerical curve is sampled via Monte-Carlo methods on $M' = 3000$ disorder realizations (DR) and $N' = 500$ spin configurations for each DR. The analytical curve is given by Eqn. 4.11.

4.3 Rabi Driving from Numerical Sampling

We can write the total Hamiltonian in the rotating frame assuming that the Zeeman terms are already eliminated. ϕ is free to choose so we set the driving field at x axis. For convenience, we drop constant \hbar in the following derivations. The Hamiltonian on the central qubit can thus be given as

$$\mathcal{H} = \sum_j 2D_j S_j^z S_0^z - h S_0^x. \quad (4.12)$$

Following the same approach shown in Section. 2.5.1, the effective unitary projected on a bath eigenstate can be given as

$$U_p(t) = \langle p | e^{-i\mathcal{H}t} | p \rangle = \cos(\omega_p t) - i \sin(\omega_p t) (\vec{n}_p \cdot \vec{\sigma}) \quad (4.13)$$

in which \vec{n}_p is the effective direction of driving field, ω_p is half of the Rabi frequency.

$$\vec{n}_p = (n_{p,x}, 0, n_{p,z}) = \left(\frac{h}{\Omega_p}, 0, \frac{\beta_p}{\Omega_p} \right), \quad \omega_p = \Omega_p/2, \quad \Omega_p = \sqrt{h^2 + \beta_p^2}. \quad (4.14)$$

The central qubit are prepared at $|0\rangle$, which is at z axis in Rabi oscillation. Thus the initial state of the central spin is $\rho_0 = |0\rangle\langle 0| = \frac{1}{2}\mathbb{1} + S_z$. The expectation of $S_z(t)$ under Rabi driving is given by,

$$\langle S_z(t) \rangle = \frac{1}{2^n} \sum_p \text{Tr} \langle p | S_0^z | p \rangle = \frac{1}{2^n} \sum_p \text{Tr} [S_z U_p(t) S_z U_p(t)^\dagger]. \quad (4.15)$$

Define the observable on a bath state as $\text{Tr} \langle p | S_0^z | p \rangle = f_z^{(p)}(t)$, then

$$f_z^{(p)}(t) = \text{Tr} [S_z U_p(t) S_z U_p(t)^\dagger] = \frac{1}{2} [\cos^2(\omega_p t) + \sin^2(\omega_p t) (n_{p,z}^2 - n_{p,x}^2)], \quad (4.16)$$

Similarly, we can derive $S_x(t)$ and $S_y(t)$ in the Schödinger picture

$$\langle S_y(t) \rangle = \frac{1}{2^n} \sum_p f_y^{(p)}(t) = -\frac{1}{2^n} \sum_p n_{p,x} \sin(\omega_p t) \cos(\omega_p t), \quad (4.17)$$

$$\langle S_x(t) \rangle = \frac{1}{2^n} \sum_p f_x^{(p)}(t) = \frac{1}{2^n} \sum_p n_z n_x \sin^2(\omega_p t). \quad (4.18)$$

Detailed derivation of the above results is given in Appendix. B.12. Take disorder realizations into consideration, the above results can be further extended to an ensemble average by replacing label p with the combinational index $\zeta = (p, \xi)$, where ξ is the label of disorder realization. Thus the ensemble average Rabi curve is given by

$$F_z(t) = \frac{1}{\mathcal{M}} \sum_{\zeta=1}^{\mathcal{M}} f_z^{(\zeta)}(t) = \frac{1}{\mathcal{M}} \sum_{\zeta=1}^{\mathcal{M}} [\cos^2(\omega_\zeta t) + \sin^2(\omega_\zeta t)(n_{\zeta,z}^2 - n_{\zeta,x}^2)] \quad (4.19)$$

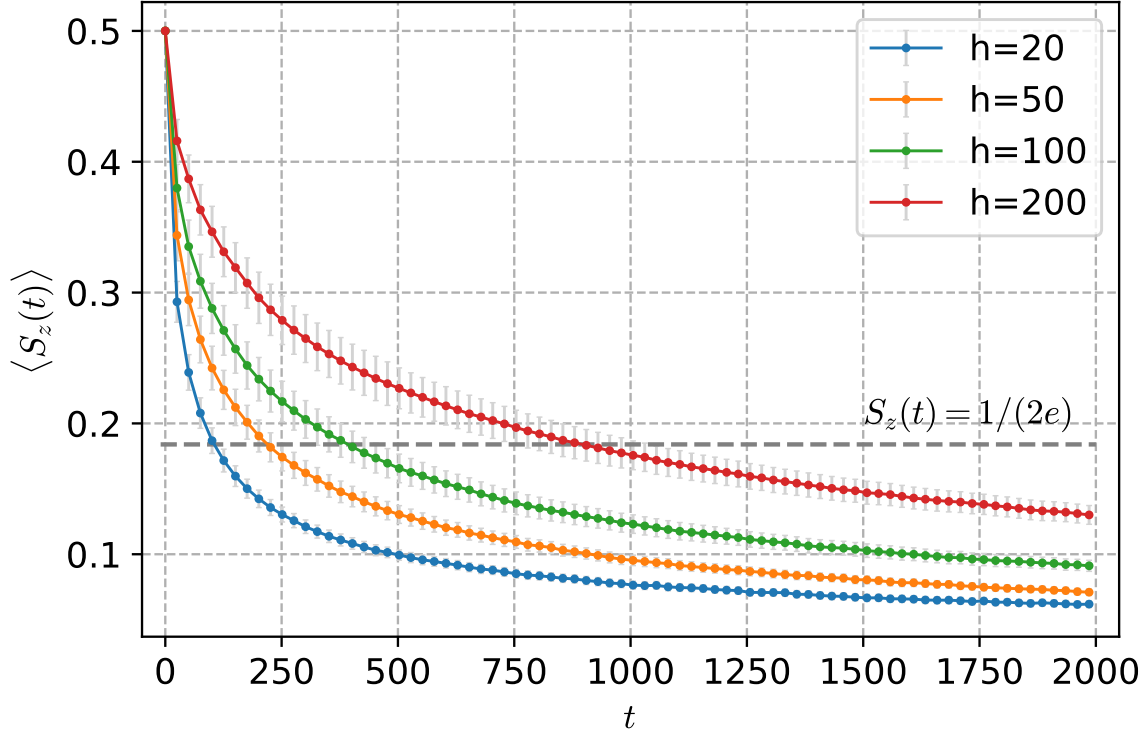
in which we dropped the prefactor $I = \frac{1}{2}$, which is from the spin 1/2. With the formulas above, the ensemble-averaged Rabi driving curve can be effectively evaluated from Monte-Carlo sampling.

4.4 Damping of Continuous Driving

The first specialized topic we want to discuss is a continuous Rabi driving with constant driving strength h . Experimentally, such a continuous driving can serve as a method to prolong the effective decoherence time $T_{2,R}$ of spin qubits. As shown in Eqn. 4.8, the damped Rabi oscillation with Gaussian noise is enveloped by a function $A(t)$, this envelope decays very slowly so the coherence of qubit can be preserved for a very long time. The effective T_{2*} given by this continuous nutation is much longer compared with the original coherence time of the qubit. As a dynamical decoupling approach, the simple continuous driving is robust against various noises, such as magnetic, electric, and temperature fluctuations[34]. It can also be used to construct a decoupling-protected quantum gate[55].

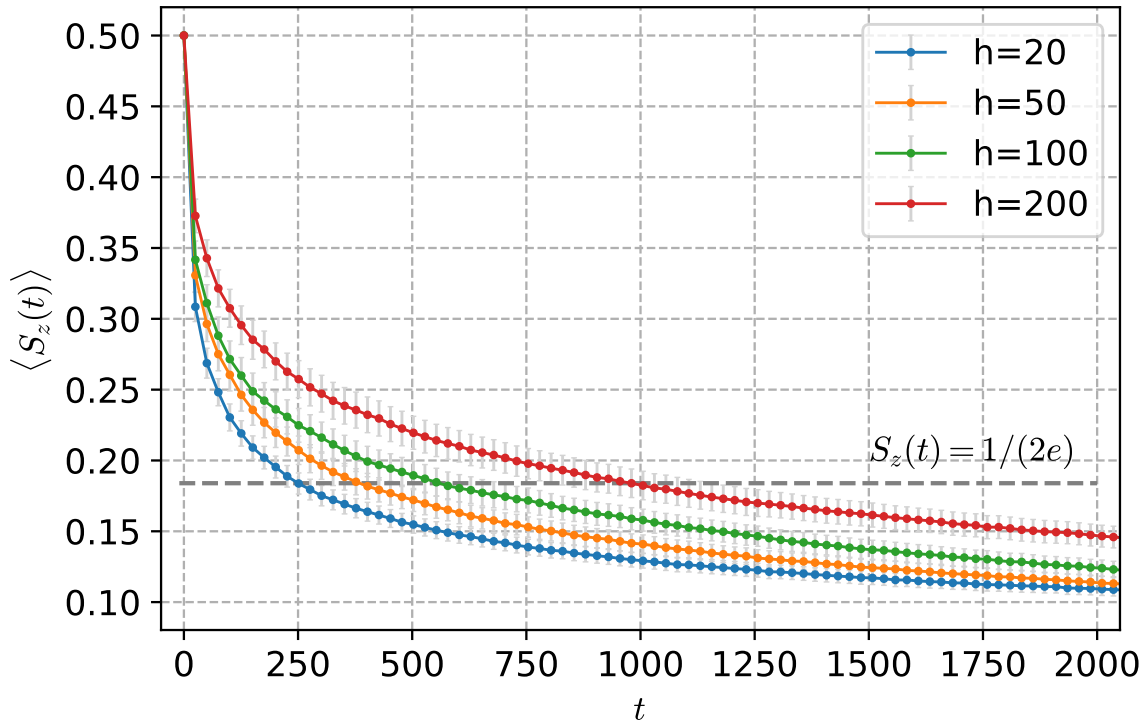
4.4.1 Rabi Envelope

The envelope of Rabi oscillation can be extracted from an array of oscillating points by taking the maximum of each period. Envelopes of averaged Rabi driving for 3D, 2D, and 1D ensembles, obtained from Monte-Carlo sampling are shown in Fig. 4.2a, Fig. 4.2b and Fig. 4.3. The horizontal line marks the $1/e$ threshold of amplitude decay. The x coordinates of crossing points, where Rabi curves intersect with the $1/e$ line, are the $T_{2,R}$ of corresponding curves. Using the continuous driving, the effective coherence time $T_{2,R}$ is improved by 10^2 to 10^3 at magnitude in 2D and 3D (remember that the original coherence time is normalized to 1). However, Rabi driving in one dimension demonstrates a very strong singularity, the decay of oscillation amplitude is quite slow that $1/e$ decay can't be observed in a short time. For this reason, further analysis is needed to understand its asymptotic behavior in the long-time regime.



(a) Envelope of ensemble averaged Rabi oscillation in 3D.

Coherence time at $1/e$ decay are $T_{2,R} = 100, 226, 402, 905$, for $h = 20, 50, 100, 200$. Monte-Carlo sampling size is given by $M' = 2000$, $N' = 500$.



(b) Envelope of ensemble averaged Rabi oscillation in 2D.

Coherence time at $1/e$ decay are $T_{2,R} = 251, 377, 553, 980$, for $h = 20, 50, 100, 200$. Monte-Carlo sampling size is given by $M' = 3000$, $N' = 500$.

Figure 4.2: Envelope of ensemble averaged Rabi oscillation in 3D and 2D, obtained from numerical sampling.

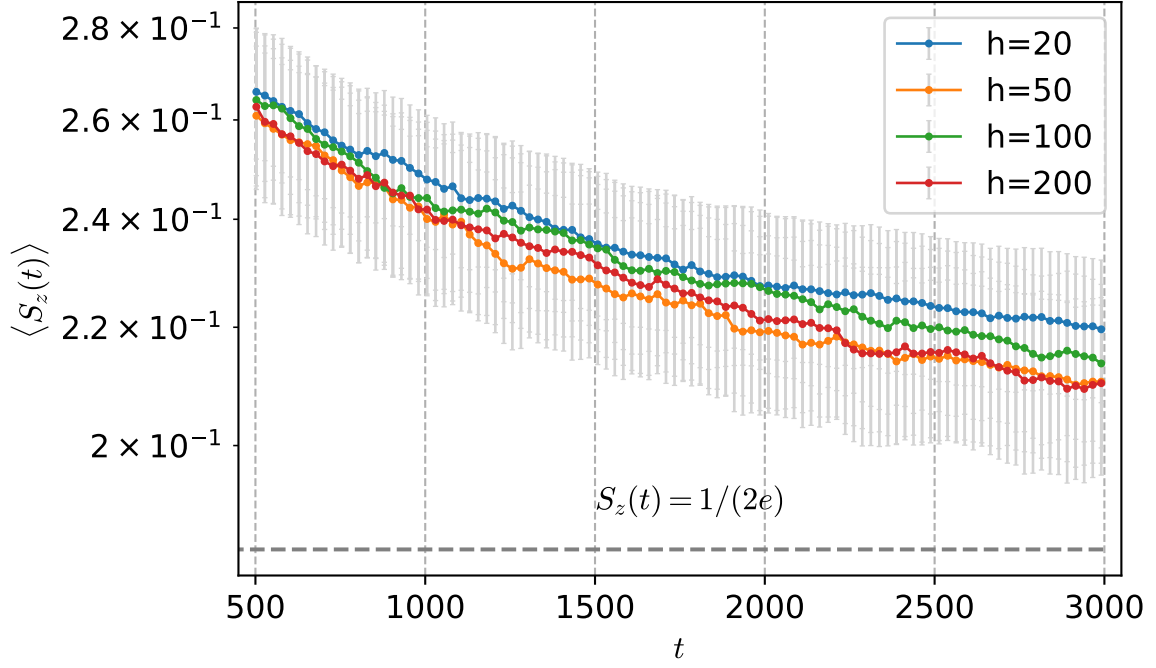


Figure 4.3: Envelope of ensemble averaged Rabi oscillation in 1D, shown in log scale.

The averaged Rabi oscillation decays very slowly in one dimension, $1/e$ decay is not observed at short time. Further analysis is needed to understand its asymptotic behavior at long time. The Monte-Carlo sampling size is given by $M' = 8000$, $N' = 500$.

4.4.2 Asymptotic Behavior

Exponential Approximation

The approximate solution of ensemble-averaged Rabi driving owns a quite complicated form, as shown in Eqn. 4.11. Yet, the behavior of the function $\langle S_z(t) \rangle$ can be much simplified at a limit $t = 0$ or $t = \infty$ by taking a series expansion and truncating high order terms. Following this idea, a simple and intuitive model can be found to describe the behavior in the short-time regime and long-time regime, as shown below.

Short time model:

$$S_z^{(1)}(t) \approx \frac{1}{2} \left[1 - \left(\frac{t}{T_{2,R}} \right)^{d/6} \right], \quad (4.20)$$

$$\Rightarrow F_1(t) = \log \left(1 - 2S_z^{(1)}(t) \right) = \frac{d}{6} (\log t - \log T_{2,R}).$$

Long time model:

$$S_z^{(2)}(t) \approx \frac{1}{2} (t/T_{2,R})^{-d/6}, \quad (4.21)$$

$$\Rightarrow F_2(t) = \log \left(2S_z^{(2)}(t) \right) = -\frac{d}{6} (\log t - \log T_{2,R}).$$

A linear relation $y = kx + b$ is expected in log-log scale, if we replace $x = \log t$ and $F(t) = y$, in which $|k| = d/6$ and $|b| = |k| \log T_{2,R}$. Fig. 4.4 displays the results obtained from a linear regression $y = kx + b$ in log-log scale, at $h = 100$ in an 3D ensemble. Both long time model and short time model are plotted in the figure. A clear transition period can be observed between the short time behavior and long time behavior, as marked by t_1 .

Pointer State

In long time, the damped Rabi oscillation will decay to a equilibrium state called pointer state.

$$\lim_{t \rightarrow \infty} S_z(t) = n_z^{(b)} S_z(0), \quad n_z^{(b)} = \frac{b}{\sqrt{b^2 + h^2}}, \quad (4.22)$$

in which b is the linewidth of noise density. Thus the pointer state should be proportional to the noise linewidth when the driving field is much larger than the noise. For the ensemble-averaged driving in 3D, the noise density is a Lorentzian with normalized linewidth $b = \Gamma = 1$, thus the pointer state should be $S_z(t) = 1/\sqrt{h^2 + 1} \approx 1/h$. Such a pointer can be observed in the numerical results at the long time limit of 3D ensembles, as shown in Fig. 4.4. The analytical prediction matches well with the numerical results.

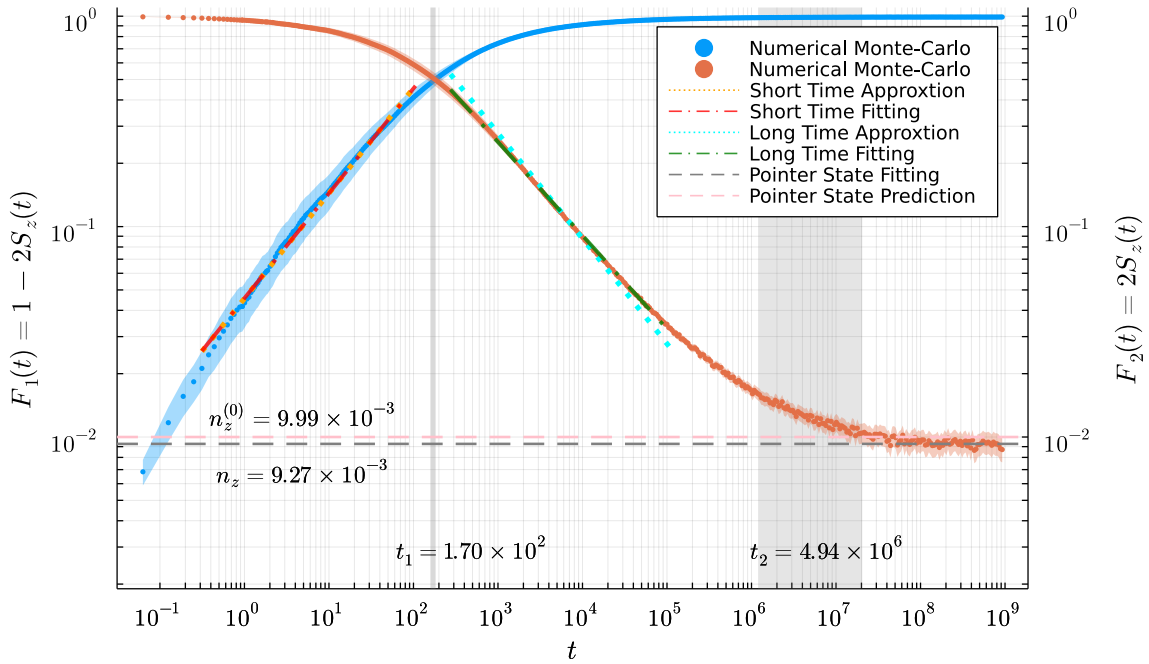


Figure 4.4: Ensemble averaged Rabi oscillation envelope in log scale. **3D, $h=100$** .

Rabi envelope is obtained at $M' = 10000$, $N' = 500$. The short time fitting result is $k = 0.4984$, $b = -1.3401$. The long time fitting result is $k = -0.4442$, $b = 0.7345$.

For 2D and 1D cases, larger linewidths can be expected due to larger standard deviations, as shown in the previous chapter, Fig. 3.5. Due to the large divergence of effective noise in 1D and 2D, the driving might happen in a weak driving regime where $h/b \sim 1$. In such a case a large component of the pointer state can be observed at the long time limit, as shown in Fig. 4.6. At 1D, $h = 50$, the pointer state is about $n_z = 0.166$, which means the effective linewidth of 1D noise density is about $\Gamma \approx 8.1$. Similarly, a clear transition period between the long-time decay and equilibrium pointer state can be observed, which is marked by t_2 . Even if a fixed linewidth can not be found, larger pointer states indicate larger statistical fluctuations in the noise.

More figures of $h = 200, 100, 50, 20$ is given in the Appendix. C. From the figures, it can be concluded that the larger the driving field, the longer the coherence. Both t_1 and t_2 will be prolonged under a stronger driving.

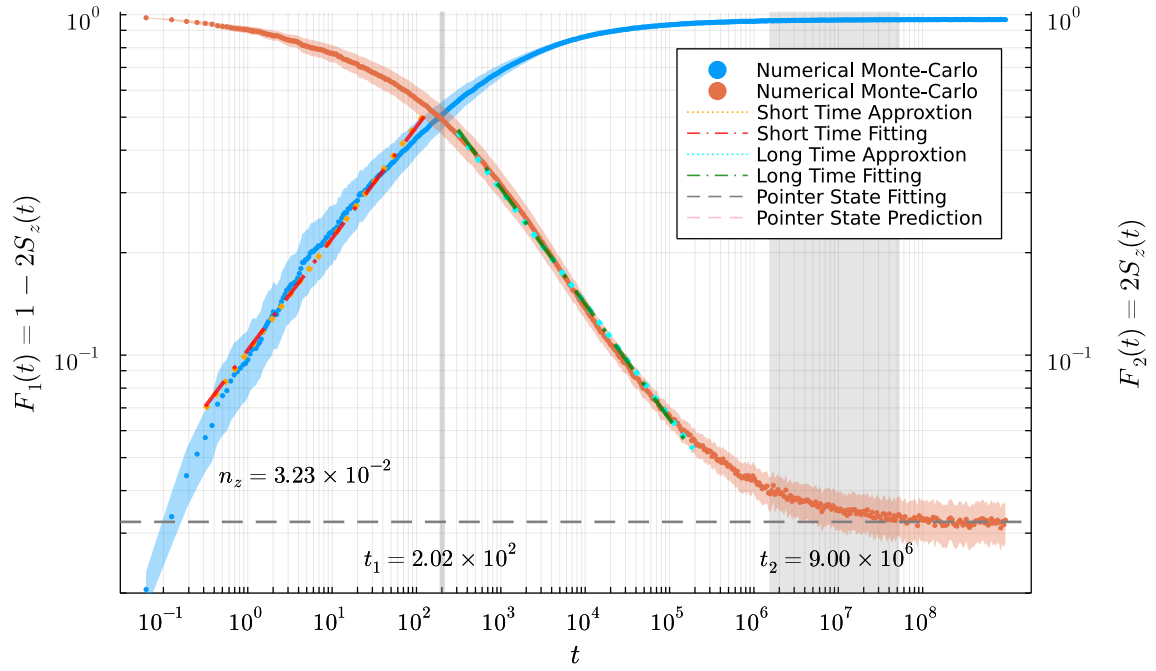


Figure 4.5: Ensemble averaged Rabi oscillation envelope in log scale. **2D, $h=100$** .

Rabi envelope is obtained at $M' = 10000$, $N' = 500$. The short time fitting result is $k = 0.3281$, $b = -0.9852$. The long time fitting result is $k = -0.339$, $b = 0.5069$.

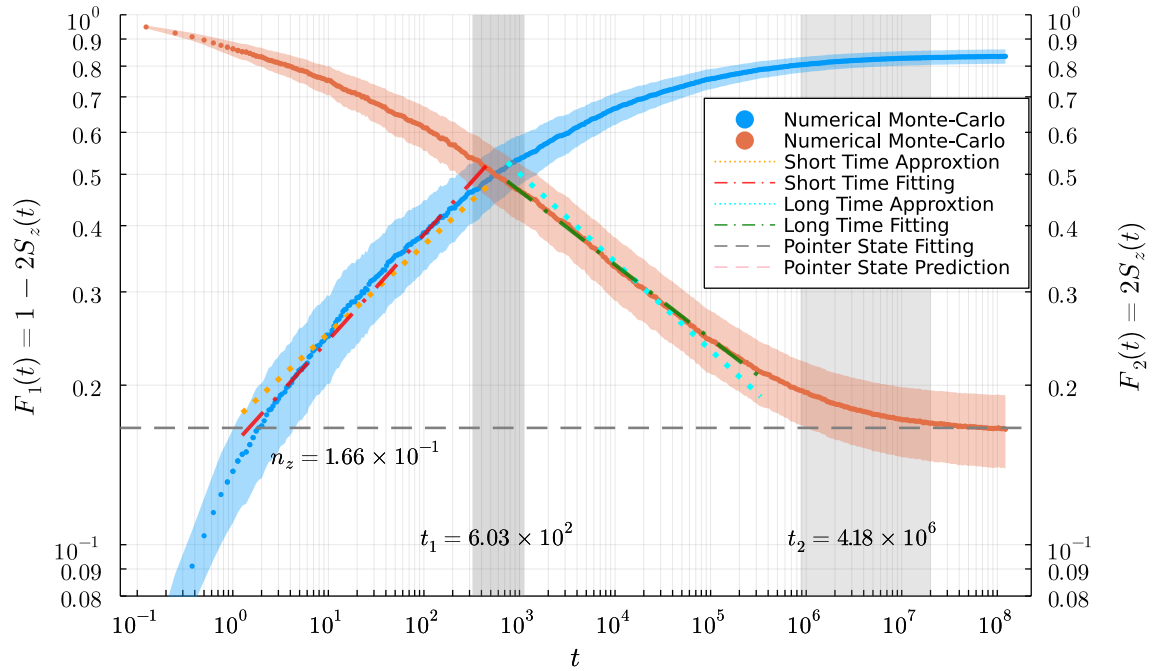


Figure 4.6: Ensemble averaged Rabi oscillation envelope in log scale. **1D, $h=50$** .

Rabi envelope is obtained at $M' = 10000$, $N' = 500$. The short time fitting result is $k = 0.1992$, $b = -0.8132$. The long time fitting result is $k = -0.1396$, $b = 0.0867$.

Chapter 5

Noisy Quantum Gate

5.1 Driving Error

In reality, the Rabi driving on a qubit is always non-resonant due to the fluctuation in local field strength produced by dipolar couplings. Such a fluctuation β will lead to inevitable errors in the Rabi driving, disturbing both the driving axis and accumulated phase. Studying the error distributions and their properties will provide an insight into error mitigation and benefit the quantum information processing at a fundamental level.

The evolution unitary of a qubit under non-resonant driving is shown in Eqn. 4.6. If we take positions and configurations of bath spins (disorder realization) into consideration, then the effective unitary will be labeled by ζ ,¹

$$U(t, \zeta) = \cos\left(\frac{\Omega_\zeta t}{2}\right) + i \sin\left(\frac{\Omega_\zeta t}{2}\right) \sigma_n(\zeta) \quad (5.1)$$

in which

$$\Omega_\zeta = \sqrt{h^2 + \beta_\zeta^2}, \quad \sigma_n(\zeta) = \vec{\sigma} \cdot \left(\frac{h}{\Omega_\zeta}, 0, \frac{\beta_\zeta}{\Omega_\zeta}\right). \quad (5.2)$$

h is an effective driving strength given by $\gamma_0 B$, Ω_ζ is the local field inhomogeneity $\Delta\omega$, decided by the environmental couplings. They are both in the dimension of frequency.

For an arbitrary driving axis \vec{n}_0 with constant pulse strength h . The Rabi frequency and driving axis can be given by

$$\Omega_\zeta = \|\beta_\zeta \vec{n}_\zeta + h \vec{n}_0\|, \quad \vec{n}_\zeta = (\beta_\zeta \vec{n}_\zeta + h \vec{n}_0) / \Omega_\zeta \quad (5.3)$$

5.1.1 Phase Error

In order to determine the optimal duration for a Pi pulse, we need to calibrate our system with Rabi signal. The spin is prepared at Z state and then rotated around X axis, and measured from Y basis. The signal is

$$\langle S_y(t) \rangle_\zeta = -n_x \langle \sin(\Omega_\zeta t) \rangle_\zeta \quad (5.4)$$

The optimal duration of Pi pulse, t_π , is defined by

$$f(t) = \langle \sin(\Omega_\zeta t_\pi) \rangle_\zeta = \frac{1}{N} \sum_{\zeta=1}^N \sin(\Omega_\zeta t_\pi) = 0, \quad (5.5)$$

It can be found at the zero point of $\langle S_y(t) \rangle$, as shown in Fig. 5.1. Taking the zero point of $S_y(t)$ is more efficient compared with finding the minimum of $S_z(t)$, since the error of slope detection is lower. But the phase accumulation on a specific disorder realization $\Omega_\zeta t_\pi$ is not

¹ ζ here is a combinational index for both disorder realization and spin configurations, detailed description about ζ is given in Appendix. A.

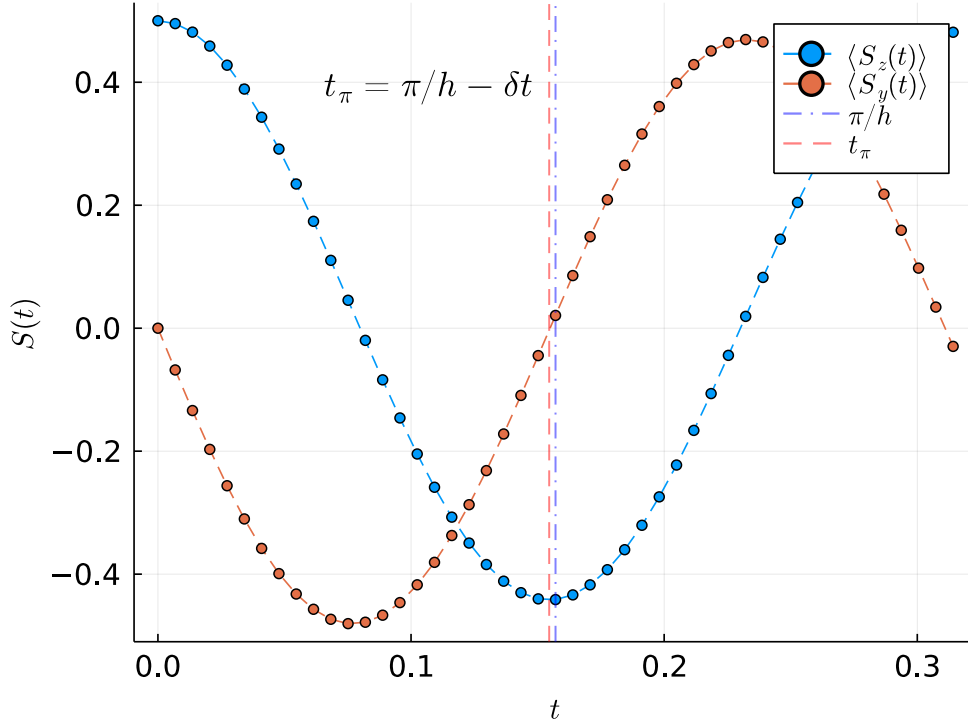


Figure 5.1: Corrected gate time for Pi pulse t_π in 3D ensemble at $h = 20$.

t_π can be found by fitting the linear line around π/h and calculating the zero root. The curve is sampled at $M' = 2000$ and $N' = 1000$.

necessarily π . Phase error ε is defined by

$$\langle \sin(\pi + \varepsilon_\zeta) \rangle_\zeta = 0 \Rightarrow \varepsilon_\zeta = \Omega_\zeta t_\pi - \pi. \quad (5.6)$$

The distribution of Ω_ζ can be obtained via a numerical sampling for β_ζ . Besides, t_π can be obtained by finding the first zero root of an ensemble-averaged Rabi oscillation. The distribution of phase error can be obtained numerically.

We found that the phase errors of Rabi driving are highly skewed with remarkable long tails², as shown in Fig. 5.2. This can be understood from the expression of Ω . Expand it

$$\Omega_\zeta = \sqrt{h^2 + \beta_\zeta^2} \approx h + \frac{\beta_\zeta^2}{2h} - \frac{\beta_\zeta^4}{8h^3} + \mathcal{O}(\beta/h)^6, \quad (5.7)$$

then we will immediately realize that the β_ζ^2 term lead to a positive fluctuation beyond the resonant Rabi frequency $\Omega_0 = h$. Substitute the formula into the phase error

$$\varepsilon_\zeta \approx \varepsilon_0 + \frac{\beta_\zeta^2}{2h} t_\pi, \quad \varepsilon_0 = h t_\pi - \pi. \quad (5.8)$$

We find that the error is peaked at $\varepsilon_0 = h t_\pi(h) - \pi$, and then gradually decays to a flat tail on the right side. This picture is clearly shown in Fig. 5.3. The location of the most probable

²In statistics, the skewness of a distribution is related with its third-order momentum, defined by

$$\tilde{\mu}_3[X] = \frac{\sum_i^N (X_i - \mu)^3}{(N-1)\sigma^3},$$

in which μ is the mean value and σ is the standard deviation. Skewness characterizes the asymmetry observed in a probability distribution.

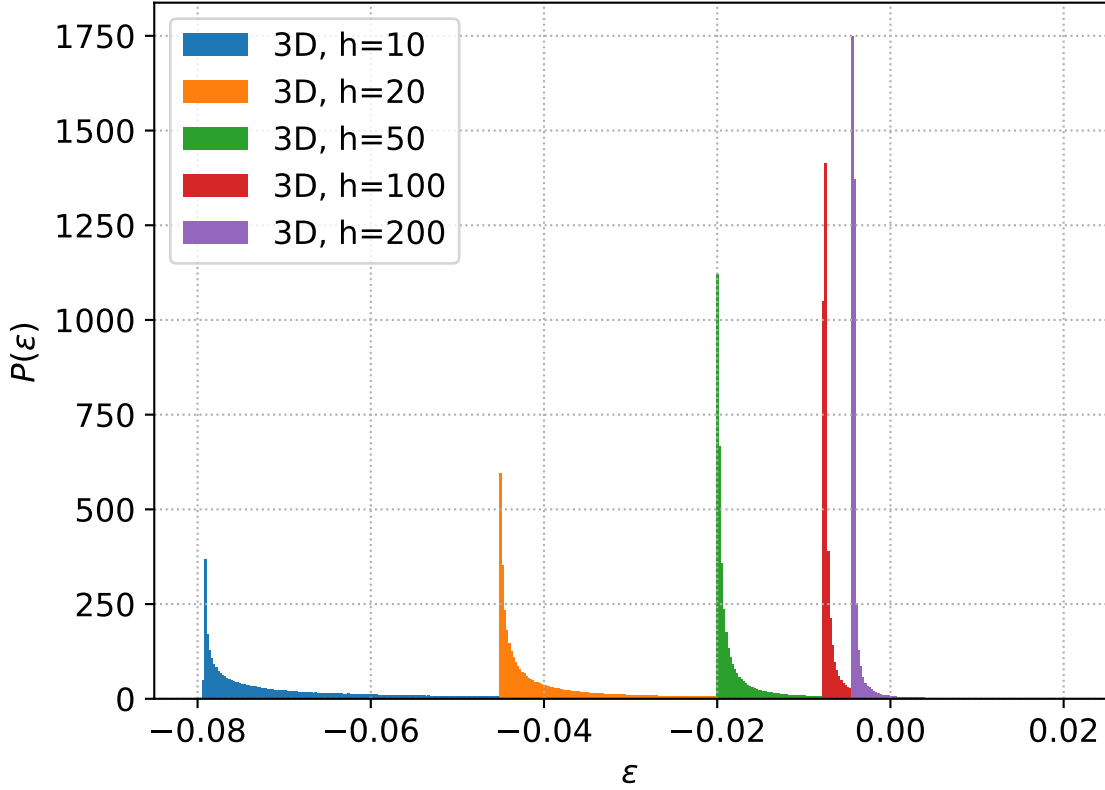


Figure 5.2: Distribution of phase error ε under various driving strength in 3D spin ensemble. The error is sampled with $M' = 2000$ disorder realizations (DR), and $N' = 400$ spin configurations for each DR. The histogram is plotted from -0.08 to 0.02 with 400 bins in total.

error ε_0 depends on the driving strength h . As h goes from 20 to 200, ε_0 is effectively reduced from 10^{-2} to 10^{-3} . **The long tail diverges to a significantly large scale because the second-order momentum of the Lorentzian distribution does not converge, as given in Eqn. 3.37** The statistical indicators of the distributions are demonstrated in Table. 5.4.

	h	mean	std	skewness	kurtosis	median
0	10.0	0.088264	0.509461	5.318630	33.110874	-0.064319
1	20.0	0.033233	0.360468	8.537711	84.078919	-0.041424
2	50.0	0.018340	0.251193	11.808517	163.677854	-0.019313
3	100.0	0.008155	0.158776	19.530045	473.378535	-0.007441
4	200.0	0.006242	0.148085	23.379660	637.224210	-0.004295

Table 5.4: Statistics of 3D phase error distribution

We find that both the standard deviation and fluctuation of mean value are shrunk with h going larger.

Yet, the growing kurtosis, which is at the scale of 10^2 , means that even if we will safely get a small error most of the time, significant error may still happen with a small probability. Such a property of long-tailed distribution is related to a famous phrase, "black swan", which means a rare event with a huge impact.

Another counterintuitive finding is that the medians of the error distributions are strictly 0. It means we have equal probabilities to get positive errors and negative errors, $P(\varepsilon > 0) =$

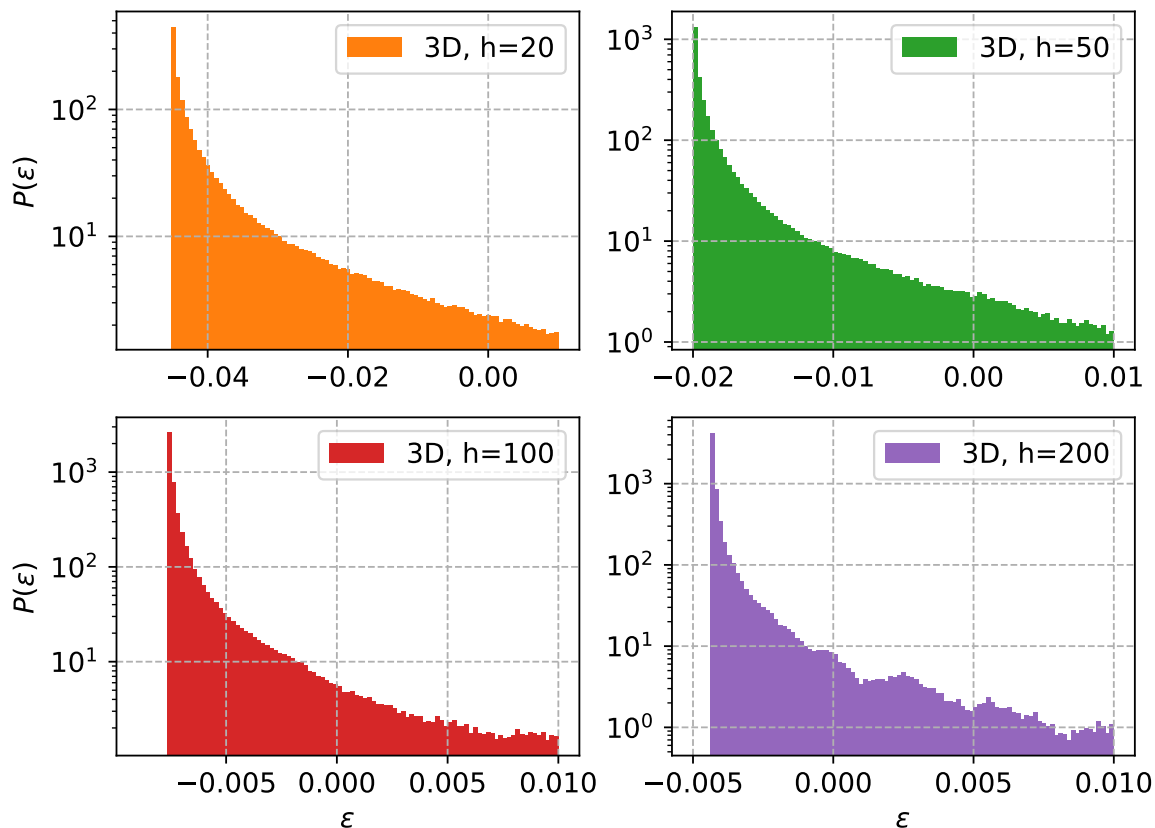


Figure 5.3: Log scale probability distribution function of ε in 3D ensemble under various driving strengths.

The range of the log scale histogram is adjusted with ε_0 , with 400 bins used in total. The distributions are similar to each other, only scaled on the horizontal axis.

$P(\varepsilon < 0) = 1/2$, so the distributions are still "balanced", while highly skewed. The difference is that the negative errors are confined in a limited range $\varepsilon \in [\varepsilon_0, 0)$, while the positive errors are stretched in a large area $\varepsilon \in (0, \infty]$ with thin probabilities.

Similar phenomena can be observed in 2D and 1D systems. The phase error distribution in 2D is attached in Appendix, Fig. C.8, and the 1D case is shown here in Fig. 5.5. Compared with the 3D case, the phase error of 2D and 1D is more centralized. The peaks are higher and thinner, corresponding to lower kurtosis. Detailed static indicators of the distributions are appended in table D.3 and 5.7. We found that the distributions of phase error in low dimensions are less tailed and skewed, yet have larger fluctuations. For example, the kurtosis at $h = 50$ is 163.68 for 3D, 72.96 for 2D, and 28.18 for 1D, such that $\text{Kurt}[\varepsilon_{3D}] > \text{Kurt}[\varepsilon_{2D}] > \text{Kurt}[\varepsilon_{1D}]$. However, their relation on standard deviation is reversed $\sigma_{3D} = 0.25 < \sigma_{2D} = 1.19 < \sigma_{1D} = 5.82$. The large variance in low dimensional systems make them hard to sample. As shown in Fig. 5.6, the fluctuations on the distribution can be clearly observed even if we increase the sampling size to $M' = 5000$ and $N' = 1000$.

5.1.2 Axis Error

The rotation axis of Rabi driving is given by

$$\vec{n}_\zeta = (n_{\zeta,x}, n_{\zeta,y}, n_{\zeta,z}) = \left(\frac{\hbar}{\Omega_\zeta}, 0, \frac{\beta_\zeta}{\Omega_\zeta} \right)$$

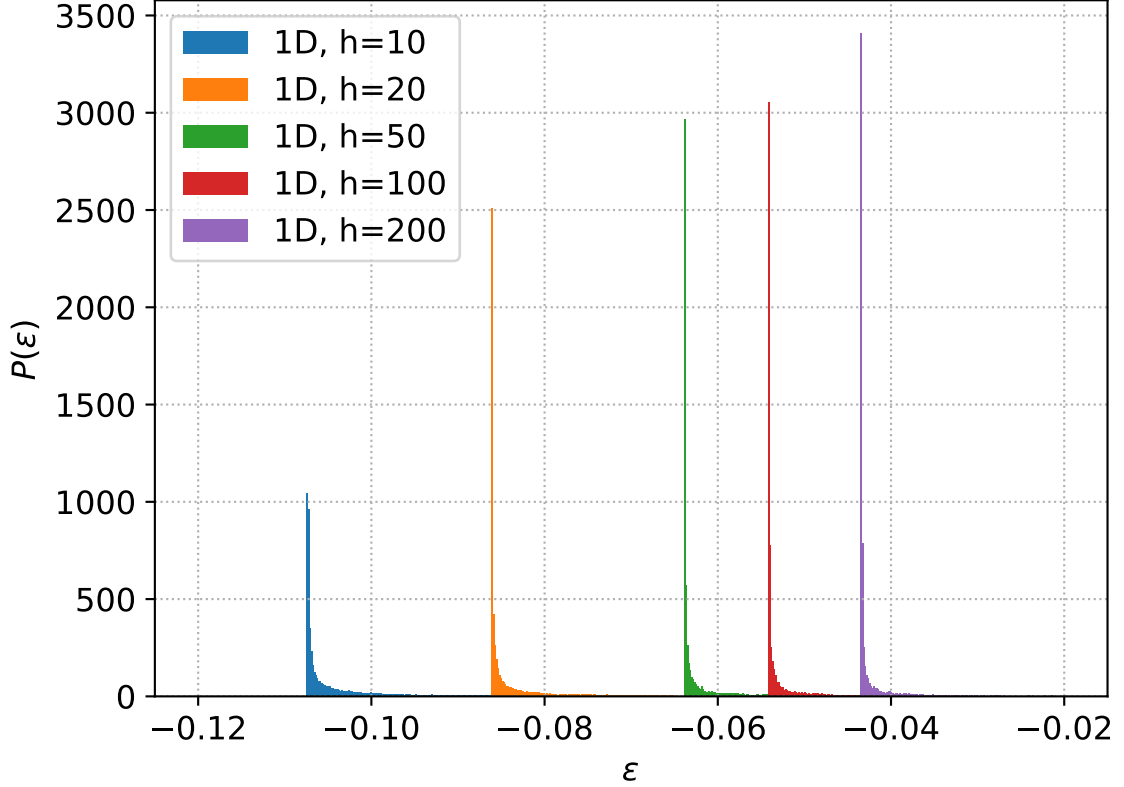


Figure 5.5: Distribution of phase error ε under various driving strength in 1D spin ensemble

The error is sampled with $M' = 5000$ disorder realizations(DR), and $N' = 1000$ spin configurations for each DR. the histogram is plotted from -0.12 to 0.02 with 600 bins in total.

	h	mean	std	skewness	kurtosis
0	10.0	2.745321	7.622191	3.612021	13.807976
1	20.0	1.944198	6.542662	4.462761	21.581191
2	50.0	1.552844	5.822662	5.050152	28.185031
3	100.0	1.257895	5.475406	5.613614	34.153929
4	200.0	0.982550	4.829757	6.612477	48.233012

Table 5.7: Statistics of 1D phase error

in which the driving field is applied along the X-direction. In an ideal limit, the Rabi driving is a perfect rotation around X-axis such that $\vec{n} = (1, 0, 0)$. So we expect that $\langle n_z(\zeta) \rangle_\zeta = 0$, $\langle n_x(\zeta) \rangle_\zeta = 1$. Yet, due to the local effective field produced by the bath spins, the driving axis will be shifted to a small angle. The error of the driving axis can be defined as

$$\delta n_{\zeta,z} = n_{\zeta,z}, \quad \delta n_{\zeta,x} = 1 - n_{\zeta,x}. \quad (5.9)$$

Since $\sqrt{n_{\zeta,x}^2 + n_{\zeta,z}^2} = 1$, we only need to study one of the error $\delta n_{\zeta,z}$. Expand the expression

$$\delta n_{\zeta,z} = \frac{\beta_\zeta}{\sqrt{\beta_\zeta^2 + h^2}} \approx \frac{\beta_\zeta}{h} - \frac{\beta_\zeta^3}{2h^3} + \mathcal{O}(\beta_\zeta/h)^5. \quad (5.10)$$

On the contrary to phase error, the axis error is related with the odd terms of β_ζ in the expansion. If we truncate the high order terms, then the distribution of $n_{\zeta,z}$ is just a rescaled distribution of the original β_ζ , as shown in Fig. 5.8, 5.9, 5.10. Statistical indicators of the dis-

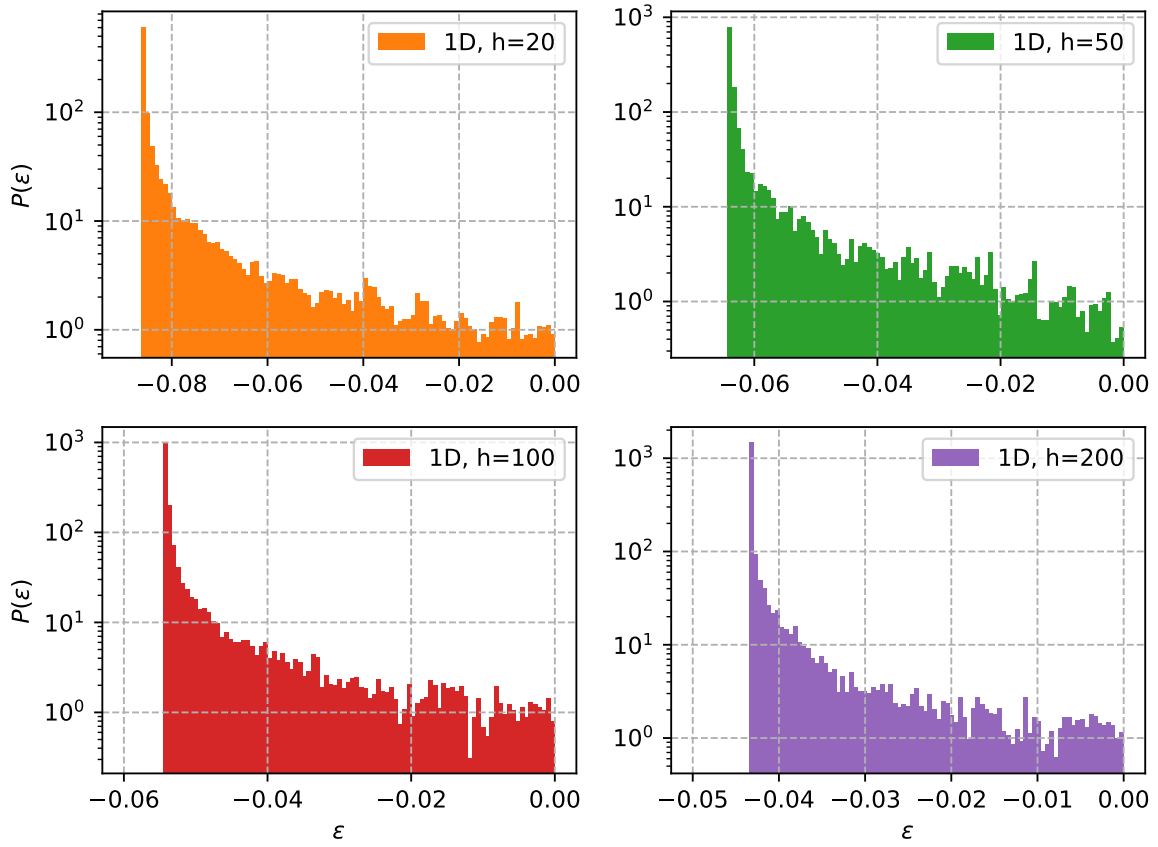


Figure 5.6: Log scale probability distribution function of ε in 1D ensemble under various driving strengths.

tributions are given in Appendix. D. The standard deviation is shrunk by approximately $1/h$ as expected while the kurtosis is increased with growing h .

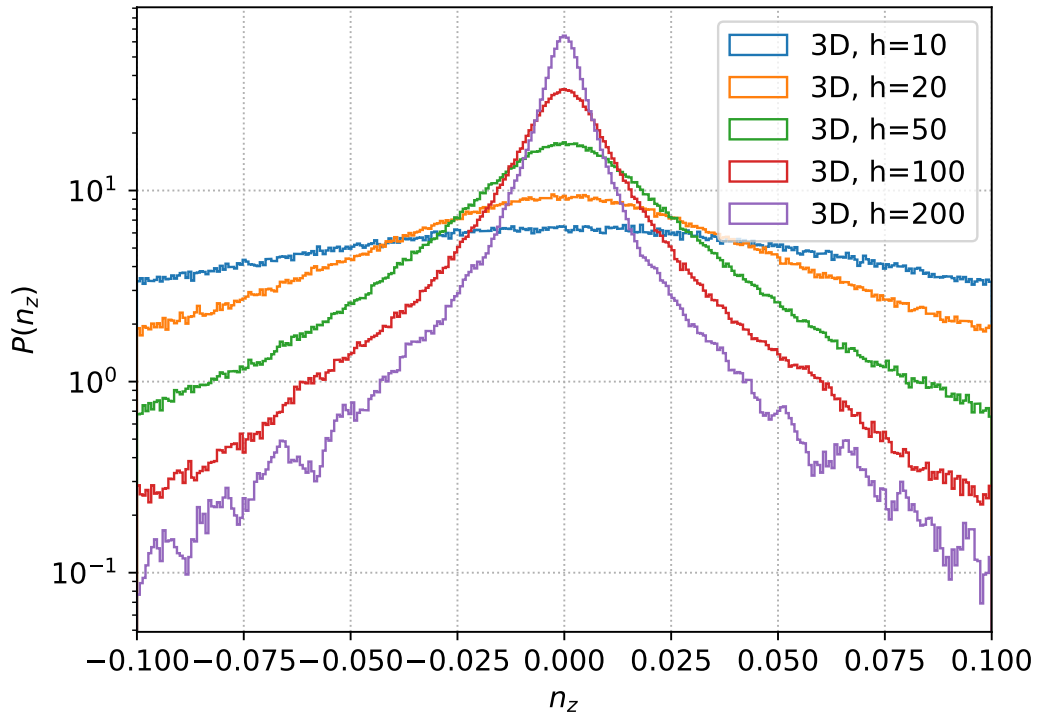


Figure 5.8: Distribution of axis error in 3D ensemble under various driving strengths.

The error is sampled with $M' = 2000$ disorder realizations(DR), and $N' = 400$ spin configurations for each DR. The histogram is plotted from -0.1 to 0.1 with 300 bins in total. The fluctuations of sampling increase with the driving strength h .

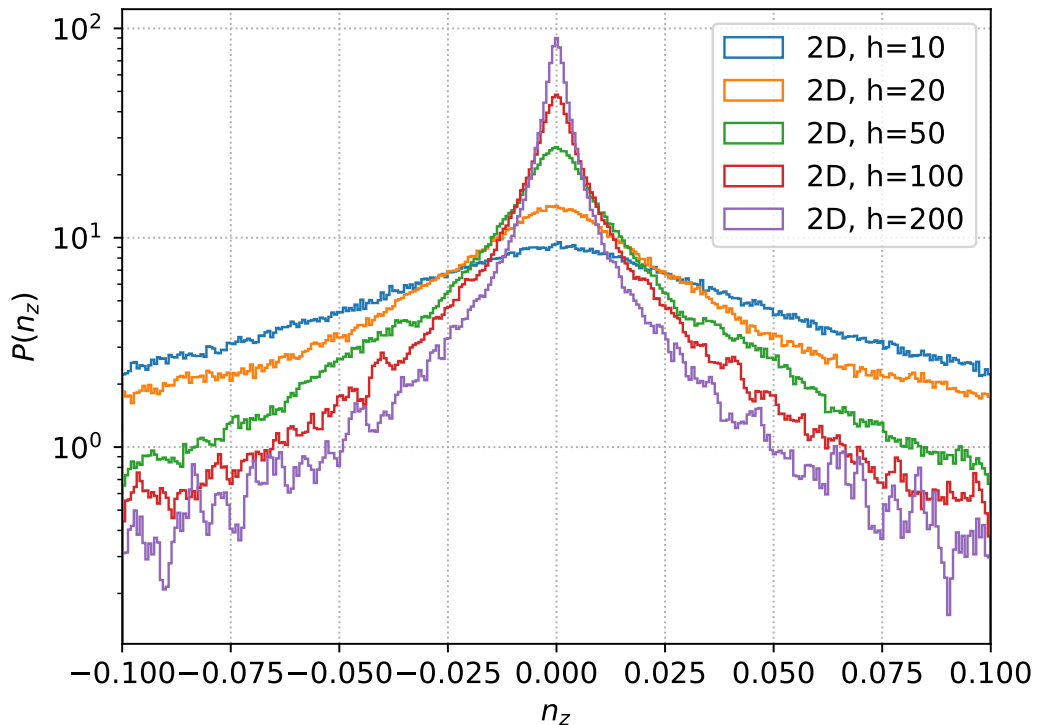


Figure 5.9: Distribution of axis error in 2D ensemble under various driving strengths.

The error is sampled with $M' = 2000$ disorder realizations(DR), and $N' = 400$ spin configurations for each DR. The histogram is plotted from -0.1 to 0.1 with 300 bins in total.

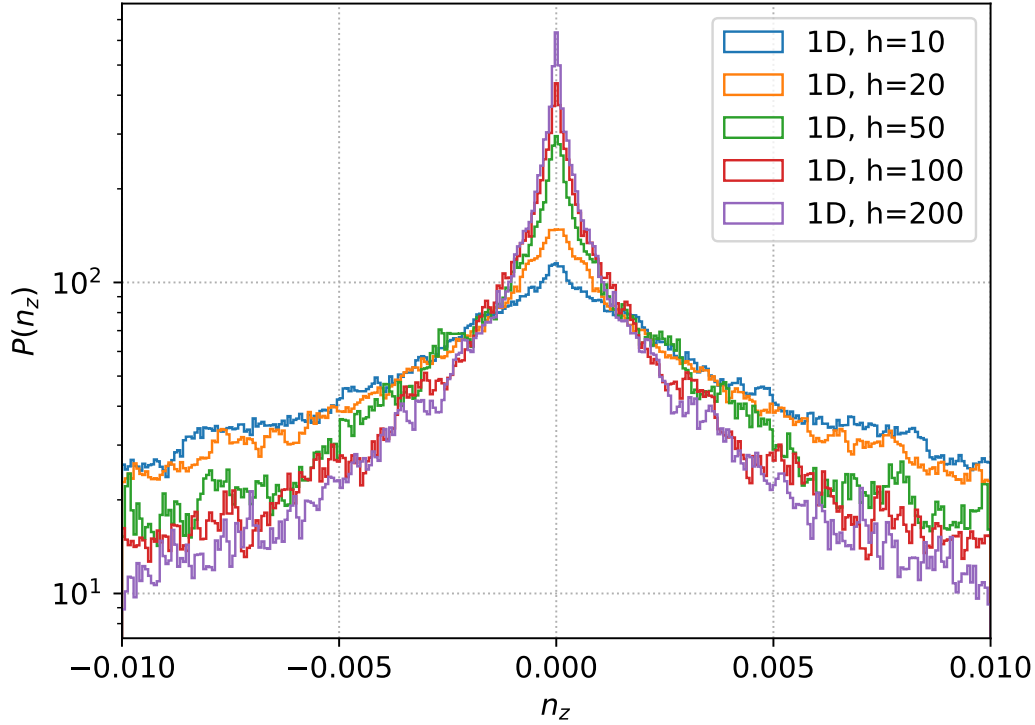


Figure 5.10: Distribution of axis error in 1D ensemble under various driving strengths.

The error is sampled with $M' = 5000$, and $N' = 1000$. Significant fluctuations can be observed in the sampling even though the sampling size is larger. The histogram is plotted from -0.1 to 0.1 with 300 bins in total.

5.2 Combined Error Distribution

In reality, Rabi driving of spin qubits is simultaneously affected by both the phase error and axis error. The combinational error distribution can be visualized in the following 2D heat maps, as demonstrated in Fig. 5.11, Fig. 5.12, and Fig. 5.13.

A quadratic curve can be clearly observed in the heat maps, which is given by

$$\varepsilon_\zeta - \varepsilon_0 = \frac{ht_\pi}{2} n_{\zeta,z}^2, \quad h \gg \beta_\zeta. \quad (5.11)$$

It can be obtained by expanding ε_ζ , $n_{\zeta,z}$ and preserving 2 order terms. As h increased from 20 to 200, the range of axis error is reduced from 10^{-1} to 10^{-2} while the phase error is reduced from 10^{-2} to 10^{-3} in 3D ensembles. This is good news for experimentalists, as we can always improve the driving fidelity of qubit by applying a stronger driving field.

However, due to the skewness of phase distribution, the combined errors are largely centralized around the bottom of the quadratic curve, which corresponds to the bright yellow areas on the heat map. From 3D to 1D, the probability density is more and more concentrated, as the distribution of β becomes sharper. In 1D, the error density is almost squeezed to a small spot on the vertex of the quadratic curve, as shown in Fig. 5.13.

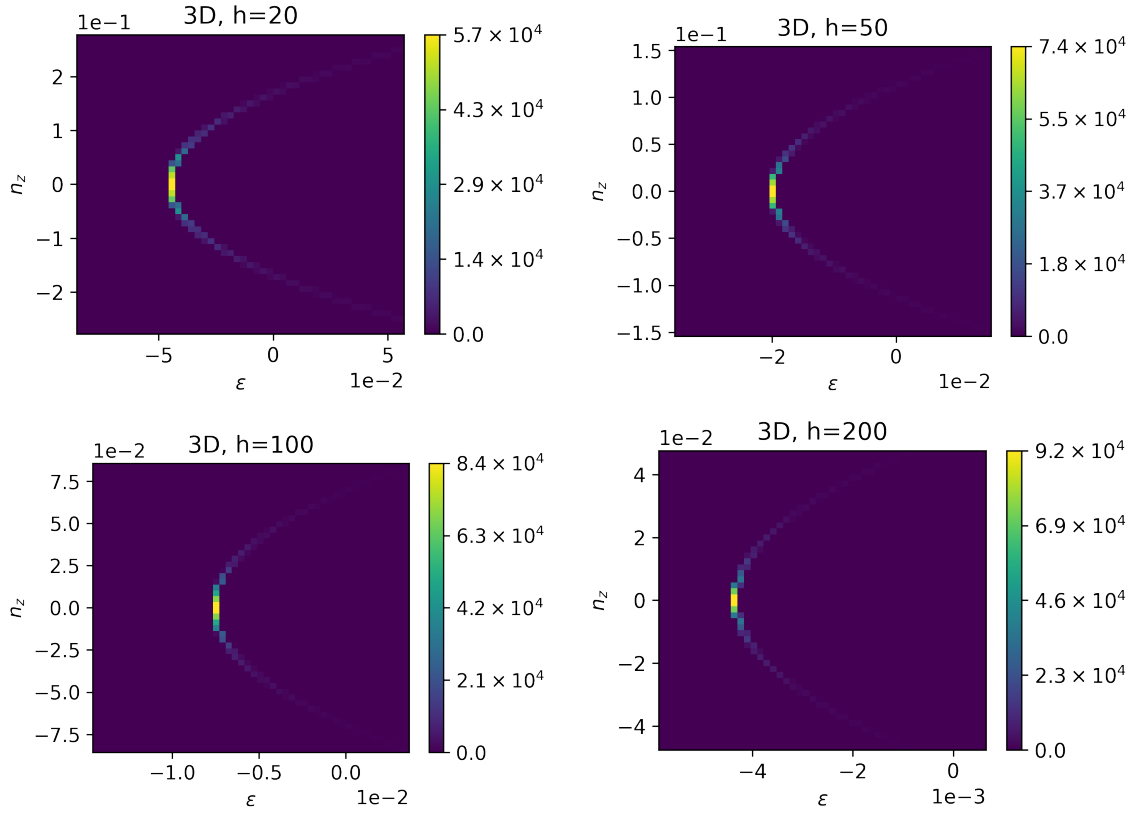


Figure 5.11: Distribution of driving error in 3D ensembles

The resolution of the heat maps is 50×50 , with bin area $dA = \Delta\epsilon\Delta n_z$ depending on the plotting range of phase and axis error. A quadratic structure can be observed in the combined error distribution.

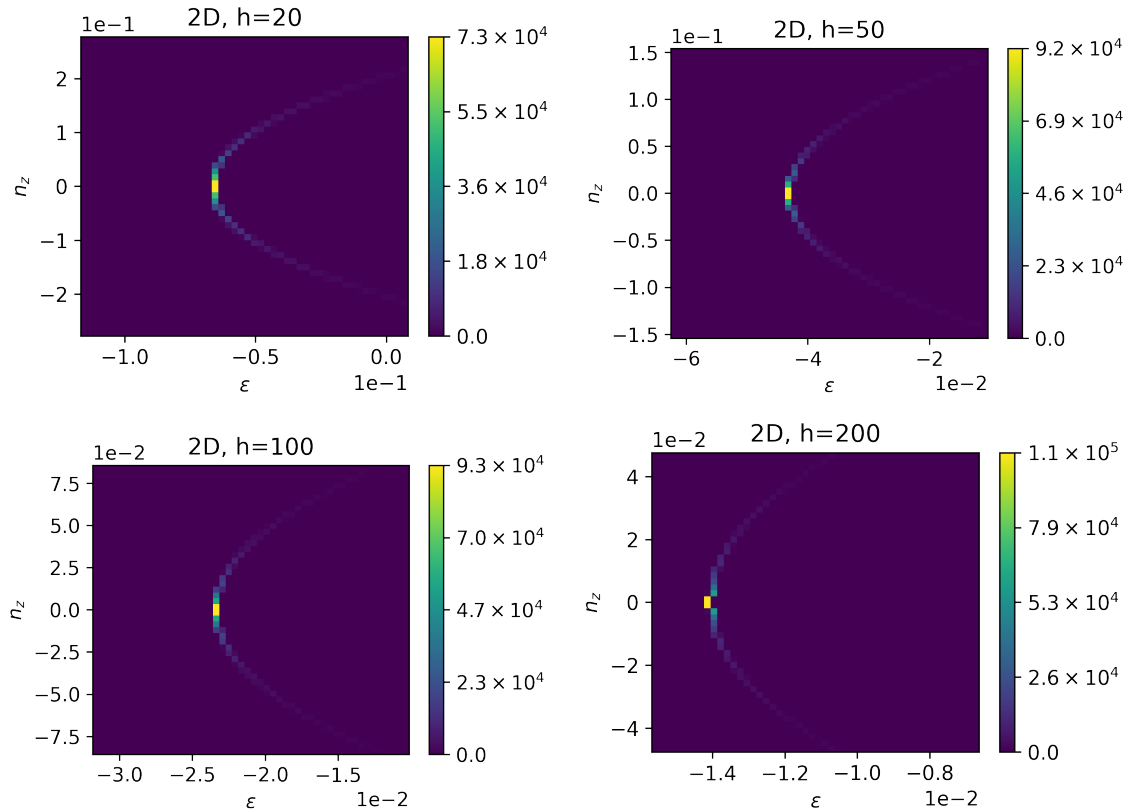


Figure 5.12: Distribution of driving error in 2D ensembles

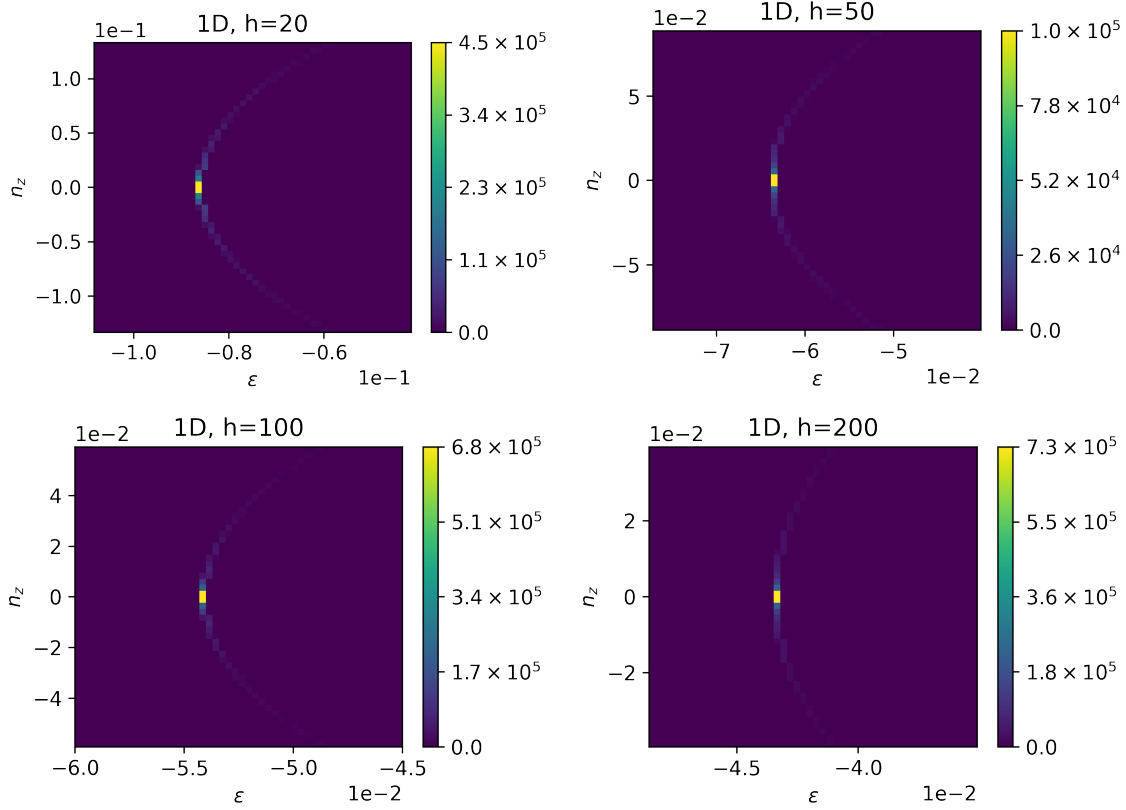


Figure 5.13: Distribution of driving error in 1D ensembles

5.3 Fidelity of Quantum Gate

Quantum gates are the central concept in the circuit-based quantum computation model. A quantum gate defines a certain unitary operation on qubits, such as X or CNOT which is analogous to classical logic gates in digital electronics. For spin qubits, single qubit quantum gates are just Rabi driving with a set of fixed parameters implemented using the RF driving field. For example, in ideal resonant driving, X gate can be implemented by setting the driving field along the axis, $\phi = 0$, and keeping the driving time for $t = \pi/(\gamma_0 B)$, as shown in Eqn. 4.4.

However, as we have seen in previous discussions, errors from the environmental coupling are inevitable in the driving process. As a consequence, what we get in reality is actually a noisy quantum operation, instead of an unitary gate. In order to estimate the effect of environmental noise and know how well we can control and manipulate qubits, fidelity metrics are needed.

5.3.1 Pulse Gate as a Quantum Operation

Consider a spin qubit an interacting spin bath, where the qubit is labeled by "0" and the bath is label labeled by "b". For the central spin qubit, evolution of its density matrix is given by

$$\rho_0(t) = \text{Tr}_b U(\rho_0 \otimes \rho_b) U^\dagger = \sum_k \langle k|U(\rho_0 \otimes \rho_b)U^\dagger|k\rangle = \sum_k c_k \langle k|U|k\rangle \rho_0 \langle k|U^\dagger|k\rangle \quad (5.12)$$

in which $|k\rangle$ denotes a eigen state of the bath spins, $c_b(k) = \langle k|\rho_b(0)|k\rangle$ is the probability of $|k\rangle$ state. The effective unitary is already given in previous chapter as

$$\langle k|U|k\rangle = e^{-i\langle k|\mathcal{H}|k\rangle t} = \langle k|e^{-i\mathcal{H}t}|k\rangle = \cos\left(\frac{\Omega_k t}{2}\right) - i \sin\left(\frac{\Omega_k t}{2}\right) (\vec{n}_k \cdot \vec{\sigma}). \quad (5.13)$$

If we define the operator $E_k = \sqrt{c_k} \langle k|U|k\rangle = \sqrt{c_k} U_k$, then the density matrix can be written in the Kraus operator form of quantum operation

$$\rho_0(t) = \sum_k \langle k|U|k\rangle \rho_0 \langle k|U^\dagger|k\rangle = \mathcal{E}[\rho_0(0)] = \sum_{k=0}^{2^n-1} E_k \rho_0 E_k^\dagger. \quad (5.14)$$

Hence the time evolution of the the density matrix is not a unitary but a non-unitary *quantum operation*, denoted by \mathcal{E} . We can easily check its property as a TPCP (trace preserving completely positive) map

$$\sum_k E_k E_k^\dagger = \sum_k c_k U_k U_k^\dagger = 1. \quad (5.15)$$

5.3.2 Entanglement Fidelity

A good metric to measure the distance between the quantum operation and the desired unitary is the *average gate fidelity*, which is the average fidelity over all possible input states. For convenience in the calculation, it can be derived from the entanglement fidelity.

The entanglement fidelity of the quantum channel can be write as

$$F_{\text{ent}}(U, \mathcal{E}) = \langle \Psi | (I \otimes \mathcal{T})(|\Psi\rangle\langle\Psi|) | \Psi \rangle \quad (5.16)$$

in which the $\mathcal{T}(\rho) = U^\dagger \mathcal{E}(\rho) U$ is a converted quantum channel, $|\Psi\rangle\langle\Psi|$ is the maximal entanglement state for dimension d .

$$|\Psi\rangle = \frac{1}{\sqrt{d}} \sum_{k=0}^{d-1} |k, k\rangle, \quad (5.17)$$

Since the quantum channel \mathcal{E} is a single-qubit process ($d = 2$), the maximal entanglement state is just Bell state $|\Psi\rangle\langle\Psi| = \frac{1}{\sqrt{2}}(|00\rangle + |11\rangle)$. The Eqn. 5.16 can be further derived into the form

$$F_{\text{ent}} = \langle \Psi | (I \otimes \mathcal{T})(|\Psi\rangle\langle\Psi|) | \Psi \rangle = \langle \Psi | (I \otimes U^\dagger)(I \otimes \mathcal{E})(|\Psi\rangle\langle\Psi|)(I \otimes U) | \Psi \rangle \quad (5.18)$$

$$= \sum_{k=0}^{2^n-1} c_k \langle \Psi | (I \otimes U^\dagger U_k) | \Psi \rangle \langle \Psi | (I \otimes U_k^\dagger U) | \Psi \rangle \quad (5.19)$$

Using the expression above we can derive the entanglement fidelity of all common used single qubit gate. It can be prove that, if U is a Pauli matrix P_j then its fidelity is

$$\langle \Psi | (I \otimes P_j^\dagger U_k) | \Psi \rangle \langle \Psi | (I \otimes U_k^\dagger P_j) | \Psi \rangle = (\vec{n}_k \cdot \vec{e}_j)^2 \sin^2 \left(\frac{\Omega_k t}{2} \right), \quad P_j = X, Y, Z; \quad j = 1, 2, 3 \quad (5.20)$$

Thus the entanglement fidelity of Pauli gates (X,Y,Z) can be given by

$$F_{\text{ent}}(P_j, \mathcal{E}) = \sum_{k=0}^{2^n-1} c_k (\vec{n}_k \cdot \vec{e}_j)^2 \sin^2 \left(\frac{\Omega_k t}{2} \right). \quad (5.21)$$

With the same approach we can give that for Pi/2 pulse gates ($\sqrt{X}, \sqrt{Y}, \sqrt{Z}(S)$)

$$F_{\text{ent}}(\sqrt{P_j}, \mathcal{E}) = \frac{1}{2} \sum_{k=0}^{2^n-1} c_k \left[\cos \left(\frac{\Omega_k t}{2} \right) - (\vec{n}_k \cdot \vec{e}_j) \sin \left(\frac{\Omega_k t}{2} \right) \right]^2 \quad (5.22)$$

For Hadamard gate

$$F_{\text{ent}}(H, \mathcal{E}) = \frac{1}{4} \sum_{k=0}^{2^n-1} c_k (n_{kx} + n_{kz})^2 (1 - \cos(\Omega_k t)) \quad (5.23)$$

There is a relation between entanglement fidelity and average gate fidelity

$$F_{\text{avg}} = \frac{dF_{\text{ent}} + 1}{d + 1} \quad (5.24)$$

in which d is the dimension of the system, which is $d = 2$ for single qubit. Using this formula we can easily derive the overall average gate fidelity. The average gate fidelity can also be obtained by finding the state average fidelity over all possible input states. This approach will give the same result as shown in Appendix. B.15.

5.3.3 Numerical Results

Given all the results above, the fidelity of single qubit gates can be well evaluated by Monte-Carlo Method. Here the infidelities $1 - F(U, \mathcal{E})$ of X, Y, Z gates are displayed in Fig. 5.14. Similar plot for $\text{Pi}/2$ gates ($\sqrt{X}, \sqrt{Y}, \sqrt{Z}(S)$) is shown in Appendix. C.13

We find that the infidelities of pulse gates decrease quasi-linearly in the log scale, following the relation $\ln(1 - F_{\text{avg}}) = m h + b$. The fitting result is listed in Table. D.5.

Increasing the driving strength h can effectively reduce the infidelities of quantum gates. For X, Y gates in 3D, $m \approx -0.011$ with $b \approx -3.6$. Such a result means that the 1% infidelity threshold for error correction can be achieved at $h \approx 77$ for a 3D ensemble. Higher precision can be achieved by further increasing the driving strength. 0.1% will be achieved at $h \approx 270$.

Yet, the suppression of error is more difficult in low dimensions. The initial infidelity at $h = 20$ is even larger than 10% for 1D case, which is completely unacceptable for information processing. The fitting result is $m \approx -0.007$ with $b \approx -2.6$ for 2D and $m \approx -0.011$ with $b \approx 0.4$ for 1D. If this prediction can be extrapolated to the stronger driving regime, then that means we need $h \approx 250$ to achieve 1% infidelity for 2D spin ensemble, and $h \approx 600$ in 1D, which would be a challenge in experiments.

In brief, the fidelity of single quantum gates in low dimensions is significantly limited due to the large fluctuation in local field induced by the environmental couplings.

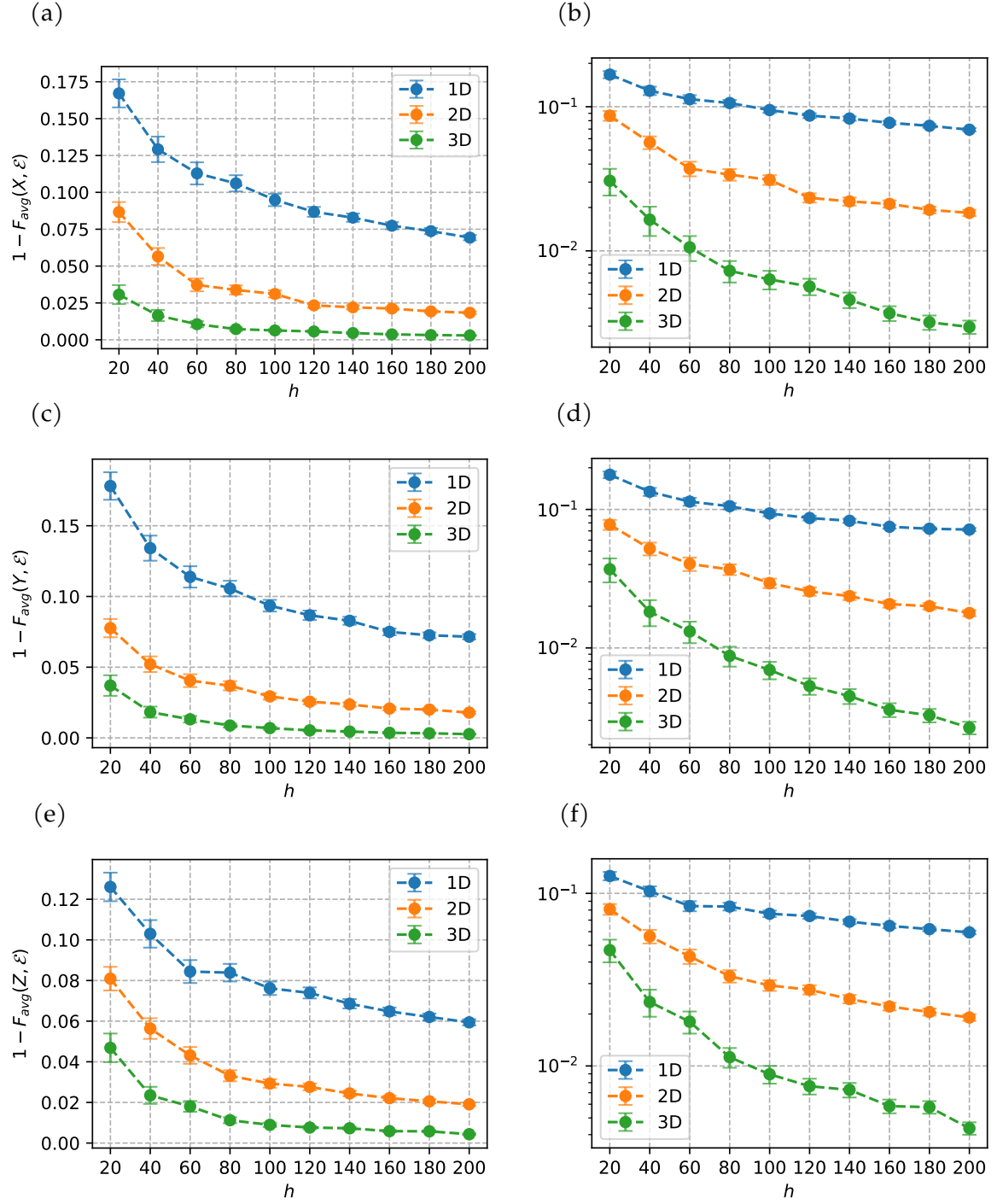


Figure 5.14: Average Gate Fidelity of Single Qubit Gates

(a): X gate infidelity, in normal scale. (b): Y gate infidelity, in log scale. (c): Y gate infidelity, in normal scale. (d): X gate infidelity, in log scale. (e): Z gate infidelity, in normal scale. (f): Z gate infidelity, in log scale. The results is obtained from Monte-Carlo sampling with $M' = h^2$, $N' = 1000$. Two fold of the mean error is displayed to make the errorbar visible.

Chapter 6

Decoupling Protocols

6.1 Periodic Driving System

6.1.1 Periodic pulse driving

As has been demonstrated by Hahn and Purcell, a properly designed sequence of pulses can effectively mitigate decoherence. By adding Floquet terms to the system Hamiltonian, periodic pulse sequence can remove the environmental couplings from the time average of Hamiltonian[27][49]. The coherence time of the system can be equivalently extended in the sense of synchronized measurements. This approach is known as dynamical decoupling since the system seems to be decoupled from its environment. The sequence of pulses used for dynamical decoupling constitutes a quantum control protocol.

An essential question is that in what extent can we eliminate the environmental coupling for the artificial quantum system? This question is partially answered by the theoretical work of Seth Lloyd[48], in which he proved that given an arbitrary form of interaction Hamiltonian, the environmental coupling can be fully eliminated by a periodic control protocol at the limit of infinite-short pulse operation.

However, an infinite short pulse, or equivalently infinite strong pulse strength, is impossible in reality. For spin qubits, the driving strength is limited by the maximal RF magnetic field we can produce. In recent experiments, the pulse time for a Pi gate is at the scale of $10^{-7} \sim 10^{-8}$ s, which is about 10 ns \sim 100 ns[59][14]. The finite duration of pulse time plays an important role in the performance of dynamical decoupling protocols [20] [28].

Consider a spin qubit interacting with bath spins, and driven by an RF field, its Hamiltonian can be written as

$$\mathcal{H}(t) = \mathcal{H}_0 + \mathcal{H}_C(t), \quad \mathcal{H}_C = -\hbar\omega_p[\cos\phi I_x + \sin\phi I_y] = -\hbar\omega_p(\vec{n} \cdot \vec{I}) \quad (6.1)$$

in which \mathcal{H}_0 is the internal Hamiltonian of the system and \mathcal{H}_C is the term from driving pulse.

Denote the pulse duration as t_p , then the evolution of the system can be written as

$$P_\phi(t_p) = \exp\left[-\frac{i}{\hbar}(\mathcal{H}_0 + \mathcal{H}_C)t_p\right] \quad (6.2)$$

If the pulse strength is much stronger than the internal interactions, which means $\|\mathcal{H}_C\| \gg \|\mathcal{H}_0\|$. Then the pulse unitary applied to the system, as shown in Eqn.6.2, can be regarded as a perfect rotation gate with angle θ .

$$P_\phi(\theta) \approx \exp\left(-\frac{i}{\hbar}\mathcal{H}_C t_p\right) = \exp\left[\frac{i}{\hbar}(\vec{n} \cdot \vec{I})\theta\right], \quad \theta \equiv \omega_p t_p \quad (6.3)$$

$\vec{n} \cdot \vec{I} = \cos(\phi)I_x + \sin(\phi)I_y$. ω_p is the strength of driving field. We expect that $t_p \approx 0$ for very strong driving. The default evolution of the system can be written as

$$U(t) = \exp\left(-\frac{i}{\hbar}\mathcal{H}_0 t\right) \quad (6.4)$$

since the Zeeman and dipolar terms are commutative. For a periodic pulse sequence with n repetitions, the evolution of system can be depicted as

$$\rho(t) = \rho(n t_c) = \{U(\tau)P_\phi U(\tau)\}^n \rho(0) \left\{U^\dagger(\tau)P_\phi^\dagger U^\dagger(\tau)\right\}^n \quad (6.5)$$

in which t_c is the period of the driving, $t_c = 2\tau + t_p$.

6.1.2 Average Hamiltonian Theory

In the following derivations we drop the constant by assuming that $\hbar = 1$.

For a time dependent Hamiltonian $\mathcal{H}(t)$, its time evolution is a unitary can be given by

$$U(t) = \exp\left(-\frac{i}{\hbar} \int_0^t \mathcal{H}(\tau) d\tau\right) \quad (6.6)$$

The unitary can be rewrite into a time evolution of static Hamiltonian.

$$U(t) \mapsto U(t_c) = \exp(-i\bar{\mathcal{H}}t_c) \quad (6.7)$$

under the conditions

1. The Hamiltonian $\mathcal{H}(t)$ is periodic for t_c .
2. The measurement is synchronized with the periods.

In a discrete approximation we can split $\mathcal{H}(t)$ into a set of static Hamiltonians in a set of small time intervals.

$$\mathcal{H}(t) = \mathcal{H}_k, \sum_0^{k-1} \tau_i < t < \sum_0^k \tau_i \quad (6.8)$$

such that

$$U(t) = \exp(-i\mathcal{H}_n \tau_n) \exp(-i\mathcal{H}_{n-1} \tau_{n-1}) \dots \exp(-i\mathcal{H}_2 \tau_2) \exp(-i\mathcal{H}_1 \tau_1) \quad (6.9)$$

Then the effective static Hamiltonian $\bar{\mathcal{H}}$ can be given by the Baker-Campbell formula

$$e^B e^A = \exp\left\{A + B + \frac{1}{2}[B, A] + \frac{1}{12}([B, [B, A]] + [[B, A], A]) + \dots\right\} \quad (6.10)$$

Use this formula the evolution operator can be reduced to

$$U(t) = \exp\left\{-i \sum_k^n \mathcal{H}_k \tau_k + \frac{1}{2} \sum_{j=1}^n \sum_{k=0}^{j-1} [-i\mathcal{H}_j \tau_j, -i\mathcal{H}_k \tau_k] + \dots\right\} \quad (6.11)$$

Compare with the Eqn. 6.7, we can get that

$$\bar{\mathcal{H}} = \bar{\mathcal{H}}^{(0)} + \bar{\mathcal{H}}^{(1)} + \bar{\mathcal{H}}^{(2)} + \dots \quad (6.12)$$

in which

$$\bar{\mathcal{H}}^{(0)} = \frac{1}{t_c} \sum_k^n \mathcal{H}_k \tau_k, \quad \bar{\mathcal{H}}^{(1)} = \frac{-i}{2t_c} \sum_{j=1}^n \sum_{k=0}^{j-1} [\mathcal{H}_j \tau_j, \mathcal{H}_k \tau_k] \quad (6.13)$$

The above expansion of static Hamiltonian, which Eqn. 6.12 is called Magnus expansion.

Usually, when the time step $\tau_k \ll 1$ is very small, the higher-order terms in the expansion are negligible to $O(\tau_k^2)$. The only remained term is the zero-order term, which is what we called average Hamiltonian.

6.2 Dynamical Decoupling Sequence

6.2.1 Toggling frames transformation

Now suppose we have a system with Hamiltonian \mathcal{H}_0 . A dynamical decoupling protocol is applied to the system, which can be described by a set of pulses P_k , separated by time intervals τ_k . They should satisfy the condition

$$P_n P_{n-1} \dots P_2 P_1 = I \quad (6.14)$$

The pulses are assumed to be perfect, meaning that their pulse duration is infinite short. The Hamiltonian is untouched during the pulse intervals. Then we can write the system evolution

$$U(t_c) = \exp(-i\mathcal{H}_0\tau_n)P_n \exp(-i\mathcal{H}_0\tau_{n-1}) \dots P_3 \exp(-i\mathcal{H}_0\tau_2)P_2 \exp(-i\mathcal{H}_0\tau_1)P_1 \exp(-i\mathcal{H}_0\tau_0) \quad (6.15)$$

The equation can be transformed to another form by inserting $P_1 P_1^\dagger = I$ between τ_1, τ_2 , $P_2 P_1 P_1^\dagger P_2^\dagger = I$ between τ_2, τ_3 , etc

$$\begin{aligned} U(t_c) &= \exp(-i\mathcal{H}_0\tau_n)P_n \exp(-i\mathcal{H}_0\tau_{n-1}) \dots P_3 \exp(-i\mathcal{H}_0\tau_2)P_2 P_1 P_1^\dagger \exp(-i\mathcal{H}_0\tau_1)P_1 \exp(-i\mathcal{H}_0\tau_0) \\ &= P_n P_n^\dagger \exp(-i\mathcal{H}_0\tau_n)P_n \dots P_3 \exp(-i\mathcal{H}_0\tau_2)P_2 P_1 U_1 U_0 \\ &= P_n P_n^\dagger \exp(-i\mathcal{H}_0\tau_n)P_n \dots P_3 P_2 P_1 P_1^\dagger P_2^\dagger \exp(-i\mathcal{H}_0\tau_2)P_2 P_1 U_1 U_0 \\ &= P_n P_n^\dagger \exp(-i\mathcal{H}_0\tau_n)P_n \dots P_3 P_2 P_1 U_2 U_1 U_0 \\ &= U_n U_{n-1} \dots U_2 U_1 U_0 \end{aligned} \quad (6.16)$$

in which we replaced that

$$\begin{aligned} U_0 &= \exp(-i\mathcal{H}_0\tau_0), \\ U_1 &= P_1^\dagger \exp(-i\mathcal{H}_0\tau_1)P_1 \\ U_2 &= P_1^\dagger P_2^\dagger \exp(-i\mathcal{H}_0\tau_2)P_2 P_1 \\ U_k &= P_1^\dagger P_2^\dagger \dots P_k^\dagger \exp(-i\mathcal{H}_0\tau_k)P_k \dots P_2 P_1 \end{aligned}$$

the notation can be written as

$$U_k = W_k^\dagger \exp(-i\mathcal{H}_0\tau_k)W_k, \quad W_k = P_k \dots P_2 P_1 \quad (6.17)$$

Then we can prove that for any matrix A, V the following relation is true.

$$V \exp(A)V^{-1} = \exp(VAV^{-1}) \quad (6.18)$$

Use this equation we can rewrite the Eqn.6.17 as

$$U_k = W_k^\dagger \exp(-i\mathcal{H}_0\tau_k)W_k = \exp(-iW_k^\dagger \mathcal{H}_0 W_k \tau_k) = \exp(-i\tilde{\mathcal{H}}_k t_k) \quad (6.19)$$

in which we define the *effective Hamiltonian in toggling frame*

$$\tilde{\mathcal{H}}_k = W_k^\dagger \mathcal{H}_0 W_k = P_1^\dagger P_2^\dagger \dots P_k^\dagger \mathcal{H}_0 P_k \dots P_2 P_1 \quad (6.20)$$

The name of toggling frame indicates that the Hamiltonian is rotated, flipped up and down by the controlling pulses.

Now use the formula of average Hamiltonian, Eqn. 6.13, we can write the first order average effective Hamiltonian of the system

$$\bar{\mathcal{H}}^{(0)} = \frac{1}{t_c} \sum_{k=0}^n W_k^\dagger \mathcal{H}_0 W_k t_k = \frac{1}{t_c} \sum_{k=0}^n \tilde{\mathcal{H}}_k t_k \quad (6.21)$$

It's exactly the time average of the Hamiltonian in the toggling frame.

6.2.2 Dynamical decoupling sequence

Dynamical decoupling is a technique of Hamiltonian engineering, that decouples a quantum system from its environment using dynamical control signals, in order to protect the quantum system, from decoherence caused by couplings with the environment.

As the average Hamiltonian theorem has shown, a dynamical decoupling protocol, which usually contains a periodic sequence of driving pulses $\{\tau - P_1 - 2\tau - P_2 - \dots - 2\tau - P_n - \tau\}$, can eliminate the zero-order time average of the coupling Hamiltonian.

$$\bar{\mathcal{H}}^{(0)} = 0, \quad \bar{\mathcal{H}}^{(1)} = \delta(\tau) \quad (6.22)$$

The higher-order terms of average Hamiltonian is a small quantity to the order of inter-pulse intervals, which can be ignored at a short period limit. Thus the time evolution of the system is approximately an identity matrix.

$$\bar{U}(t) = \exp(-i\bar{\mathcal{H}}t) \approx \mathbb{1} \quad (6.23)$$

By repeating the pulse sequence $\{\tau - P_1 - 2\tau - P_2 - \dots - 2\tau - P_n - \tau\}^n$, the system is freed to its original state in the sense of time average, $[\bar{U}(t)]^n \rho(0) \approx \rho(0)$, so that information can be stored in the quantum state without loss over time.

6.2.3 Spin dynamics during the coupling sequence

For a noisy Monte-Carlo simulation, we can use a piece-wise model to track the dynamics of qubit under the decoupling protocol. Consider a simple model of pulse $\{\tau - P - \tau\}$, for a specific noise β , its unitary can be given as a piece-wise function

$$\begin{cases} U(\beta, t) = U_0(\beta, t), & 0 < t < \tau \\ U(\beta, t) = P(\beta, t - \tau)U_0(\beta, \tau), & \tau < t < \tau + t_p \\ U(\beta, t) = U_0(\beta, t - \tau - t_p)P(\beta, t_p)U_0(\beta, \tau), & \tau + t_p < t < 2\tau + t_p \end{cases} \quad (6.24)$$

where P is the effective unitary of a pulse $P(t) = \exp(-i[\beta S_z + h(\vec{n} \cdot \vec{S})]t)$, where h is the driving strength and \vec{n} is the direction of the driving pulse P . And $U_0(\beta, \tau) = \exp(-i\beta\tau S_z)$ is the unitary during the free evolution.

With the above formulation, the dynamics of the spin during a pulse sequence can be treated as a quantum operation,

$$\rho(t) = \mathcal{E}(t)[\rho(0)] = \frac{1}{N} \sum_{\beta} U(\beta, t) \rho(0) U(\beta, t)^\dagger, \quad (6.25)$$

following the same norm shown in Chapter. 5. Such a model can be effectively evaluated by Monte-Carlo sampling on β , assuming that β obeys a distribution $P(\beta)$.

6.3 Carr-Purcell Typed Sequences

6.3.1 Protocol Review

Carr-Purcell typed sequences are the oldest and simplest dynamical decoupling protocol[11]. CP-like sequence only contains periodic π pulses, as shown in Fig. 6.1.

Here X_{-180} means a π pulse along the negative axis of X , in order to compensate for the phase error accumulated in the process. The sequence of CP protocol can be written

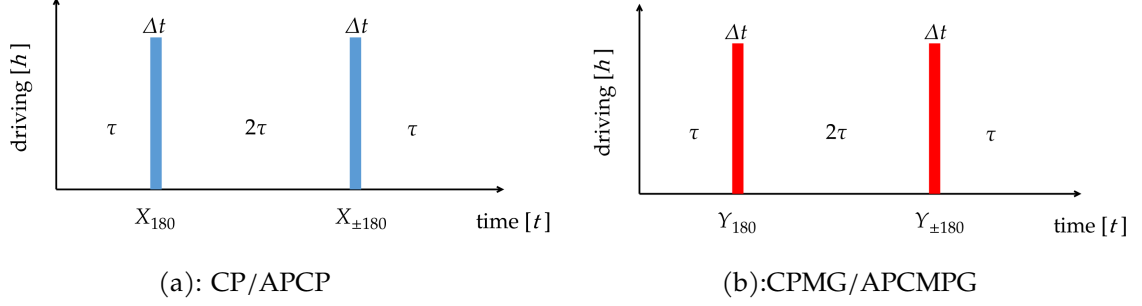


Figure 6.1: Diagram for one cycle of Carr-Purcell typed dynamical decoupling sequence.

as $\{\tau - 180_X - 2\tau - 180_X - \tau\}$, which is just a simple periodic Pi pulse. By flipping the second pulse, it becomes the APCP sequence (Alternating Phase Carr-Purcell), the sequence of which can be given as $\{\tau - 180_{\bar{X}} - 2\tau - 180_X - \tau\}$. The model contains two parameters, τ , the interval between pulses, and the driving strength h . When the pulse phase ϕ is determined, the duration of one pulse can be given by $t_p = \phi/h$. The pulse duration is usually ignored in an ideal model, as the analysis assumes h to be infinite.

Similarly, the sequence of CPMG/APCPMG protocol can be given by $\{\tau - 180_Y - 2\tau - 180_Y - \tau\}$, $\{\tau - 180_{\bar{Y}} - 2\tau - 180_Y - \tau\}$. CPMG (Carr-Purcell-Meiboom-Gill) and APCPMG sequence simply replace the X pulse with Y.

Given a perfect pulse with infinite short time and strong driving, CP/CPAP can fully eliminate the decoherence caused by Zeeman terms (noise related with S_z). The following proof will be trivial using toggling frame Hamiltonian picture.

$$\tilde{\mathcal{H}}_0 \sim S_z, \tilde{\mathcal{H}}_1 \sim X S_z X = -S_z, \tilde{\mathcal{H}}_2 \sim X X S_z X X = S_z$$

$$\bar{\mathcal{H}}^{(0)} \sim \tau S_z - 2\tau S_z + S_z = 0 \quad (6.26)$$

However, the protocol can't handle the noise of Ising terms (ZZ couplings) since $X_j X_k S_j^z S_k^z X_j X_k = S_j^z S_k^z$. The Ising terms remain untouched since the pulse drives both the qubit spin and bath spin.

6.3.2 Effective Hamiltonian

Yet, as we have mentioned above, the finite pulse duration t_p actually plays an important role in the dynamics. t_p can't be ignored especially when $\tau \sim t_p$ or $\tau < t_p$. Providing the sequence for four types of CP-like sequences, the effective Hamiltonian of the noisy system can be given by Magnus expansion. The average Hamiltonians (first order Magnus expansion) for the four protocols are easy to give

$$\text{CP: } \bar{\mathcal{H}}_0 = \frac{1}{t_c} [(4\tau + 2t_p)\beta S_z + 2t_p h S_x] \quad (6.27)$$

$$\text{APCP: } \bar{\mathcal{H}}_0 = \frac{1}{t_c} [(4\tau + 2t_p)\beta S_z] \quad (6.28)$$

$$\text{CPMG: } \bar{\mathcal{H}}_0 = \frac{1}{t_c} [(4\tau + 2t_p)\beta S_z + 2t_p h S_y] \quad (6.29)$$

$$\text{APCPMG: } \bar{\mathcal{H}}_0 = \frac{1}{t_c} [(4\tau + 2t_p)\beta S_z]. \quad (6.30)$$

The first order Hamiltonians are

$$\text{CP: } \bar{\mathcal{H}}_1 = 0 \quad (6.31)$$

$$\text{APCP: } \bar{\mathcal{H}}_1 = \frac{1}{2t_c} [h t_p \beta (2\tau + t_p) S_y] \quad (6.32)$$

$$\text{CPMG: } \bar{\mathcal{H}}_1 = 0 \quad (6.33)$$

$$\text{APCPMG: } \bar{\mathcal{H}}_1 = -\frac{1}{2t_c} [h t_p \beta (2\tau + t_p) S_x]. \quad (6.34)$$

The results are different from the derivations given in Barrett's work[29] since we used a simplified model of unlike spins, thus only Ising ($I_i^z I_j^z$) terms are preserved in the dipolar interaction.

6.4 Long-lived Coherence

The finite duration of pulses will lead to an accumulation of error due to the non-zero first order average Hamiltonian and therefore result in a much longer coherence time, up to 10^5 of T_2 [29][28]. The results we get from the Monte-Carlo assisted piece-wise model is displayed below. We prepare the spin qubit at y-axis $\rho(0) = |+i\rangle\langle+i|$ and apply periodic CP-like sequences on it, then measure the angular momentum $\langle S_y(t) \rangle$ at the end point of each time interval t_p and τ .

First, we look at the situation where the spin is placed in a bath with ensemble-averaged noise. Distributions of this noise in different dimensions are given in Fig. 3.5. The ensemble parameters is set at $T_2 = 1$. The long-lived coherence is observed in one, two, and three dimensions, as shown in Fig. 6.2.

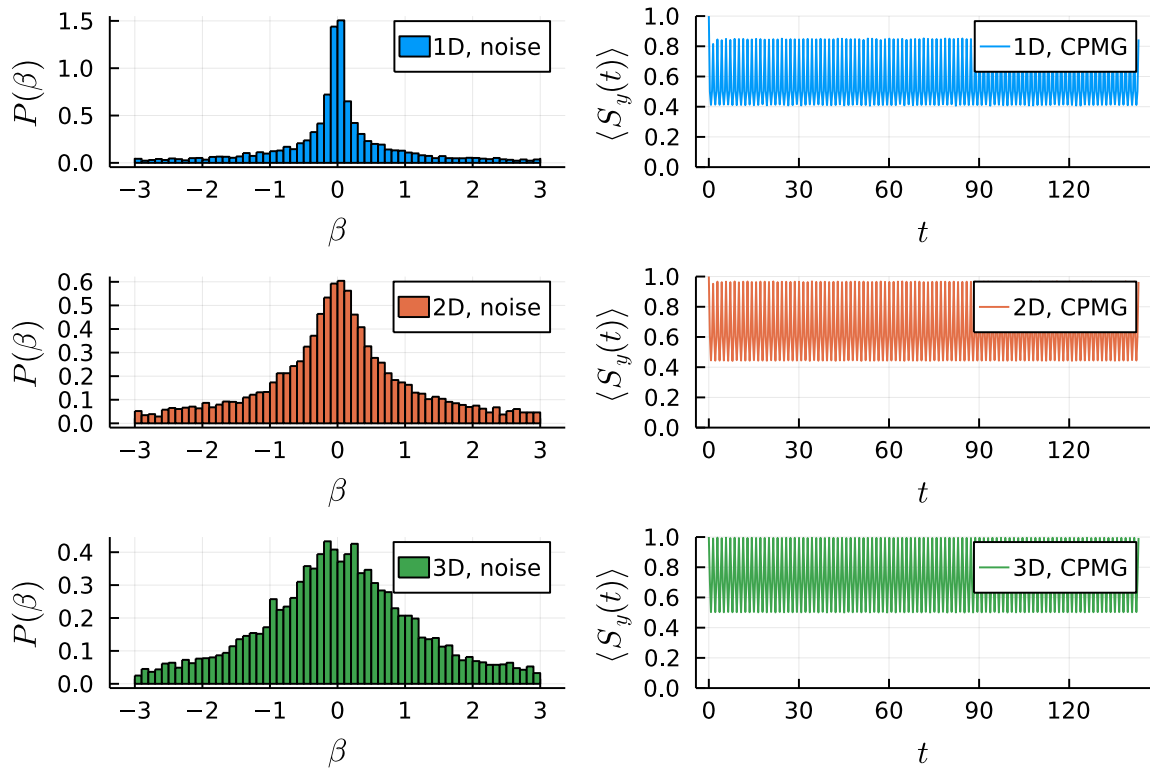


Figure 6.2: Dynamics of qubit under CPMG sequence, with ensemble averaged bath noise in different dimensions. Sequence parameters are set at $h = 100$ $\tau = 0.7$. Recall that $T_2 = 1$.

As suggested by previous research, independence of dimensionalities is a critical feature of the long-lived coherence[20]. Compare with 3D, the noise distributions in 1D, and 2D own

larger variance and extremely fatter tails, which has been discussed in Chapter. 3. However, envelope of spin echos (S_y) in 1D and 2D shows similar height ($\langle S_y(t) \rangle \approx 0.846$ for 1D, 0.965 for 2D, and 0.994 for 3D) as in 3D case, which indicates this phenomenon is very robust against the long tail noise spectrum in low dimensions.

6.4.1 Origin Mechanism

While the CP-like sequences are quite simple and similar in structure, they demonstrate completely different behaviors when applying to the qubit prepared at Y polarization. Among the four types of CP-like sequences, only APCP and CPMG demonstrate long-lived tails, due to the accumulation of higher-order terms in the Hamiltonian, as shown in Fig. 6.3. The polarization of qubit soon decays under the driving of CP and APCPMG sequence. Similar behaviors can be observed in 2D and 1D, as displayed in the appendix, Fig. C.15 and Fig. C.14.

Such a pattern has been demonstrated in the paper of Barrett.[29]. Our simplified model reproduced the results using the Monte-Carlo sampling instead of full-scale Hamiltonian simulations. This is a verification that the simulation produces the correct result.

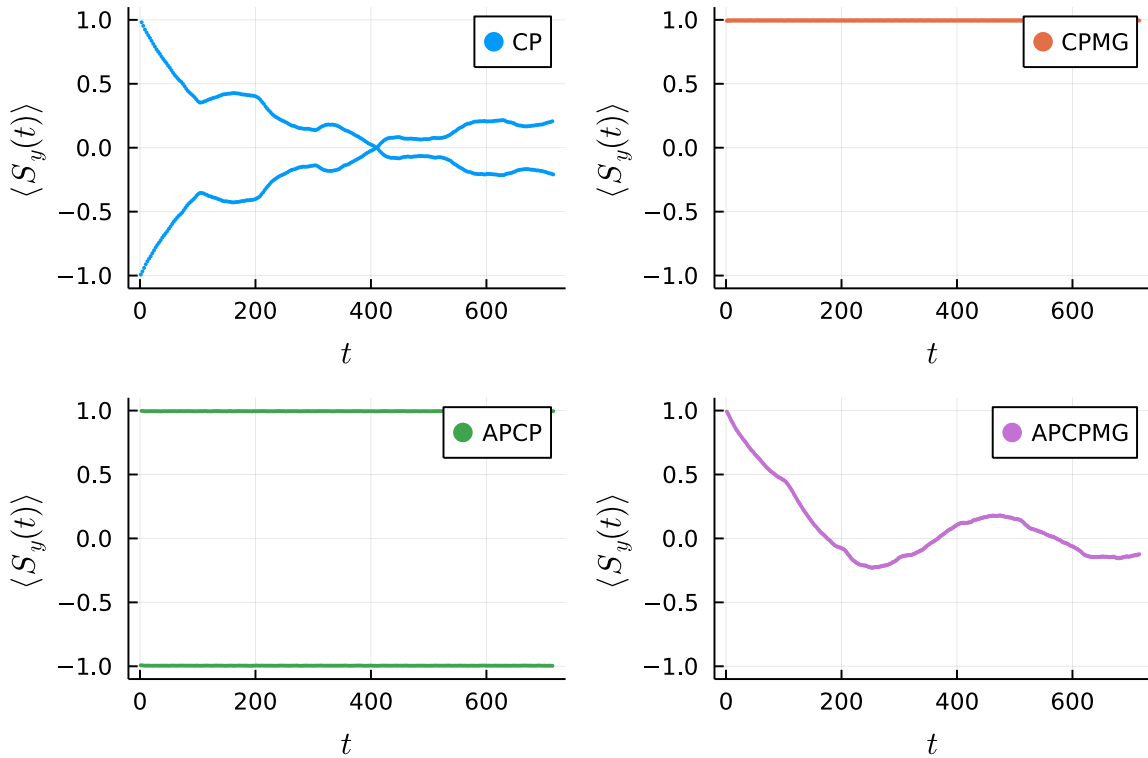


Figure 6.3: Spin echos envelope of $S_y(t)$ under different decoupling sequences in 3D. Sequence parameters are set at $h = 100$ $\tau = 0.7$.

The measurements are synchronized with the time points of spin echos, thus the curves shows an envelope of the periodic oscillations.

The origin of the long-lived coherence can be understood from the average Hamiltonian, as given in last section. It can be seen that the effective Hamiltonian of CPMG and APCP both possess similar form $\mathcal{H}_{\text{eff}} = \bar{\mathcal{H}}_0 + \bar{\mathcal{H}}_1 = \eta_y S_y + \eta_z S_z$. For CPMG sequence,

$$\mathcal{H}_{\text{eff}} = \bar{\mathcal{H}}_0 + \bar{\mathcal{H}}_1 = \beta S_z + \lambda h S_y, \quad \lambda = \frac{2t_p}{t_c} \quad (6.35)$$

where λ is the duty cycle of CPMG. The evolution of the average Hamiltonian equals an rotation

$$U_{\text{eff}}(t) = \exp(-i\mathcal{H}_{\text{eff}}t) = \exp\left[-i\Omega_{\text{eff}}t(\vec{n}_{\text{eff}} \cdot \vec{S})\right] \quad (6.36)$$

in which $\Omega_{\text{eff}} = \sqrt{\beta^2 + (\lambda h)^2}$, $\vec{n}_{\text{eff}} = (0, \lambda h/\Omega_{\text{eff}}, \beta/\Omega_{\text{eff}})$. The effective rotation locates on the YZ equator of Bloch sphere, with an polar angle $\theta = \pi/2 - \arcsin(\beta/\lambda h)$, as shown in Fig. 6.4.

As we can see in Fig. 6.4, the qubit state is prepared at the Y-axis at the beginning, and then start rotating around the axis \vec{n}_{eff} . Thus the trajectories of these rotations will be a set of circles centered at \vec{n}_{eff} and pass by Y-axis, which are plotted with blue dashed circles on the sphere.

Then $S_y(t, \beta)$ can be given using a little geometry knowledge,

$$S_y(t, \beta) = \cos^2(\epsilon) + \sin^2(\epsilon) \cos(t) = 1 - \frac{\beta^2}{h^2\lambda^2}(1 + \cos t), \quad \epsilon = \arcsin(\beta/\lambda h) \quad (6.37)$$

in which ϵ is the angle between \vec{n}_{eff} and Y axis.

At an echo time point $t_{\text{echo}} = n(2\tau + t_p)$, $n = 1, 2, 3, \dots$, $\langle S_y \rangle$ can be obtained by integrating over the distribution of β . If we assume that β obeys a distribution with linewidth b , that $b/\lambda h \ll 1$, then it can be expected that the rotation trajectories will be centralized in a smaller circle around Y-axis, thus the time average of $S_y(t)$ will be approximately 1. Hence the coherence is preserved. The situation is similar in APCP sequence, the effective Hamiltonian of which is also $\eta_y S_y + \eta_z S_z$. On the opposite, if the effective rotation is around X-axis, as in the cases in CP and APCPMG, the rotation trajectories will be a large circle close to the YZ equator. The average value of the Y component is therefore 0.

This simple and intuitive model provides a good view to understand the mechanism behind the long-lived coherence. Yet, it is still limited since we truncated all the high order terms in the Magnus expansion. Average Hamiltonian can not provide any information on the real trajectory of the spin state either, as only one single rotation is assumed. To investigate the sophisticated effect of control sequences in spin dynamics, exact simulation via Monte-Carlo methods is needed.

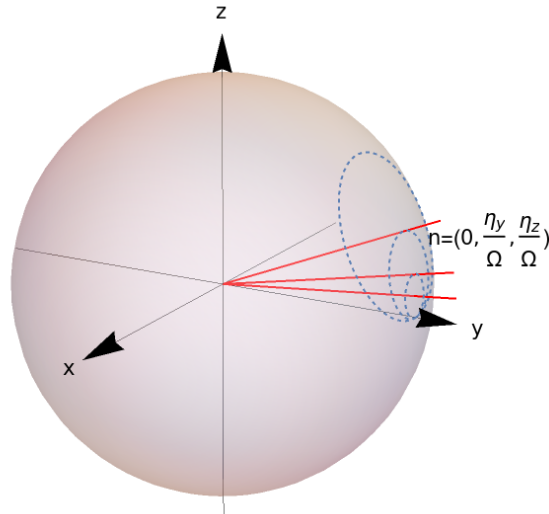


Figure 6.4: Effective rotation of average Hamiltonian

The effective rotation axes with different β are marked with a set of red lines. Trajectories of these rotations are plotted on the sphere as a set of blue dashed circles.

6.4.2 Effect of noise linewidth

As shown in the analysis above, the linewidth of noise distribution will directly affect the average height of the CPMG long-coherence. Such a behavior can be observed in Fig. 6.5. Here, the noise is set to Gaussian distribution centered at 0 with linewidth $b = 1, 5, 10$, the driving strength is set to $h = 10$. It can be observed that the height of spin echos is shorter with b increasing. This result suggests that the height of the spin echos produced by CPMG protocol depends on the standard deviation, or effective linewidth, of the corresponding noise distribution.

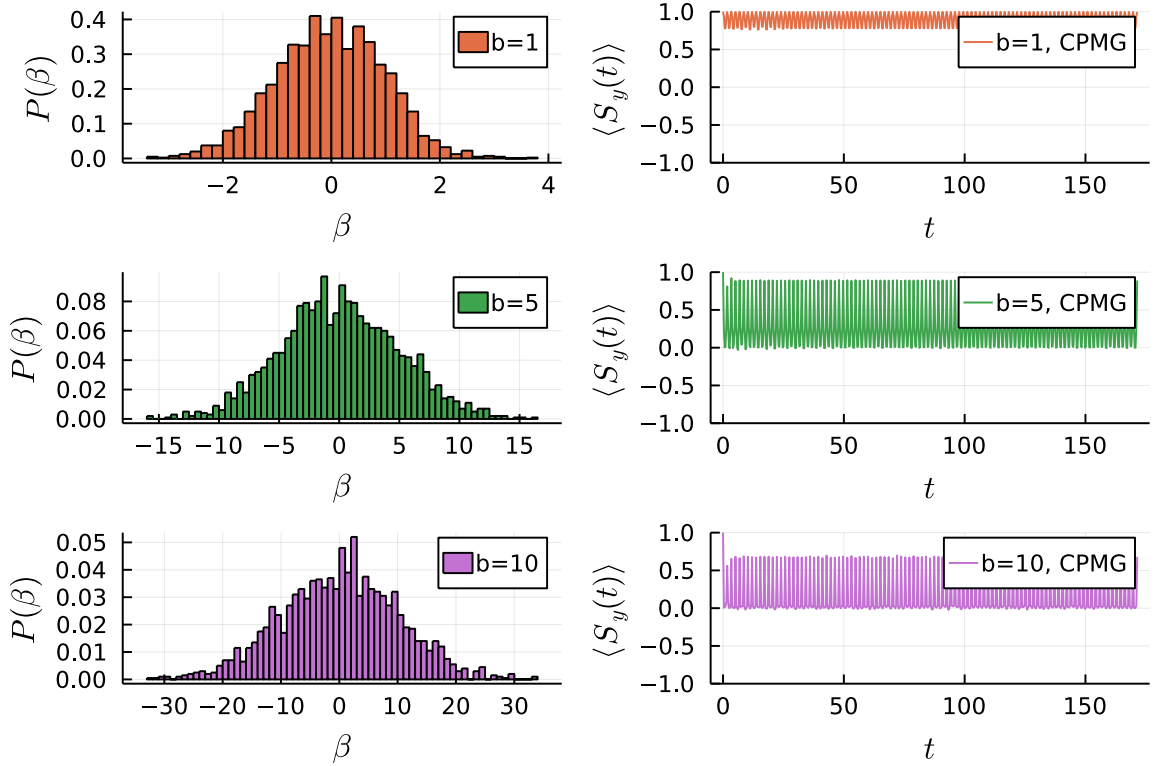


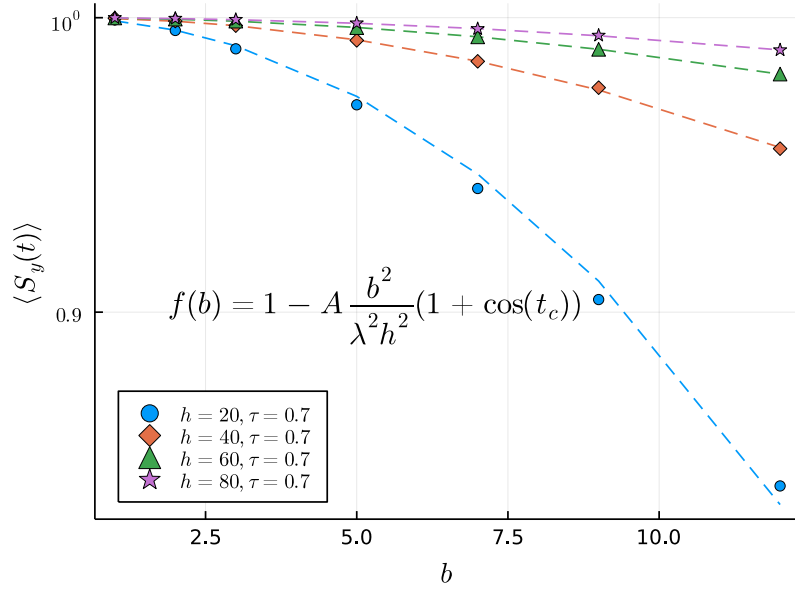
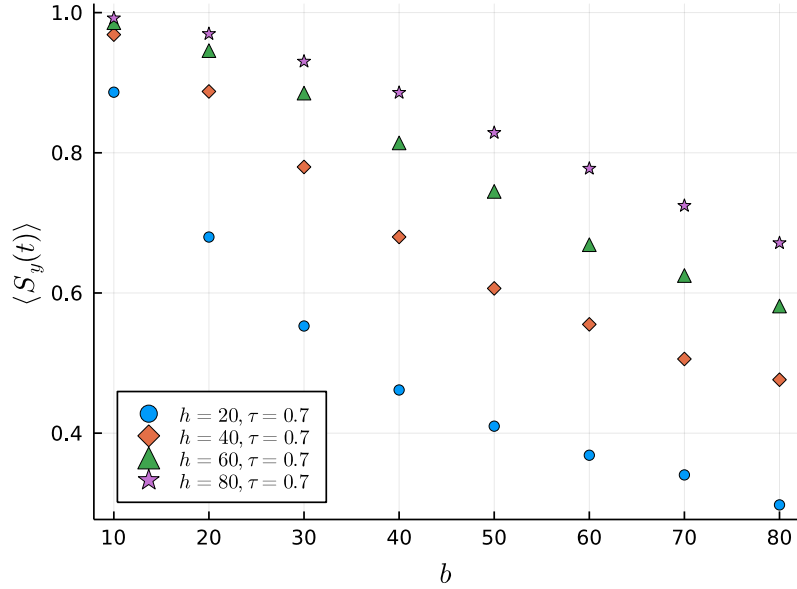
Figure 6.5: Relation between the noise linewidth and height of spin echos.

The noise is set to Gaussian distribution centered at 0 with linewidth $b = 2, 5, 10$. The parameters of CPMG are set to $h = 10, \tau = 0.7$.

Further investigation on the linewidth is shown in Fig. 6.6. Here, $\langle S_y(t) \rangle$ is the average height of spin echos under CPMG driving over time. The pulse-pulse interval of the sequence is fixed at $\tau = 0.7$. The value of b and h are chosen from both the weak driving regime $b \sim h$ and the strong-driving regime $h \gg b$.

We found that the decay of echo height in the strong-driving regime ($h \gg b$), as shown in subfigure (a), is well described by the quadratic decay predicted by the average Hamiltonian model, as given in Equation. 6.37. The dashed lines display the fitting of numerical results using quadratic decay. As we can see, the theoretical prediction of quadratic decay matches well with the simulation in this regime.

In the regime of strong noise, the height of spine echos decays quasi-linearly with the linewidth of noise b , as shown in Fig. 6.6, (b).

(a): Decay of echo height in the strong driving regime $h \gg b$.(b): Decay of echo height in weak driving regime $h \sim b$.Figure 6.6: Average height of spin echos under different driving strength h and noise linewidth b .

6.4.3 Effect of pulse-pulse interval

Different from the previous results, our model based on finite-duration pulses indicates that such a phenomenon also exists when pulse-pulse interval τ is close to T_2 ($\tau \approx 0.7$). Besides, the pulse-pulse interval τ lead to a completely different response to noise at the same driving strength, as shown in Fig. 6.6.

To further understand the role of pulse interval in CPMG, we set a fixed Gaussian noise with linewidth $b = 5$ and then observe the echo height at different values of τ . The spin qubit is set at S_y as before. The result is shown in Fig. 6.7.

The long-lived coherence emerges at both the long time regime $\tau > T_2$ and the short time regime $\tau < T_2$. This discovery is different from the previous research where the long-lived coherence does not present at $\tau > T_2$ [20].

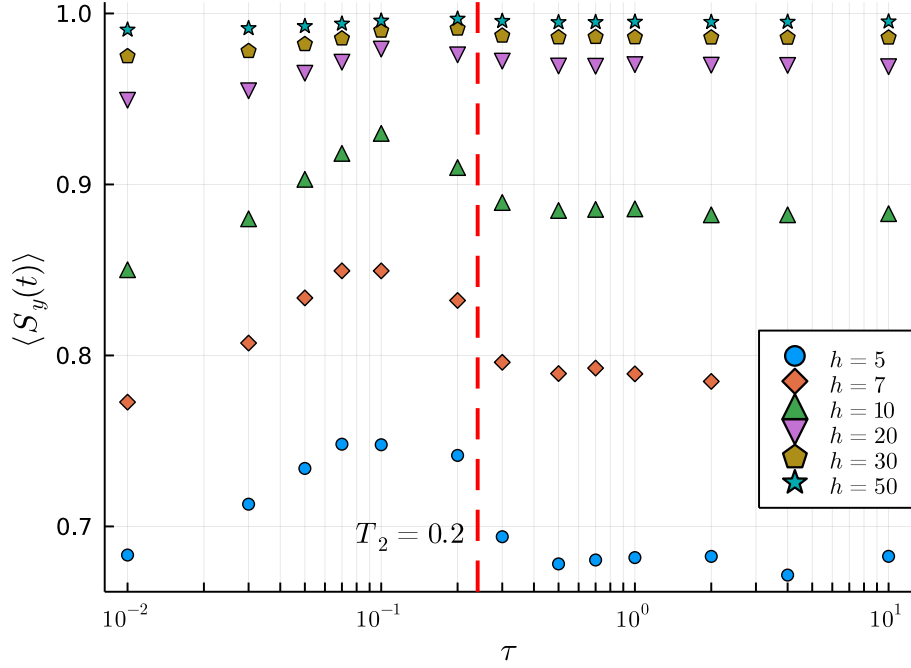


Figure 6.7: Average height of spin echoes under different driving strength h and noise linewidth τ . The noise linewidth is set at $b = 5$.

For strong driving $h \gg b$, the height of the spin echoes does not depend on τ in the time range we choose. Yet, for the weak driving case $h \sim b$, the performance of CPMG starts degenerating after $\tau > T_2$ as expected. Surprisingly, the average spin-echo height also decays at $\tau < 1/h$. A peak of echo height can be observed around $\tau = 1/h$. This result provides an interesting insight on the design of dynamical decoupling sequence, as it implies an optimal choice for τ at $\tau \approx 1/h(T_2^*)$.

Chapter 7

Conclusion

7.1 Summary and Discussion

In Chapter. 1, we identified decoherence as one of the most profound changes on the way to fully-fledged quantum technologies, and introduced noise mitigation based on quantum control as the main approach to handle the challenge. Focusing on spin systems, this thesis studied various problems in the quantum control techniques from a fundamental level of spin dynamics.

- In Chapter. 3, we identified a set of dimensionless parameters to characterize an ensemble of disordered and dilute bath spins. Based on this model, we demonstrated the average noise spectrum of a spin qubit interacting with bath spins via dipolar couplings in different dimensions. We found the effective noise in low dimensions demonstrates strong statistical fluctuation, characterized by a long tail in the average noise spectrum.
- In Chapter. 4, we studied the Rabi driving of the qubit surrounded by disordered bath spins in all different dimensions. Using Monte-Carlo simulation, we provided a long-time profile for continuous Rabi nutation under different driving strengths. Specifically, the continuous Rabi nutation demonstrates different asymptotic behaviors in the short-time regime and long-time regime, depending on dimensions. We identified the transition time between the two stages and provided a simple exponential model to describe the behaviors in different time regimes.
- In Chapter. 5, we demonstrated the distributions of errors presented in single quantum gates, including both errors on their rotating axis and errors on driving phases. We found that the phase error obeys a highly skewed distribution, with a long tail laid on the positive axis. The axis error obeys the same distribution of the effective noise in the strong driving regime. Based on these insights, we provided the average gate fidelities of single quantum gates under different driving strengths.
- In Chapter. 6, we studied the performance of Carr-Purcell typed dynamical decoupling protocols on the noisy spin qubit. We found that CP-type sequences can protect the qubit from decoherence in all one, two, and three dimensions, providing an extremely long coherence time. We found that the height of spin echos obeys a quadratic decay with noise linewidth in the strong driving regime, and decays linearly in the weak driving regime. The height of spin echos in the long lived coherence demonstrates a maximum around the inverse of driving strength $1/h$.

In summary, we studied the dynamics of a spin qubit interacting with disordered bath spins in 3D/2D/1D. By modeling the spin environment from fundamental dipolar couplings

and employing Monte-Carlo simulations, this research provides an insight into the precise driving and control of a noisy spin qubit, including the noise distribution, decoherence mechanism, driving error, gate fidelity, and performance of dynamical decoupling sequence. These knowledges will be helpful to the future design of quantum gates and potential decoupling protocols of spin qubits.

7.2 Outlook

Personally, I consider the work presented in this thesis unfinished. More problems can be investigated based on the results obtained in this thesis.

- First, I wish to visualize the motion of the spins under periodic pulse driving, by making moving trajectories on the Bloch sphere, in order to better understand its dynamics.
- Second, further exploring the parameter space of long-lived coherence would be helpful to understand the mechanism behind such a phenomenon.
- Third, the performance of various dynamical decoupling sequences (like XY-8) against noise can be further investigated using the noisy model.

The above questions can be answered by further exploiting the current model and numerical tools. Beyond this work, we can extend the environmental noise from a static distribution to a stochastic process (Ornstein-Uhlenbeck process) by considering the evolution of the system. Such a dynamical model is a better description to reality. Furthermore, the current model only considers a single spin qubit in a noisy bath. More problems can be investigated if introduce multiple qubits and their interactions in the system. For example, we can study the performance of two-qubit gates under a such noisy environment. The design of a better dynamical decoupling protocol to mitigate noise is also an exciting challenge. Aside from noise mitigation, the technique of quantum control can also be exploited to design a dynamically decoupled quantum gate. By better understanding the coupling between qubits and environment, we would be able to mitigate these noises in every operation performed on qubits, this would be an ultimate challenge on the way to general quantum information processing.

Bibliography

- [1] Anatole Abragam. *The principles of nuclear magnetism*. 32. Oxford university press, 1961.
- [2] Frank Arute et al. “Quantum supremacy using a programmable superconducting processor”. In: *Nature* 574.7779 (2019), pp. 505–510.
- [3] Ryan Babbush et al. “Focus beyond Quadratic Speedups for Error-Corrected Quantum Advantage”. In: *PRX Quantum* 2 (1 Mar. 2021), p. 010103. DOI: 10.1103/PRXQuantum.2.010103. URL: <https://link.aps.org/doi/10.1103/PRXQuantum.2.010103>.
- [4] Nir Bar-Gill et al. “Solid-state electronic spin coherence time approaching one second”. In: *Nature communications* 4.1 (2013), pp. 1–6.
- [5] Paul Benioff. “The computer as a physical system: A microscopic quantum mechanical Hamiltonian model of computers as represented by Turing machines”. In: *Journal of statistical physics* 22.5 (1980), pp. 563–591.
- [6] Charles H Bennett. “Logical reversibility of computation”. In: *IBM journal of Research and Development* 17.6 (1973), pp. 525–532.
- [7] F. Bloch. “Nuclear Induction”. In: *Phys. Rev.* 70 (7-8 Oct. 1946), pp. 460–474. DOI: 10.1103/PhysRev.70.460. URL: <https://link.aps.org/doi/10.1103/PhysRev.70.460>.
- [8] Cristian Bonato et al. “Optimized quantum sensing with a single electron spin using real-time adaptive measurements”. In: *Nature nanotechnology* 11.3 (2016), pp. 247–252.
- [9] C. E. Bradley et al. “A Ten-Qubit Solid-State Spin Register with Quantum Memory up to One Minute”. In: *Phys. Rev. X* 9 (3 Sept. 2019), p. 031045. DOI: 10.1103/PhysRevX.9.031045. URL: <https://link.aps.org/doi/10.1103/PhysRevX.9.031045>.
- [10] Jonas Bylander et al. “Noise spectroscopy through dynamical decoupling with a superconducting flux qubit”. In: *Nature Physics* 7.7 (2011), pp. 565–570.
- [11] Herman Y Carr and Edward M Purcell. “Effects of diffusion on free precession in nuclear magnetic resonance experiments”. In: *Physical review* 94.3 (1954), p. 630.
- [12] Christian L Degen, F Reinhard, and Paola Cappellaro. “Quantum sensing”. In: *Reviews of modern physics* 89.3 (2017), p. 035002.
- [13] VV Dobrovitski et al. “Decoherence dynamics of a single spin versus spin ensemble”. In: *Physical Review B* 77.24 (2008), p. 245212.
- [14] Bo L Dwyer et al. “Probing spin dynamics on diamond surfaces using a single quantum sensor”. In: *arXiv preprint arXiv:2103.12757* (2021).
- [15] Lara Faoro and Lev B. Ioffe. “Microscopic Origin of Low-Frequency Flux Noise in Josephson Circuits”. In: *Phys. Rev. Lett.* 100 (22 June 2008), p. 227005. DOI: 10.1103/PhysRevLett.100.227005. URL: <https://link.aps.org/doi/10.1103/PhysRevLett.100.227005>.

- [16] Edward B Fel'dman and Serge Lacelle. "Configurational averaging of dipolar interactions in magnetically diluted spin networks". In: *The Journal of chemical physics* 104.5 (1996), pp. 2000–2009.
- [17] Richard P Feynman. "Simulating Physics with Computers". In: *International Journal of Theoretical Physics* 21.6/7 (1982).
- [18] E. L. Hahn. "Spin Echoes". In: *Phys. Rev.* 80 (4 Nov. 1950), pp. 580–594. DOI: 10.1103/PhysRev.80.580. URL: <https://link.aps.org/doi/10.1103/PhysRev.80.580>.
- [19] Erwin L Hahn. "Nuclear induction due to free Larmor precession". In: *Physical Review* 77.2 (1950), p. 297.
- [20] Walter Hahn and VV Dobrovitski. "Long-lived coherence in driven many-spin systems: from two to infinite spatial dimensions". In: *New Journal of Physics* 23.7 (2021), p. 073029.
- [21] R Hanson et al. "Coherent dynamics of a single spin interacting with an adjustable spin bath". In: *Science* (2008).
- [22] Daniel Hetterich et al. "Detection and characterization of many-body localization in central spin models". In: *Phys. Rev. B* 98 (16 Oct. 2018), p. 161122. DOI: 10.1103/PhysRevB.98.161122. URL: <https://link.aps.org/doi/10.1103/PhysRevB.98.161122>.
- [23] Peter C Humphreys et al. "Deterministic delivery of remote entanglement on a quantum network". In: *Nature* 558.7709 (2018), pp. 268–273.
- [24] Alexander V. Khaetskii, Daniel Loss, and Leonid Glazman. "Electron Spin Decoherence in Quantum Dots due to Interaction with Nuclei". In: *Phys. Rev. Lett.* 88 (18 Apr. 2002), p. 186802. DOI: 10.1103/PhysRevLett.88.186802. URL: <https://link.aps.org/doi/10.1103/PhysRevLett.88.186802>.
- [25] G. de Lange et al. "Universal Dynamical Decoupling of a Single Solid-State Spin from a Spin Bath". In: *Science* 330.6000 (2010), pp. 60–63. DOI: 10.1126/science.1192739.
- [26] Harry Levine et al. "High-Fidelity Control and Entanglement of Rydberg-Atom Qubits". In: *Phys. Rev. Lett.* 121 (12 Sept. 2018), p. 123603. DOI: 10.1103/PhysRevLett.121.123603. URL: <https://link.aps.org/doi/10.1103/PhysRevLett.121.123603>.
- [27] Malcolm H Levitt. *Spin dynamics: basics of nuclear magnetic resonance*. John Wiley & Sons, 2013.
- [28] Dale Li et al. "Generating unexpected spin echoes in dipolar solids with π pulses". In: *Physical review letters* 98.19 (2007), p. 190401.
- [29] Dale Li et al. "Intrinsic origin of spin echoes in dipolar solids generated by strong π pulses". In: *Phys. Rev. B* 77 (21 June 2008), p. 214306. DOI: 10.1103/PhysRevB.77.214306. URL: <https://link.aps.org/doi/10.1103/PhysRevB.77.214306>.
- [30] Tom Manovitz et al. "Fast dynamical decoupling of the Mølmer-Sørensen entangling gate". In: *Physical review letters* 119.22 (2017), p. 220505.
- [31] JF Marques et al. "Logical-qubit operations in an error-detecting surface code". In: *Nature Physics* 18.1 (2022), pp. 80–86.
- [32] J. R. Maze, J. M. Taylor, and M. D. Lukin. "Electron spin decoherence of single nitrogen-vacancy defects in diamond". In: *Phys. Rev. B* 78 (9 Sept. 2008), p. 094303. DOI: 10.1103/PhysRevB.78.094303. URL: <https://link.aps.org/doi/10.1103/PhysRevB.78.094303>.
- [33] C. J. Mertens, T. A. B. Kennedy, and S. Swain. "Many-body theory of quantum noise". In: *Phys. Rev. Lett.* 71 (13 Sept. 1993), pp. 2014–2017. DOI: 10.1103/PhysRevLett.71.2014. URL: <https://link.aps.org/doi/10.1103/PhysRevLett.71.2014>.

- [34] Kevin C Miao et al. “Universal coherence protection in a solid-state spin qubit”. In: *Science* 369.6510 (2020), pp. 1493–1497.
- [35] Nissim Ofek et al. “Extending the lifetime of a quantum bit with error correction in superconducting circuits”. In: *Nature* 536.7617 (2016), pp. 441–445.
- [36] L. Petit et al. “Spin Lifetime and Charge Noise in Hot Silicon Quantum Dot Qubits”. In: *Phys. Rev. Lett.* 121 (7 Aug. 2018), p. 076801. DOI: 10.1103/PhysRevLett.121.076801. URL: <https://link.aps.org/doi/10.1103/PhysRevLett.121.076801>.
- [37] E. M. Purcell, H. C. Torrey, and R. V. Pound. “Resonance Absorption by Nuclear Magnetic Moments in a Solid”. In: *Phys. Rev.* 69 (1-2 Jan. 1946), pp. 37–38. DOI: 10.1103/PhysRev.69.37. URL: <https://link.aps.org/doi/10.1103/PhysRev.69.37>.
- [38] I. I. Rabi et al. “A New Method of Measuring Nuclear Magnetic Moment”. In: *Phys. Rev.* 53 (4 Feb. 1938), pp. 318–318. DOI: 10.1103/PhysRev.53.318. URL: <https://link.aps.org/doi/10.1103/PhysRev.53.318>.
- [39] Benjamin Schumacher. “Quantum coding”. In: *Phys. Rev. A* 51 (4 Apr. 1995), pp. 2738–2747. DOI: 10.1103/PhysRevA.51.2738. URL: <https://link.aps.org/doi/10.1103/PhysRevA.51.2738>.
- [40] Peter W Shor. “Fault-tolerant quantum computation”. In: *Proceedings of 37th Conference on Foundations of Computer Science*. IEEE, 1996, pp. 56–65.
- [41] Peter W. Shor. “Scheme for reducing decoherence in quantum computer memory”. In: *Phys. Rev. A* 52 (4 Oct. 1995), R2493–R2496. DOI: 10.1103/PhysRevA.52.R2493. URL: <https://link.aps.org/doi/10.1103/PhysRevA.52.R2493>.
- [42] Charles P Slichter. *Principles of magnetic resonance*. Vol. 1. Springer Science & Business Media, 2013.
- [43] Susumu Takahashi et al. “Quenching Spin Decoherence in Diamond through Spin Bath Polarization”. In: *Phys. Rev. Lett.* 101 (4 July 2008), p. 047601. DOI: 10.1103/PhysRevLett.101.047601. URL: <https://link.aps.org/doi/10.1103/PhysRevLett.101.047601>.
- [44] JM Taylor et al. “High-sensitivity diamond magnetometer with nanoscale resolution”. In: *Nature Physics* 4.10 (2008), pp. 810–816.
- [45] J. H. Van Vleck. “The Coupling of Angular Momentum Vectors in Molecules”. In: *Rev. Mod. Phys.* 23 (3 July 1951), pp. 213–227. DOI: 10.1103/RevModPhys.23.213. URL: <https://link.aps.org/doi/10.1103/RevModPhys.23.213>.
- [46] Lieven MK Vandersypen and Isaac L Chuang. “NMR techniques for quantum control and computation”. In: *Reviews of modern physics* 76.4 (2005), p. 1037.
- [47] M Veldhorst et al. “An addressable quantum dot qubit with fault-tolerant control-fidelity”. In: *Nature nanotechnology* 9.12 (2014), pp. 981–985.
- [48] Lorenza Viola, Emanuel Knill, and Seth Lloyd. “Dynamical Decoupling of Open Quantum Systems”. In: *Phys. Rev. Lett.* 82 (12 Mar. 1999), pp. 2417–2421. DOI: 10.1103/PhysRevLett.82.2417. URL: <https://link.aps.org/doi/10.1103/PhysRevLett.82.2417>.
- [49] Lorenza Viola, Seth Lloyd, and Emanuel Knill. “Universal Control of Decoupled Quantum Systems”. In: *Phys. Rev. Lett.* 83 (23 Dec. 1999), pp. 4888–4891. DOI: 10.1103/PhysRevLett.83.4888. URL: <https://link.aps.org/doi/10.1103/PhysRevLett.83.4888>.
- [50] Zhi-Hui Wang and Susumu Takahashi. “Spin decoherence and electron spin bath noise of a nitrogen-vacancy center in diamond”. In: *Physical Review B* 87.11 (2013), p. 115122.
- [51] Zhi-Hui Wang et al. “Comparison of dynamical decoupling protocols for a nitrogen-vacancy center in diamond”. In: *Phys. Rev. B* 85 (15 Apr. 2012), p. 155204. DOI: 10.1103/PhysRevB.85.155204. URL: <https://link.aps.org/doi/10.1103/PhysRevB.85.155204>.

- [52] TF Watson et al. “A programmable two-qubit quantum processor in silicon”. In: *nature* 555.7698 (2018), pp. 633–637.
- [53] J. S. Waugh, L. M. Huber, and U. Haeberlen. “Approach to High-Resolution nmr in Solids”. In: *Phys. Rev. Lett.* 20 (5 Jan. 1968), pp. 180–182. DOI: 10.1103/PhysRevLett.20.180. URL: <https://link.aps.org/doi/10.1103/PhysRevLett.20.180>.
- [54] Stephanie Wehner, David Elkouss, and Ronald Hanson. “Quantum internet: A vision for the road ahead”. In: *Science* 362.6412 (2018).
- [55] Xiangkun Xu et al. “Coherence-Protected Quantum Gate by Continuous Dynamical Decoupling in Diamond”. In: *Phys. Rev. Lett.* 109 (7 Aug. 2012), p. 070502. DOI: 10.1103/PhysRevLett.109.070502. URL: <https://link.aps.org/doi/10.1103/PhysRevLett.109.070502>.
- [56] Xiao Xue et al. “Quantum logic with spin qubits crossing the surface code threshold”. In: *Nature* 601.7893 (2022), pp. 343–347.
- [57] Juan Yin et al. “Satellite-based entanglement distribution over 1200 kilometers”. In: *Science* 356.6343 (2017), pp. 1140–1144.
- [58] H Dieter Zeh. “On the interpretation of measurement in quantum theory”. In: *Foundations of Physics* 1.1 (1970), pp. 69–76.
- [59] Hengyun Zhou et al. “Quantum Metrology with Strongly Interacting Spin Systems”. In: *Phys. Rev. X* 10 (3 July 2020), p. 031003. DOI: 10.1103/PhysRevX.10.031003. URL: <https://link.aps.org/doi/10.1103/PhysRevX.10.031003>.

Appendix A

Monte-Carlo Methods

As shown in the previous chapter 2.5.1, the environmental noise is equivalent to a fluctuation on the local field, defined by a bath spin state \vec{P}_p and a set of dipolar coupling strengths \vec{D}_ξ ,

$$\beta_{p,\xi} = \vec{P}_p \cdot \vec{D}_\xi \quad (\text{A.1})$$

in which the bath spin configuration is labeled by p , and the disorder realization (DR) is labeled by ξ .

The properties and dynamics of an ensemble of interacting spin clusters can thus be studied from a view of ensemble average [13].

$$\langle A \rangle = \frac{1}{N} \frac{1}{M} \sum_p \sum_\xi A(\beta_{p,\xi}) = \frac{1}{\mathcal{N}} \sum_\zeta A_\zeta, \quad (\text{A.2})$$

in which Eqn. 2.16 is used to obtain the expectation of one specific disorder realization. M, N are the total volume of eigenstates and disorder realizations respectively. Here $\zeta = (s, \xi) \in \Omega(s) \otimes \Omega(\xi)$ labels a combinational state of a specific spin configuration and a specific disorder realization. $\mathcal{N} = N \cdot M$ is the total number of possible combined states. Basically the combined ensemble is still microcanonical as the probability to reach each microstate is the same.

The Eqn. A.2 is simple in form but hard to compute in practice. The observable A_ζ must be evaluated for each ζ . Thus the calculation must be repeated by $\mathcal{N} = |\Omega(s) \otimes \Omega(\xi)| = 2^n \cdot \binom{m}{n}$ times. Obviously, the problem is non-polynomial, as its complexity grows super-exponentially.

Estimator

In such a situation, Monte-Carlo sampling can be used to effectively evaluate the result in a trade-off to precision [50]. Instead of iterate over the full space spanned by of \vec{P}_p and \vec{D}_ξ , the algorithm only samples a subspace with limited size \mathcal{M} , as shown below

$$\bar{A}_\mathcal{M} = \frac{1}{N'} \frac{1}{M'} \sum_{p=1}^{N'} \sum_{\xi=1}^{M'} A(\beta_{p,\xi}) = \frac{1}{\mathcal{M}} \sum_\zeta A_\zeta, \quad (\text{A.3})$$

\bar{A} is an *estimator* of $\langle A \rangle$ using the average calculated from a random sampled subspace. The volume of the subspace is $\mathcal{M} = M' N' < \mathcal{N}$.

Sampling

The spin configuration \vec{P}_p equals a bitstring of length n , we can randomly generate many bitstrings, with a total number $N' < N$. $\vec{P} \mapsto |0011 \dots 1001\rangle = |\uparrow\uparrow\downarrow\downarrow \dots \downarrow\uparrow\uparrow\downarrow\rangle$. Disorder

realization \vec{D} equals a set of occupations $\{\phi_i\}$ if we preserve the lattice. It can also be sampled from a bitstring $\{\phi_i\} = 0011 \dots 1001$ of length m with a Hamming weight n . If we ignore the lattice structure at a limit of dilute ensemble, then the positions can be generated as an array of random numbers, $\{\vec{r}_j\}$. However, singularity might be introduced into our system by assuming a continuous coordinates. D_j can be unreasonably large when a very small \vec{r}_j is generated by chance, as $D_j \propto 1/|\vec{r}_j|^3$. In reality, the maximum strength of a dipolar interaction between two spins is limited by the minimal lattice constant. Thus we can set a minimum threshold a distance that $\vec{r}_j > a$ for all j in order to eliminate the singularity.

Error

The error of Monte-Carlo estimator is given by the Chebychev inequality

$$P \left\{ |\bar{A}_{\mathcal{M}} - \langle A \rangle| \geq \left[\frac{\text{var}[A]}{\delta} \right]^{1/2} \right\} \leq \delta. \quad (\text{A.4})$$

in which $\text{var}[A]$ is the variance of A . It's given equivalently in the form of central limit theorem,

$$|\bar{A}_{\mathcal{M}} - \langle A \rangle| \sim \frac{\text{Normal}(0, \text{var}[A])}{\sqrt{\mathcal{M}}}, \quad (\text{A.5})$$

where $\text{Normal}(\mu, \sigma^2)$ denotes a normal distribution. As shown in the equation, the mean error of Monte-Carlo estimator decays with a square root of the sampling size, which can be given by

$$\delta[A] = \frac{\sigma[A]}{\sqrt{\mathcal{M}}} = \sqrt{\frac{1}{\mathcal{M}^2} \sum_{\zeta=1}^{\mathcal{M}} (A_{\zeta} - \bar{A})^2}. \quad (\text{A.6})$$

$\sigma[A]$ is the standard deviation of A .

Numerical analysis based on Monte-Carlo sampling will be the basic methodology used in this thesis.

Appendix B

Supplementary Derivations

B.1 Transformation of Joint Rotating Frame

The transformation from a static frame to a joint rotating frame

$$|\psi\rangle \rightarrow \prod_j e^{-i\tilde{\omega}_j S_j^z t} |\psi\rangle_R \quad (\text{B.1})$$

substitute this into the Schrodinger equation we will get

$$\begin{aligned} i\hbar \frac{d|\psi\rangle}{dt} = H |\psi\rangle &\Rightarrow i\hbar \frac{d}{dt} \left(e^{-it \sum_j \tilde{\omega}_j S_j^z} |\psi\rangle_R \right) = H e^{-it \sum_j \tilde{\omega}_j S_j^z} |\psi\rangle_R \\ i\hbar \left[-i \left(\sum_j \tilde{\omega}_j S_j^z \right) e^{-it \sum_j \tilde{\omega}_j S_j^z} |\psi\rangle_R + e^{-it \sum_j \tilde{\omega}_j S_j^z} \frac{d}{dt} |\psi\rangle_R \right] &= H e^{-it \sum_j \tilde{\omega}_j S_j^z} |\psi\rangle_R \\ i\hbar \left[-i \left(\sum_j \tilde{\omega}_j S_j^z \right) V |\psi\rangle_R + V \frac{d}{dt} |\psi\rangle_R \right] &= H V |\psi\rangle_R \end{aligned}$$

in which the transformation is denoted as $V = e^{-it \sum_j \tilde{\omega}_j S_j^z}$. The derivative on unitary is treated as normal since the S_j^z are commute to each other and they are all diagonal. Substitute the equation in rotating frame into the formula

$$i\hbar \frac{d|\psi\rangle_R}{dt} = H_R |\psi\rangle_R$$

We get that

$$\left(\sum_j \tilde{\omega}_j S_j^z \right) V |\psi\rangle_R + V H_R |\psi\rangle_R = H V |\psi\rangle_R \Rightarrow V H_R = H V - \hbar \left(\sum_j \tilde{\omega}_j S_j^z \right) V$$

The final expression for H_R

$$H_R = V^\dagger H V - \hbar \omega_0 \left(\sum_j S_j^z \right) \quad (\text{B.2})$$

since V is commute to S_j^z .

B.2 Two-Spin Interaction Hamiltonian in Rotating Frame

Let the unitary V be a transformation to joint rotating frame of two spins

$$V = e^{-i\tilde{\omega}_1 S_1^z t} e^{-i\tilde{\omega}_2 S_2^z t} = e^{-i\tilde{\omega}_1 t/2(\sigma_z \otimes I)} e^{-i\tilde{\omega}_2 t/2(I \otimes \sigma_z)} = e^{-i\tilde{\omega}_1 t/2\sigma_z} \otimes e^{-i\tilde{\omega}_2 t/2\sigma_z} \quad (\text{B.3})$$

Then we have

$$[S_1^z, S_2^z] = 0 \Rightarrow V^\dagger S_1^z S_2^z V = S_1^z S_2^z \quad (\text{B.4})$$

$$V^\dagger S_1^x S_2^z V = \frac{1}{4} e^{+i\tilde{\omega}_1 t/2\sigma_z} \sigma_x e^{-i\tilde{\omega}_1 t/2\sigma_z} \otimes \sigma_z = \cos(\tilde{\omega}_1 t) S_1^x S_2^z - \sin(\tilde{\omega}_1 t) S_1^y S_2^z \quad (\text{B.5})$$

similarly we get

$$V^\dagger S_1^y S_2^z V = \cos(\tilde{\omega}_1 t) S_1^y S_2^z + \sin(\tilde{\omega}_1 t) S_1^x S_2^z \quad (\text{B.6})$$

using the fact that

$$\begin{aligned} (\cos A + i \sin A \sigma_z) \sigma_x (\cos A - i \sin A \sigma_z) &= \cos^2 A \sigma_x + \sin^2 A \sigma_z \sigma_x \sigma_z + i \sin A \cos A [\sigma_z, \sigma_x] \\ &= (\cos^2 A - \sin^2 A) \sigma_x - 2 \sin A \cos A \sigma_y \\ &= \cos(2A) \sigma_x - \sin(2A) \sigma_y \\ (\cos A + i \sin A \sigma_z) \sigma_y (\cos A - i \sin A \sigma_z) &= \cos^2 A \sigma_y + \sin^2 A \sigma_z \sigma_y \sigma_z + i \sin A \cos A [\sigma_z, \sigma_y] \\ &= (\cos^2 A - \sin^2 A) \sigma_y + 2 \sin A \cos A \sigma_x \\ &= \cos(2A) \sigma_y + \sin(2A) \sigma_x \end{aligned}$$

Then for the crossing terms

$$\begin{aligned} V^\dagger S_1^x S_2^y V &= [\cos(\tilde{\omega}_1 t) S_x - \sin(\tilde{\omega}_1 t) S_y] \otimes [\cos(\tilde{\omega}_2 t) S_y + \sin(\tilde{\omega}_2 t) S_x] \\ &= \cos(\tilde{\omega}_1 t) \cos(\tilde{\omega}_2 t) S_1^x S_2^y - \sin(\tilde{\omega}_1 t) \sin(\tilde{\omega}_2 t) S_1^y S_2^x \\ &\quad + \cos(\tilde{\omega}_1 t) \sin(\tilde{\omega}_2 t) S_1^x S_2^x - \sin(\tilde{\omega}_2 t) \cos(\tilde{\omega}_1 t) S_1^y S_2^y \end{aligned}$$

To get $V^\dagger S_1^x S_2^y V$, we only need to switch the indices 1, 2.

The xx and yy terms can be obtained similarly

$$\begin{aligned} V^\dagger S_1^x S_2^x V &= \cos(\tilde{\omega}_1 t) \cos(\tilde{\omega}_2 t) S_1^x S_2^x + \sin(\tilde{\omega}_1 t) \sin(\tilde{\omega}_2 t) S_1^y S_2^y \\ &\quad - \cos(\tilde{\omega}_1 t) \sin(\tilde{\omega}_2 t) S_1^x S_2^y - \sin(\tilde{\omega}_2 t) \cos(\tilde{\omega}_1 t) S_1^y S_2^x \\ V^\dagger S_1^y S_2^y V &= \cos(\tilde{\omega}_1 t) \cos(\tilde{\omega}_2 t) S_1^y S_2^y + \sin(\tilde{\omega}_1 t) \sin(\tilde{\omega}_2 t) S_1^x S_2^x \\ &\quad + \cos(\tilde{\omega}_1 t) \sin(\tilde{\omega}_2 t) S_1^y S_2^x + \sin(\tilde{\omega}_2 t) \cos(\tilde{\omega}_1 t) S_1^x S_2^y \end{aligned}$$

The flip-flop term $xx+yy$ can be calculated as above, but it's better to use the ladder operator form. First we calculate the transformation on ladder operators,

$$\begin{aligned} (\cos A + i \sin A \sigma_z) \sigma_+ (\cos A - i \sin A \sigma_z) &= \cos^2 A \sigma_+ + \sin^2 A \sigma_z \sigma_+ \sigma_z + i \sin A \cos A [\sigma_z, \sigma_+] \\ &= \cos(2A) \sigma_+ + i \sin(2A) \sigma_+ \\ &= \exp(i2A) \sigma_+ \end{aligned}$$

notice that the lowering operator have an opposite sign on commutation.

$$(\cos A + i \sin A \sigma_z) \sigma_- (\cos A - i \sin A \sigma_z) = \cos(2A) \sigma_- - i \sin(2A) \sigma_- = \exp(-i2A) \sigma_-$$

The following basic properties are used

$$\sigma_z \sigma_+ \sigma_z = \frac{1}{2} \sigma_z (\sigma_x + i\sigma_y) \sigma_z = \frac{1}{2} (-\sigma_x - i\sigma_y) = -\sigma_+, \quad \sigma_z \sigma_- \sigma_z = -\sigma_-$$

$$\begin{aligned} [\sigma_z, \sigma_+] &= \frac{1}{2} ([\sigma_z, \sigma_x] + i[\sigma_z, \sigma_y]) = \frac{1}{2}(2i\sigma_y + 2\sigma_x) = 2\sigma_+ \\ [\sigma_z, \sigma_-] &= \frac{1}{2} ([\sigma_z, \sigma_x] - i[\sigma_z, \sigma_y]) = \frac{1}{2}(2i\sigma_y - 2\sigma_x) = -2\sigma_- \end{aligned}$$

$$V^\dagger \sigma_1^+ \sigma_2^- V = e^{+i\tilde{\omega}_1 t/2\sigma_z} \sigma_+ e^{-i\tilde{\omega}_1 t/2\sigma_z} \otimes e^{+i\tilde{\omega}_2 t/2\sigma_z} \sigma_- e^{-i\tilde{\omega}_2 t/2\sigma_z} = \sigma_+ \otimes \sigma_- e^{i(\tilde{\omega}_1 - \tilde{\omega}_2)t} \quad (\text{B.7})$$

$$V^\dagger \sigma_1^- \sigma_2^+ V = \sigma_- \otimes \sigma_+ e^{-i(\tilde{\omega}_1 - \tilde{\omega}_2)t} \quad (\text{B.8})$$

Therefore the $\vec{S}_1 \cdot \vec{S}_2$ contains Ising(zz) and flip-flop and is secular. The crossing terms in $(\vec{S}_1 \cdot \vec{n})(\vec{S}_2 \cdot \vec{n})$ are more tricky. Of course zz should be preserved as well. All the terms that contains only one z spin should be dropped.

Notice that the crossing terms $S_1^x S_2^y$ are also oscillating since that

$$V^\dagger (S_1^x S_2^y + S_1^y S_2^x) V = \cos(2\omega_0 t) (S_1^x S_2^y + S_1^y S_2^x)$$

The following term should be treated carefully

$$V^\dagger (n_x^2 S_1^x S_2^x + n_y^2 S_1^y S_2^y) V$$

since it contains both secular and non secular terms.

A convenient way is using direct matrix product

$$V^\dagger (n_x^2 S_1^x S_2^x + n_y^2 S_1^y S_2^y) V = \frac{1}{4} \begin{pmatrix} 0 & 0 & 0 & e^{it(\omega_1 + \omega_2)} (n_x^2 - n_y^2) \\ 0 & 0 & e^{it(\omega_1 - \omega_2)} (n_x^2 + n_y^2) & 0 \\ 0 & e^{-it(\omega_1 - \omega_2)} (n_x^2 + n_y^2) & 0 & 0 \\ e^{-it(\omega_1 + \omega_2)} (n_x^2 - n_y^2) & 0 & 0 & 0 \end{pmatrix}$$

B.2.1 Like Spins

For like spins, $e^{it(\omega_1 - \omega_2)} \approx 1$ is secular, while $e^{it(\omega_1 + \omega_2)}$ is oscillating and thus non-secular.

The fast oscillating entries can be dropped, then the remained part is

$$\frac{1}{4} \begin{pmatrix} 0 & 0 & 0 & 0 \\ 0 & 0 & e^{it(\omega_1 - \omega_2)} (n_x^2 + n_y^2) & 0 \\ 0 & e^{-it(\omega_1 - \omega_2)} (n_x^2 + n_y^2) & 0 & 0 \\ 0 & 0 & 0 & 0 \end{pmatrix} \approx \frac{1}{2} (n_x^2 + n_y^2) (S_1^x S_2^x + S_1^y S_2^y)$$

After dropping all non-secular terms, the Hamiltonian is transformed into

$$\mathcal{H}_D^R = \frac{1}{|\vec{r}_{12}|^3} [3(n_x^2 S_1^x S_2^x + n_y^2 S_1^y S_2^y + n_z^2 S_1^z S_2^z) - (S_1^x S_2^x + S_1^y S_2^y + S_1^z S_2^z)] \quad (\text{B.9})$$

Then for like spins

$$\mathcal{H}_D = \frac{1 - 3n_z^2}{2|\vec{r}_{12}|^3} (\vec{S}_1 \cdot \vec{S}_2 - 3S_1^z S_2^z)$$

in which we used that $n_x^2 + n_y^2 + n_z^2 = 1$,

$$(n_x, n_y, n_z) = (\sin \theta \cos \phi, \sin \theta \sin \phi, \cos \theta)$$

write elementary vector in spherical coordinate then you can get the formula of dipolar coupling strength

$$D_{12} = \frac{1 - 3 \cos^2 \theta}{2|\vec{r}_{12}|^3}$$

B.2.2 Unlike Spins

However, for unlike spins $|\omega_1 + \omega_2| \gg D, b$. So the terms related $e^{i(\tilde{\omega}_1 - \tilde{\omega}_2)t}$ are also oscillating and should be dropped. The only remained part is the zz terms.

The result is

$$H_D^R = \frac{1}{|\vec{r}_{12}|^3} (3n_z^2 - 1) S_1^z S_2^z$$

B.3 Effective Field

The eigenvalue can be found by

$$\hat{B} = \sum_j 2D_j S_j^z = \sum_j D_j \sigma_j^z = \mathbb{1} \otimes \sum_j D_j \mathbb{1}^{\otimes(j-1)} \otimes \sigma_z \otimes \mathbb{1}^{\otimes(n-j)}$$

If we take $n = 2$ then we will get

$$B_b = D_1(\sigma_z \otimes \mathbb{1}) + D_2(\mathbb{1} \otimes \sigma_z) = \begin{pmatrix} D_1 + D_2 & 0 & 0 & 0 \\ 0 & D_2 - D_1 & 0 & 0 \\ 0 & 0 & D_1 - D_2 & 0 \\ 0 & 0 & 0 & -D_1 - D_2 \end{pmatrix}$$

The formula can be easily extended into multiple spins. Thus the eigenvalue of β_p is

$$\beta_p = \sum_j p_j D_j, \quad p_j = \pm 1 \quad (\text{B.10})$$

B.4 Free Induction Decay

The experimnt initializes an spin at transverse axis $|+\rangle$ and then observes the spontaneous decay of the polarization. Consider a spin cluster of $n + 1$ unlike spins, in which the central spin qubit is labeled by '0', and the spin bath labeled 'b'. The Hamiltonian of the system is then given by an Ising-type interactions that can be exactly solved.

$$\mathcal{H} = \sum_{j=1}^n 2\hbar D_j S_j^z S_0^z \quad (\text{B.11})$$

in which $S_0^z = S_z \otimes \mathbb{1}_b$, and $S_j^z = \frac{1}{2} \mathbb{1}^{\otimes j} \otimes \sigma_z \otimes \mathbb{1}^{\otimes(n-j+1)}$. The $\mathbb{1}_b = \mathbb{1}^{\otimes n}$ is an identity matrix on bath space, of 2^n dimension. $\sigma_j, j = x, y, z$ are Pauli matrices.

The central spin qubit is initialized at a mixed state polarized on the x axis.

$$\rho_0 = \frac{1 - \lambda}{2} \mathbb{1} + \lambda |+\rangle\langle +| = \frac{1}{2} \mathbb{1} + \lambda S_x \quad (\text{B.12})$$

in which $0 < \lambda < 1$ is a coefficient characterizing the probability of $|+\rangle$ in the mixed state. The initial state of the spin bath is $\rho_b = 2^{-n} \mathbb{1}_b$ as given by the assumption of hot spin bath.

We want to know its angular momentum on x axis as a function of time.

$$f(t) \propto \langle S_0^x(t) \rangle = \text{Tr} \left\{ U(t) \rho(0) U^\dagger(t) S_0^x \right\} = 2^{-n} \lambda \text{Tr} \left\{ U S_0^x U^\dagger S_0^x \right\} \quad (\text{B.13})$$

in which the initial state is $\rho(0) = \rho_0(0) \otimes \rho_b(0)$. The formula can be simplified as $f(t) = 2 \langle S_0^x S_0^x(t) \rangle$. Here a factor 2 is added before $\langle S_0^x(t) \rangle$ since the angular momentum of spin-1/2 is associated with a 1/2 factor.

The time evolution is a unitary, assuming that the system is closed, which can be given by

$$U(t) = \exp(-i\mathcal{H}t/\hbar) = \prod_j e^{-i2D_j S_j^z S_0^z t}, \quad (\text{B.14})$$

as all the Ising terms $S_j^z S_0^z$ in the summation is commute with each other.

Given that $(\sigma_1^z \sigma_2^z)^2 = 1$, then the time evolution of Ising Hamiltonian is $e^{-iA\sigma_1^z \sigma_2^z t} = \cos(At) - i \sin(At)\sigma_1^z \sigma_2^z$. Here $S_z = \sigma_z/2$, substitute the expression we can get that

$$U(t) = \prod_j U_j(t) = \prod_j [\cos(D_j t/2) - i \sin(D_j t/2)\sigma_0^z \sigma_j^z] \quad (\text{B.15})$$

Substitute the unitary into the expression of $f(t)$, expand the term

$$\begin{aligned} U S_0^x U^\dagger S_0^x &= \frac{1}{4} \sigma_0^x \left\{ \dots U_3 U_2 [\cos(D_1 t/2) - i \sin(D_1 t/2)\sigma_0^z \sigma_1^z] \sigma_0^x [\cos(D_1 t/2) + i \sin(D_1 t/2)\sigma_0^z \sigma_1^z] U_2^\dagger U_3^\dagger \dots \right\} \\ &= \frac{1}{4} \sigma_0^x \left\{ \dots (\cos(D_1 t/2)^2 - \sin(D_1 t/2)^2) \sigma_0^x - 2i \sin(D_1 t/2) \cos(D_1 t/2) \sigma_1^z \sigma_0^y \dots \right\} \\ &= \frac{1}{4} \sigma_0^x \left\{ \dots U_3 U_2 [\cos(D_1 t)\sigma_0^x - i \sin(D_1 t)\sigma_1^z \sigma_0^y] U_2^\dagger U_3^\dagger \dots \right\} \end{aligned}$$

in which we used $\sigma_0^z \sigma_0^x \sigma_0^z = -\sigma_0^x$ (anti-commute) and $[\sigma_0^x, \sigma_0^z] = -2i\sigma_0^y$.

Noticing that $\text{Tr}[\sigma_0^x \sigma_0^x] = 2^{n+1}$, $\text{Tr}[\sigma_0^x \sigma_0^y] = 0$, the only remaining term after trace will be $\cos(D_j t)$. Thus the final result is

$$\langle S_0^x(t) \rangle = \frac{1}{2^n} \text{Tr} [U S_0^x U^\dagger S_0^x] = \frac{1}{2} \prod_j \cos(D_j t). \quad (\text{B.16})$$

Another approach is

$$\langle S_0^x(t) \rangle = \frac{1}{N} \sum_{p=1}^N \langle p | S_0^x(t) | p \rangle. \quad (\text{B.17})$$

The value of an observable on eigenstates can be given by

$$\langle p | S_0^x(t) | p \rangle = \langle p | U S_0^x U^\dagger S_0^x | p \rangle = \langle p | U | p \rangle \langle p | S_0^x | p \rangle \langle p | U^\dagger | p \rangle \langle p | S_0^x | p \rangle, \quad (\text{B.18})$$

since the \mathcal{H} is diagonal on the subspace of bath. The projection on the subspace is given by $\langle p | S_0^x | p \rangle = S_x$, and

$$\langle p | U | p \rangle = \langle p | e^{-i\mathcal{H}t/\hbar} | p \rangle = e^{-i\langle p | \mathcal{H} | p \rangle t/\hbar}, \quad (\text{B.19})$$

The unitary is thus given by

$$U_p = \langle p | U | p \rangle = \cos(\beta_p t/2) - i \sin(\beta_p t/2) \sigma_z \quad (\text{B.20})$$

noticing that $\langle p | \mathcal{H} | p \rangle = \hbar \langle p | \hat{B}_b \otimes S_z | p \rangle = \hbar \beta_p S_z$. Therefore, the observable on a specific substate is

$$\langle p | S_0^x(t) | p \rangle = \text{Tr} \left\{ S_x U_p S_x U_p^\dagger \right\} = \frac{1}{2} \cos(\beta_p t). \quad (\text{B.21})$$

Thus the normalized decoherence curve $f(t) = 2 \langle S_0^x(t) \rangle$ is given by

$$f(t) = \frac{1}{N} \sum_{p=1}^N f_s(t) = \frac{1}{N} \sum_{p=1}^N \cos(\beta_p t). \quad (\text{B.22})$$

Use the formula of triangle functions $\cos(\omega_1 t) \cos(\omega_2 t) = \frac{1}{2} [\cos(\omega_1 + \omega_2) t + \cos(\omega_1 - \omega_2) t]$, it can be proved that Eqn. B.16 is equivalent to Eqn. B.22

$$\begin{aligned} \langle S_0^x(t) \rangle &= \frac{1}{2^n} \sum_{\{p_j\}} \cos \left((D_1 + \sum_{j=2}^n p_j D_j) \cdot t \right), p_j = \pm 1 \\ &= \frac{1}{2^N} \sum_{p=1}^N \cos(|\vec{P}_p \cdot \vec{D}| t) \\ &= \frac{1}{2} \left[\frac{1}{N} \sum_{p=1}^N \cos(\beta_p t) \right] \end{aligned} \quad (\text{B.23})$$

B.5 Equivalent Noise

This approach can be easily justified since $\beta_p = \langle p | \hat{\beta} | p \rangle$ is just an eigenvalue on some eigenstate p . The Hilbert space is of 2^n dimension, and the β_p almost forms a continuous spectrum given a large enough quantum system with $n \gg 1$. In the sum over p , we can count the number of β_p appears in an interval $(B, B + \Delta B)$,

$$N(B) = |\{\beta_p | B \leq \beta_p \leq B + \Delta B\}|$$

Then we get the probability density function $P(B)$.

$$\Pr[B \leq \beta_p \leq B + \Delta B] = \frac{N(B)}{N} = \int_B^{B+\Delta B} P(\beta) d\beta, N = 2^n$$

$$\lim_{\Delta B \rightarrow 0} P(B) \Delta B = \lim_{N \rightarrow \infty} \frac{1}{N} \sum_{p=1}^N \delta(B - \beta_p)$$

We can write the PDF of β directly

$$P(\beta) = \frac{1}{N} \sum_{p=1}^N \delta(\beta - \beta_p) \quad (\text{B.24})$$

This formula follows the definition of discrete probability density function

$$P(t) = \sum_{i=1}^n p_i \delta(t - x_i) \quad (\text{B.25})$$

in which p_i is the probability of t being at x_i . We can see it is well normalized.

$$\int_{-\infty}^{\infty} P(\beta) d\beta = \frac{1}{N} \sum_{p=1}^N \int_{-\infty}^{\infty} \delta(\beta - \beta_p) d\beta = \frac{1}{N} \sum_{p=1}^N 1 = 1 \quad (\text{B.26})$$

B.6 Observable on Subspace Eigenstates

Consider a spin cluster with $n + 1$ spins, in which the central spin is labeled by '0', and rest n spins are labeled by 'b',

Given a central qubit Hamiltonian taking the form

$$H = \sum_j D_j S_j^z S_0^z + h S_0^x,$$

and its unitary defined by $U = r^{-iHt/\hbar}$, we want to find the value of observable S_0^x projected on a bath eigenstate $|s\rangle \in \mathcal{S}_b$.

The observable on an eigenstate can be expanded using projective operators, $\sum_q |q\rangle\langle q| = \mathbb{1}_b$, which also applies to r, s .

$$\langle p|S_0^x(t)|p\rangle = \langle p|US_0^xU^\dagger S_0^x|p\rangle = \sum_{q,r,s} \langle p|S_0^x|q\rangle\langle q|U|r\rangle\langle r|S_0^x|s\rangle\langle s|U^\dagger|p\rangle$$

It can be proved that the term is not zero only when $p = q = r = s$ on the eigen basis,

a) S_0^x

$$\langle r|S_0^x|s\rangle = \langle r|S_x \otimes \mathbb{1}_b|s\rangle = S_x \langle r|\mathbb{1}_b|s\rangle = \begin{cases} 0, r \neq s \\ S_x, r = s \end{cases}$$

2) $U(t)$

$$\langle p|e^{-iHt}|q\rangle = \langle p|\mathbb{1}^{\otimes(n+1)}|q\rangle - i\langle p|H|q\rangle t - \frac{1}{2}\langle p|H^2|q\rangle t^2 + \dots$$

in which

$$H = BS_0^z + hS_0^x = (\mathbb{1} \otimes B_b)(S_z \otimes \mathbb{1}_b) + h(S_x \otimes \mathbb{1}_b) = S_z \otimes B_b + h(S_x \otimes \mathbb{1}_b)$$

$$\langle p|H|q\rangle = \langle p|B_b|q\rangle \otimes S_z + h\langle p|\mathbb{1}_b|q\rangle \otimes S_x = \begin{cases} 0, p \neq q \\ \beta_p S_z + hS_x, p = q \end{cases}$$

The β_p is an effective magnetic field. We can rewrite the non zero case as

$$\langle p|H|p\rangle = \beta_p S_z + hS_x = \omega_p(n_{p,x}\sigma_x + n_{p,z}\sigma_z) = \omega_p(\vec{n}_p \cdot \vec{\sigma})$$

in which we normalized the pointer state with $\omega_p = \frac{1}{2}(\beta_p^2 + h^2)^{1/2}$. for higher order terms, we have

$$\langle p|H^2|p\rangle = \langle p|B^2(S_0^z)^2 + h^2(S_0^x)^2 + Bh\{S_0^x, S_0^z\}|q\rangle = \langle p|B^2|q\rangle + h^2\langle p|\mathbb{1}^{\otimes(n+1)}|q\rangle$$

Here $(S_0^z)^2 = (S_0^x)^2 = \mathbb{1}^{\otimes(n+1)}$, anti-commutator $\{S_0^x, S_0^z\} = 0$. Noticing that $B = \mathbb{1} \otimes B_b = \sum_j 2D_j S_j^z$ is a diagonal matrix, which means B_b is also a diagonal matrix, then we can get

$$\langle p|B^2|q\rangle = \mathbb{1} \otimes \langle p|B_b^2|q\rangle = \mathbb{1} \otimes \begin{cases} \beta_p^2, \text{ if } p = q \\ 0, \text{ else} \end{cases}$$

the same applies for $\langle p|\mathbb{1}^{\otimes(n+1)}|q\rangle$. Hence $\langle p|H^2|q\rangle = \omega_p^2 \mathbb{1}$. Thus the term is not zero only when $p = q = r = s$. The summation should include just one label p .

Use the result we get above, we can easily find that

$$e^{-i\langle p|H|p\rangle t} = e^{-i\omega_p t(\vec{n}_p \cdot \vec{\sigma})} = \cos(\omega_p t) - i \sin(\omega_p t)(\vec{n}_p \cdot \vec{\sigma}) \quad (\text{B.27})$$

and

$$\begin{aligned} \langle p|e^{-iHt}|p\rangle &= \langle p|\mathbb{1}^{\otimes(n+1)}|p\rangle - i\langle p|H|p\rangle t - \frac{1}{2!}\langle p|H^2|p\rangle t^2 + \frac{1}{3!}i\langle p|H^3|p\rangle t^3 + \dots \\ &= 1 - i\omega_p t(\vec{n}_p \cdot \vec{\sigma}) - \frac{1}{2}\omega_p^2 t^2 + i\frac{1}{3!}\omega_p^3 t^3(\vec{n}_p \cdot \vec{\sigma}) + \dots \\ &= \cos(\omega_p t) - i \sin(\omega_p t)(\vec{n}_p \cdot \vec{\sigma}) \end{aligned}$$

Therefore we get $\langle p|e^{-iHt}|p\rangle = e^{-i\langle p|H|p\rangle t}$. The observable is

$$\langle p|S_0^x(t)|p\rangle = \langle p|U|p\rangle \langle p|S_0^x|p\rangle \langle p|U^\dagger|p\rangle \langle p|S_0^x|p\rangle$$

B.7 Van Vleck Momentum

At $t = 0$, we have

$$M_k|_{t=0} = \int_{-\infty}^{\infty} \beta^k P(\beta) d\beta = \frac{1}{N} \sum_p \int_{-\infty}^{\infty} \beta^k \delta(\beta - \beta_p) d\beta = \frac{1}{N} \sum_p \beta_p^k \quad (\text{B.28})$$

here we dropped the constant $(-i)^k$

Then we can substitute into Eqn. 2.22, with $\beta = \sum_{j=1}^n p_j D_j$.

$$\begin{aligned} M_2 &= \frac{1}{N} \sum_{p=1}^N \left(\sum_i p_i D_i \right) \left(\sum_j p_j D_j \right), \quad p_{i,j} = \pm 1 \\ &= \frac{1}{N} \sum_{p=1}^N \left(\sum_i p_i^2 D_i^2 \right) + \frac{1}{N} \sum_{p=1}^N \left(\sum_{i \neq j} p_i p_j D_i D_j \right), \quad p_{i,j} = \pm 1 \\ &= \frac{1}{N} \sum_{p=1}^N \sum_i D_i^2, \quad \leftarrow p_i p_j = \pm 1, p_i^2 = 1 \\ &= \sum_i D_i^2 \end{aligned} \quad (\text{B.29})$$

The fourth order momentum is

$$M_4 = \frac{1}{N} \sum_{p=1}^N \left(\sum_{i,j,k,l} p_i p_j p_k p_l D_i D_j D_k D_l \right), \quad p_{i,j} = \pm 1 \quad (\text{B.30})$$

Let's focus on the prefactor $p_i p_j p_k p_l$. Since $p_i = \pm 1$, the summation is always zero if the $p_i p_j p_k p_l = \pm 1$. The summation is non-zero only when $p_i p_j p_k p_l = 1$, or $p_i p_j p_k p_l = -1$, we can discuss these cases in detail.

a)

$$i = j, k = l, j \neq k \Rightarrow p_i p_j p_k p_l = 1,$$

To pick 2 indices from 4, we have $\binom{4}{2}/2 = 3$ choices. Then the valid indices is reduced from 4 to 2. For the remained 2 indices,

$$\sum_i \sum_j D_i^2 D_j^2 = \left(\sum_i D_i^2 \right) \left(\sum_j D_j^2 \right) = \sum_{j=i} D_j^4 + \sum_i \sum_{j \neq i} D_i^2 D_j^2$$

Therefore, the summation from case a) is

$$M_4^{(a)} = 3 \sum_i \sum_{j \neq i} D_i^2 D_j^2 = 3 \left[\left(\sum_i D_i^2 \right)^2 - \sum_j D_j^4 \right] \quad (\text{B.31})$$

the condition $i \neq j$ means we need to subtract the diagonal terms (i, i) from the pairs of (i, j)

b)

$$i = j, k = l, j = k \Leftrightarrow i = j = l = l \Rightarrow p_i p_j p_k p_l = 1,$$

the summation is simply

$$M_4^{(b)} = \sum_j D_j^4 \quad (\text{B.32})$$

Finally we arrive the summation of all non-zero terms that forms M_4

$$M_4 = M_4^{(a)} + M_4^{(b)} = 3\left(\sum_i D_i^2\right)^2 - 2\sum_j D_j^4 \quad (\text{B.33})$$

For a Gaussian distribution

$$\mathcal{N}(0, b) = \frac{1}{\sqrt{2\pi b}} e^{-\frac{x^2}{2b^2}} \quad (\text{B.34})$$

Its characteristic function is

$$f(t) = \int_{-\infty}^{\infty} \frac{1}{\sqrt{2\pi b}} e^{-\frac{x^2}{2b^2}} e^{-ixt} dx = e^{-\frac{1}{2}b^2 t^2} \quad (\text{B.35})$$

the second order momentum is

$$M_2 = \frac{d^2 f}{dt^2} = b^2 e^{-\frac{1}{2}b^2 t^2} (b^2 t^2 - 1) \quad (\text{B.36})$$

the fourth order momentum is

$$M_4 = \frac{d^4 f}{dt^4} = b^4 e^{-\frac{1}{2}b^2 t^2} (b^4 t^4 - 6b^2 t^2 + 3) \quad (\text{B.37})$$

B.8 Driving Hamiltonian in Rotating Frame

Then the total Hamiltonian for the cluster under a driving field is $\mathcal{H} = \mathcal{H}_Z + \mathcal{H}_D + \mathcal{H}_C$, in which the \mathcal{H}_Z is the magnetization energy and \mathcal{H}_D is the dipolar interactions, $\mathcal{H}_C(t)$ is the driving field.

Consider one spin qubit labeled by j , the total Hamiltonian of this qubit in rotating frame is given by $\mathcal{H}_j = \hbar(\omega_j - \tilde{\omega}_j)I_0^z + V_j^\dagger H_{D,i} V_j + V_j^\dagger \mathcal{H}_{C,j} V_j$, in which $V_j = e^{i\tilde{\omega}_j t I_j^z}$, ω_j is its Larmor frequency. The control term is given by

$$\begin{aligned} V_j^\dagger \mathcal{H}_{C,j} V_j &= -\hbar\gamma_j B e^{i\tilde{\omega}_j t I_j^z} [\cos(\omega_c t + \phi) I_j^x + \sin(\omega_c t + \phi) I_j^y] e^{-i\tilde{\omega}_j t I_j^z} \\ &= -\hbar\gamma_j B [I_j^x \cos((\omega_C - \tilde{\omega}_j)t + \phi) + I_j^y \sin((\omega_C - \tilde{\omega}_j)t + \phi)]. \end{aligned}$$

The dipolar Hamiltonian in the rotating frame is given by $V_j^\dagger H_{D,i} V_j = \sum_{i=1}^N 2D_{ij} I_i^z I_j^z$. Set $j = 0$ as the label of central spin qubit, and substitute above results into the formula, then we can get that

$$\begin{aligned} \mathcal{H}_0 &= \hbar(\omega_0 - \tilde{\omega}_0) I_0^z + \sum_{i=1}^N 2D_{i0} I_i^z I_0^z \\ &\quad - \hbar\gamma_0 B [I_0^x \cos((\omega_C - \tilde{\omega}_0)t + \phi) + I_0^y \sin((\omega_C - \tilde{\omega}_0)t + \phi)]. \end{aligned} \quad (\text{B.38})$$

B.9 Ensemble Averaged FID

B.9.1 One Dimension, D=1

Let θ be the angle between the 1D spin chain and the external field.

$$\langle G(t) \rangle_c = \exp\left\{-\rho \int_{-\infty}^{\infty} \left[1 - \cos\left(\frac{1 - 3\cos^2(\theta)}{2r^3} \gamma^2 \hbar t\right)\right] dr\right\} \quad (\text{B.39})$$

$$= \exp\left\{-\rho \int_{-\infty}^{\infty} \left[1 - \cos\left(\frac{a^3}{r^3}\right)\right] dr\right\} \quad (\text{B.40})$$

in which we define a constant $a^3 = (1 - 3 \cos^2(\theta)) \gamma^2 \hbar t / 2$ and particle density $\rho = N/V$. Focus on the integral part

$$\begin{aligned}
 \int_{-\infty}^{\infty} \left[1 - \cos\left(\frac{a^3}{r^3}\right) \right] dr &= 2 \int_0^{\infty} \left[1 - \cos\left(\frac{a^3}{r^3}\right) \right] dr \leftarrow \cos(x) = \cos(-x) \\
 &= 2 \lim_{r \rightarrow 0} \int_0^{a^3/r^3} [1 - \cos(u)] \left(-\frac{a}{3}\right) (-1)^{1/3} u^{-4/3} du \leftarrow u = \frac{a^3}{r^3} \\
 &= 2 \int_0^{\infty} [1 - \cos(u)] \left(-\frac{|a|}{3}\right) (-1)^{1/3} u^{-4/3} du \\
 &= \frac{2|a|}{3} \int_0^{\infty} (1 - \cos u) u^{-4/3} du \\
 &= \frac{2|a|}{3} \left(-\frac{\sqrt{3}}{2}\right) \Gamma\left(-\frac{1}{3}\right)
 \end{aligned}$$

We used the integral formula of negative Gamma function in the last step

$$\int_0^{\infty} x^{\alpha-1} (1 - \cos x) dx = -\cos\left(\frac{\pi\alpha}{2}\right) \Gamma(\alpha), \quad -2 < \text{Re } \alpha < 0 \quad (\text{B.41})$$

Then we can substitute the integral result into Eqn. B.40

$$\langle G(t) \rangle_c = \exp \left\{ -\frac{2\rho}{3} \left| \frac{1 - 3 \cos^2(\theta)}{2} \gamma^2 \hbar t \right|^{1/3} S_1 \right\} \quad (\text{B.42})$$

in which

$$S_1 = -\frac{\sqrt{3}}{2} \Gamma\left(-\frac{1}{3}\right)$$

B.9.2 Two Dimension, D=2

In 2D plane, the volume element is $dv = r dr d\varphi$. Assume the angle between the external field and the plane is θ . The angle between a location vector and the projection of the external field is φ . Then the angle Θ between a location vector and the external field is $\cos(\Theta) = \cos(\theta) \cos(\varphi)$.

$$\langle G(t) \rangle_c = \exp \left\{ -\rho \int_0^{2\pi} \int_0^{\infty} \left[1 - \cos\left(\frac{1 - 3 \cos^2(\Theta)}{2r^3} \gamma^2 \hbar t\right) \right] r dr d\varphi \right\} \quad (\text{B.43})$$

$$= \exp \left\{ -\rho \int_0^{2\pi} \int_0^{\infty} \left[1 - \cos\left(\frac{a^3}{r^3}\right) \right] r dr d\varphi \right\} \quad (\text{B.44})$$

Focus on the integral first

$$\begin{aligned}
 \int_0^{\infty} \left[1 - \cos\left(\frac{a^3}{r^3}\right) \right] r dr &= \int_0^{\infty} [1 - \cos(u)] (au^{-1/3}) \left(-\frac{a}{3}\right) (-1)^{1/3} u^{-4/3} du \\
 &= \frac{a^2}{3} \int_0^{\infty} (1 - \cos u) u^{-5/3} du \\
 &= \frac{a^2}{3} \left(-\frac{1}{2}\right) \Gamma\left(-\frac{2}{3}\right)
 \end{aligned}$$

The a contains ϕ so we need to do integral again

$$\Phi(\theta) = \int_0^{2\pi} |1 - 3 \cos^2(\theta) \cos^2(\varphi)|^{2/3} d\varphi \quad (\text{B.45})$$

Here θ is a constant. $\theta = 0$ when the external field is parallel to the plane. $\theta = \pi/2$ when the external field is perpendicular to the plane. For these two case we get $\Phi(0) \approx 6.01$ and $\Phi(\pi/2) = 2\pi$

Write the final form of the formula, with $S_2 = (-\frac{1}{2}) \Gamma(-\frac{2}{3})$.

$$\langle G(t) \rangle_c = \exp \left\{ -\frac{\rho}{3} \left(\frac{\gamma^2 \hbar t}{2} \right)^{2/3} \Phi(\theta) S_2 \right\} \quad (\text{B.46})$$

When $\theta = \pi/2$, we get

$$\langle G(t) \rangle_c = \exp \left\{ \frac{\pi \rho}{3} \Gamma \left(-\frac{2}{3} \right) \left(\frac{\gamma^2 \hbar t}{2} \right)^{2/3} \right\} \quad (\text{B.47})$$

B.9.3 Three Dimension, D=3

Pick the external field at z direction. The volume element is $dv = r^2 \sin(\theta) dr d\theta d\varphi$

$$\langle G(t) \rangle_c = \exp \left\{ -\rho \int_0^{2\pi} \int_0^\pi \int_0^\infty \left[1 - \cos \left(\frac{1 - 3 \cos^2(\theta)}{2r^3} \gamma^2 \hbar t \right) \right] r^2 \sin(\theta) dr d\theta d\varphi \right\} \quad (\text{B.48})$$

Use the same approach

$$\int_0^\infty \left[1 - \cos \left(\frac{a^3}{r^3} \right) \right] r^2 dr = \int_0^\infty [1 - \cos(u)] (au^{-1/3})^2 \left(-\frac{a}{3}\right) (-1)^{1/3} u^{-4/3} du \quad (\text{B.49})$$

$$= \frac{|a|^3}{3} \int_0^\infty (1 - \cos u) u^{-2} du \quad (\text{B.50})$$

$$(\text{B.51})$$

In which

$$S_3 = \int_0^\infty (1 - \cos u) u^{-2} du = 2 \int_0^\infty \frac{\sin(u/2)^2}{u^2} du = \int_0^\infty \left(\frac{\sin x}{x} \right)^2 dx = \frac{\pi}{2} \quad (\text{B.52})$$

The remained part of integral is

$$\begin{aligned} \Phi &= \int_0^{2\pi} \int_0^\pi |1 - 3 \cos^2(\theta)| \sin(\theta) d\theta d\varphi \\ &= 2\pi \int_{-1}^1 |1 - 3 \cos^2(\theta)| d \cos(\theta) \\ &= 4\pi \left[\int_0^{1/\sqrt{3}} (1 - 3x^2) dx + \int_{1/\sqrt{3}}^1 (1 - 3x^2) dx \right] \\ &= 2\pi \cdot \frac{8}{3\sqrt{3}} \end{aligned}$$

The numerical constant comes from the angular integral. Substitute into the formula

$$\langle G(t) \rangle_c = \exp \left\{ -\frac{\rho}{3} \left(\frac{\gamma^2 \hbar t}{2} \right) \Phi S_3 \right\} = \exp \left\{ -\frac{1}{6} \rho \pi^2 \gamma^2 \hbar t \cdot \frac{8}{3\sqrt{3}} \right\} \quad (\text{B.53})$$

This is exactly the result we can see from textbook [1] (except the 1/3 constant from 'truncated coupling strength').

B.10 Ensemble Average Noise

$$\begin{aligned}
 P(B) &= \int_0^\infty P(b)P(B)db \\
 &= \int_0^\infty \frac{1}{\sqrt{2\pi b^2}} \exp\left(-\frac{B^2}{2b^2}\right) \frac{1}{b^2} \sqrt{\frac{2}{\pi}} \Gamma \exp\left(-\frac{\Gamma^2}{2b^2}\right) db \\
 &= \frac{\Gamma}{\pi} \int_0^\infty \frac{1}{b^3} \exp\left(-\frac{B^2 + \Gamma^2}{2b^2}\right) db \\
 &= -\frac{\Gamma}{2\pi} \int_0^\infty \exp\left(-\frac{B^2 + \Gamma^2}{2} u\right) du \leftarrow u = \frac{1}{b^2} \\
 &= -\frac{\Gamma}{2\pi} \frac{2}{B^2 + \Gamma^2} \exp\left(-\frac{B^2 + \Gamma^2}{2} u\right) \Big|_0^\infty \\
 &= \frac{\Gamma}{\pi(B^2 + \Gamma^2)},
 \end{aligned} \tag{B.54}$$

B.11 Rabi Driving with Approximate Noise

Gaussian

As we have seen from the Equation.4.13, the evolution unitary of H is

$$U(\beta; t) = e^{-iHt} = \cos(\omega t) - i \sin(\omega t)(\vec{n} \cdot \vec{\sigma}), \quad \omega = \frac{1}{2}\sqrt{\beta^2 + h^2}$$

in which $\vec{n} \cdot \vec{\sigma} = n_x \sigma_x + n_z \sigma_z$ and $n_x = \frac{h}{\Omega}, n_z = \frac{\beta}{\Omega}$.

The Gaussian noise is centered at zero with linewidth b . Thus $h \gg b$ suggests $h \gg |\beta|$. Assume $h \gg |\beta| \Rightarrow n_x \approx 1, n_z \approx 0$. So we can approximate the unitary by $\vec{n} \cdot \vec{\sigma} \approx \sigma_x$

$$\tilde{U}(\beta; t) \approx \cos(\omega t) - i \sin(\omega t) \sigma_x = e^{-i\omega \sigma_x t} = e^{-i\Omega S_x t} \tag{B.55}$$

noticing that $S_x = \frac{1}{2}\sigma_x$ and $\Omega = 2\omega$ Thus

$$\begin{aligned}
 \langle S_z(t) \rangle &\approx \text{Tr}\left\{S_z \tilde{U}(\beta; t) S_z \tilde{U}(\beta; t)^\dagger\right\} = +\frac{1}{2} \cos(\Omega t) \\
 \langle S_y(t) \rangle &\approx \text{Tr}\left\{S_y \tilde{U}(\beta; t) S_z \tilde{U}(\beta; t)^\dagger\right\} = -\frac{1}{2} \sin(\Omega t)
 \end{aligned} \tag{B.56}$$

Obviously $\langle S_x(t) \rangle \approx 0$ since the unitary is rotation around x axis. These results can also be derived from Equation. B.64, Equation. B.63, Equation. B.60 by using $n_x \approx 1, n_z \approx 0$.

Then we start considering the noise spectrum, The Rabi oscillation can be rewrite as

$$S_z(t) = \frac{1}{2} \text{Re} \int_{-\infty}^{\infty} e^{-i\Omega t} P(\beta) d\beta, \quad S_y(t) = \frac{1}{2} \text{Im} \int_{-\infty}^{\infty} e^{-i\Omega t} P(\beta) d\beta \tag{B.57}$$

This formula is quite similar with the characteristic function of $P(\beta)$ but it is more complicated. When $P(\beta)$ subject to Gaussian distribution, we can define $F(t)$

$$F(t) = \int_{-\infty}^{\infty} e^{-i\Omega t} P(\beta) d\beta = \frac{e^{-iht}}{\sqrt{1 + i\frac{b^2 t}{h}}} \tag{B.58}$$

The integral is calculated as following

$$\begin{aligned}
 \int_{-\infty}^{\infty} e^{-i\Omega t} P(\beta) d\beta &= \int_{-\infty}^{\infty} \frac{1}{\sqrt{2\pi b}} e^{-\frac{\beta^2}{2b^2}} e^{-it\left(\frac{\beta^2}{2h} + h\right)} d\beta \\
 &= \frac{1}{\sqrt{2\pi b}} e^{-iht} \int_{-\infty}^{\infty} e^{-\left(\frac{1}{b^2} + i\frac{t}{h}\right)\frac{\beta^2}{2}} d\beta \\
 &= \frac{1}{\sqrt{2\pi b}} e^{-iht} \int_{-\infty}^{\infty} e^{-\frac{\beta^2}{2\xi^2}} d\beta \\
 &= \frac{\xi}{b} e^{-iht}
 \end{aligned}$$

in which we used that

$$\Omega = \sqrt{\beta^2 + h^2} \approx h + \frac{\beta^2}{2h} + O(\beta)^4, \quad \xi^2 = \left(\frac{1}{b^2} + i\frac{t}{h}\right)^{-1}.$$

Lorentzian

$$\begin{aligned}
 S_z(t) &= \frac{1}{2} \operatorname{Re} \int_{-\infty}^{\infty} P(B) e^{i\Omega t} dB = \frac{1}{2} \operatorname{Re}\{F(t)\} \\
 &\approx \operatorname{Re} \frac{2\Gamma}{\pi} e^{iht} \int_0^{\infty} \frac{1}{B^2 + \Gamma^2} \exp\left\{i\frac{B^2}{2h}t\right\} dB \leftarrow \Omega = \sqrt{B^2 + h^2} \approx h + \frac{B^2}{2h} + O(B)^3
 \end{aligned}$$

according to NIST handbook of special integrals

$$\operatorname{erfc}(az) = \frac{2z}{\pi} e^{-a^2 z^2} \int_0^{\infty} \frac{\exp(-a^2 t^2)}{t^2 + z^2} dt \quad (\text{B.59})$$

The integral part can be evaluated

$$\begin{aligned}
 I &= \int_0^{\infty} \frac{1}{B^2 + \Gamma^2} \exp\left\{i\frac{B^2}{2h}t\right\} dB \\
 &= \int_0^{\infty} \frac{\exp(-a^2 t^2)}{t^2 + z^2} dt \leftarrow a^2 = -\frac{it}{2h}, z = \Gamma \\
 &= \operatorname{erfc}(az) e^{a^2 z^2} \frac{\pi}{2z} \\
 &= \operatorname{erfc}\left(\frac{1-i}{\sqrt{2}} \sqrt{\frac{t}{2h}} \Gamma\right) e^{-\frac{i\Gamma^2 t}{2h}} \frac{\pi}{2\Gamma}
 \end{aligned}$$

Substitute it back into the formula we get

B.12 Exact solution of Rabi driving

$$\begin{aligned}
 z_p(t) &= \operatorname{Tr}\left[S_z U_p(t) S_z U_p(t)^\dagger\right] \\
 &= \frac{1}{4} \operatorname{Tr}\left\{\sigma_z \left([\cos^2(\omega_p t) \sigma_z + \sin^2(\omega_p t) (\vec{n}_p \cdot \vec{\sigma}) \sigma_z (\vec{n}_p \cdot \vec{\sigma})] + i \sin(\omega_p t) \cos(\omega_p t) [\sigma_z, (\vec{n}_p \cdot \vec{\sigma})]\right)\right\} \\
 &= \frac{1}{4} \operatorname{Tr}\left\{\sigma_z \left([\cos^2(\omega_p t) \sigma_z + \sin^2(\omega_p t) ((n_{p,z}^2 - n_{p,x}^2) \sigma_z + 2n_z n_x \sigma_x)] - 2n_{p,x} \sin(\omega_p t) \cos(\omega_p t) \sigma_y\right)\right\} \\
 &= \frac{1}{2} [\cos^2(\omega_p t) + \sin^2(\omega_p t) (n_{p,z}^2 - n_{p,x}^2)]
 \end{aligned} \quad (\text{B.60})$$

in which we used that

$$(\vec{n}_p \cdot \vec{\sigma})\sigma_z(\vec{n}_p \cdot \vec{\sigma}) = (n_{p,x}\sigma_x + n_{p,z}\sigma_z)\sigma_z(n_{p,x}\sigma_x + n_{p,z}\sigma_z) = (n_{p,z}^2 - n_{p,x}^2)\sigma_z + 2n_z n_x \sigma_x$$

$$[\sigma_z, (\vec{n}_p \cdot \vec{\sigma})] = [\sigma_z, (n_{p,x}\sigma_x + n_{p,z}\sigma_z)] = n_{p,x}[\sigma_z, \sigma_x] = 2i n_{p,x}\sigma_y$$

Similarly, we can get $S_x(t)$ and $S_y(t)$ in Schödinger picture

$$\langle S_y(t) \rangle = \frac{1}{2^n} \sum_p [S_y U_p(t) S_z U_p(t)^\dagger] = \frac{1}{2^n} \sum_p y_p(t) \quad (\text{B.61})$$

$$\langle S_x(t) \rangle = \frac{1}{2^n} \sum_p [S_x U_p(t) S_z U_p(t)^\dagger] = \frac{1}{2^n} \sum_p x_p(t) \quad (\text{B.62})$$

$$\begin{aligned} y_p(t) &= \text{Tr} [S_y U_p(t) S_z U_p(t)^\dagger] \\ &= \frac{1}{4} \text{Tr} \{ \sigma_y ([\cos^2(\omega_p t)\sigma_z + \sin^2(\omega_p t)((n_{p,z}^2 - n_{p,x}^2)\sigma_z + 2n_z n_x \sigma_x]) - 2n_{p,x} \sin(\omega_p t) \cos(\omega_p t) \sigma_y \} \\ &= -n_{p,x} \sin(\omega_p t) \cos(\omega_p t) \end{aligned} \quad (\text{B.63})$$

$$\begin{aligned} x_p(t) &= \text{Tr} [S_x U_p(t) S_z U_p(t)^\dagger] \\ &= \frac{1}{4} \text{Tr} \{ \sigma_x ([\cos^2(\omega_p t)\sigma_z + \sin^2(\omega_p t)((n_{p,z}^2 - n_{p,x}^2)\sigma_z + 2n_z n_x \sigma_x]) - 2n_{p,x} \sin(\omega_p t) \cos(\omega_p t) \sigma_y \} \\ &= n_z n_x \sin^2(\omega_p t) \end{aligned} \quad (\text{B.64})$$

If we replace ω_p with $\Omega_p = \sqrt{h^2 + \beta_p^2}$, the formula can be rewrite as

$$\begin{aligned} f_z^{(p)}(t) &= +\frac{1}{2} [n_{p,z}^2 + n_{p,x}^2 \cos(\Omega_p t)] \\ f_y^{(p)}(t) &= -\frac{1}{2} n_{p,x} \sin(\Omega_p t) \\ f_x^{(p)}(t) &= +\frac{1}{2} [n_{p,x} n_{p,z} - n_{p,x} n_{p,z} \cos(\Omega_p t)] \end{aligned} \quad (\text{B.65})$$

Of course we can verify that

$$(f_x^{(p)})^2 + (f_y^{(p)})^2 + (f_z^{(p)})^2 = \frac{1}{4} [\sin^2(\omega) (n_{p,x}^2 + n_{p,z}^2) + \cos^2(\omega)]^2 = \frac{1}{4}, \quad (\text{B.66})$$

given that $n_{p,z}^2 + n_{p,x}^2 = 1$. Thus the angular momentum is normalized since the spin number is 1/2.

B.13 Weak Driving

In practical experiments, strong field is hard to achieve. Thus the approximation of strong rabi driving is no longer valid. For weak driving, we can start from the exact formula B.65. With the symbol integral of Mathematica, we can get a more rigirous result.

$$\langle S_z(t) \rangle = \int_{-\infty}^{\infty} z_p(t; \beta) P(\beta) d\beta = 1 + \frac{1}{b} \sqrt{\frac{\pi}{2}} h e^{\frac{h^2}{2b^2}} \text{Re} \left(e^{\frac{iht}{2}} \text{erfc} \left(\frac{\sqrt{h(h - ib^2 t)}}{\sqrt{2b}} \right) + \text{erf} \left(\frac{h}{\sqrt{2b}} \right) - 1 \right) \quad (\text{B.67})$$

$$\langle S_y(t) \rangle = \int_{-\infty}^{\infty} y_p(t; \beta) P(\beta) d\beta = \text{Im} \frac{e^{iht} (2h^2 + b^2(-1 - 2iht))}{2\sqrt{h} (h - ib^2 t)^{3/2}} \quad (\text{B.68})$$

For an ensemble averaged rabi driving, the situation in weak driving is quite similar. We can get a sloppy approximation assuming that

$$\langle S_i(\beta, t) \rangle = S_i(\langle \beta \rangle, t)$$

Then

$$\langle S_z(t) \rangle = \frac{1}{2}[n_{p,z}^2 + n_{p,x}^2 \operatorname{Re}\{F(t)\}] \quad (\text{B.69})$$

$$\langle S_y(t) \rangle = \frac{1}{2}n_{p,x} \operatorname{Im}\{-F(t)\} \quad (\text{B.70})$$

$$\langle S_x(t) \rangle = \frac{1}{2}n_{p,x}n_{p,z}[1 - \operatorname{Re}\{F(t)\}] \quad (\text{B.71})$$

The final result can be given using Mathematica.

$$\langle S_z(t) \rangle = \int_{-\infty}^{\infty} z_p(t; \beta) P(\beta) d\beta = \quad (\text{B.72})$$

$$\frac{\Gamma}{\Gamma+h} + \frac{\Gamma+h}{h-\Gamma} \operatorname{Re} h e^{\frac{i\hbar t}{2}} \left(-\Gamma(1+i) \operatorname{erfi} \left(\frac{1+i}{2} \sqrt{\hbar t} \right) + h e^{it(h^2-\Gamma^2)/2h} \left(1 + i \operatorname{erfi} \left(\frac{1+i}{2} \Gamma \sqrt{\frac{t}{h}} \right) \right) \right) \quad (\text{B.73})$$

$$\langle S_y(t) \rangle = \int_{-\infty}^{\infty} y_p(t; \beta) P(\beta) d\beta = \quad (\text{B.74})$$

$$\frac{e^{i\hbar t}}{2\sqrt{\pi}h^2} \left(\sqrt{\pi} (\Gamma^2 + 2h^2) e^{-\frac{i\Gamma^2 t}{2h}} \left(1 + i \operatorname{erfi} \left(\left(\frac{1}{2} + \frac{i}{2} \right) \Gamma \sqrt{\frac{t}{h}} \right) \right) + (-1-i) \Gamma \sqrt{\frac{h}{t}} \right) \quad (\text{B.75})$$

$$\langle S_x(t) \rangle = \int_{-\infty}^{\infty} x_p(t; \beta) P(\beta) d\beta = 0 \quad (\text{B.76})$$

B.14 State Fidelity

Assume the target unitary of the pulse is U , and the system start from some pure state $\rho_0 = |\psi_0\rangle\langle\psi_0|$. The noisy quantum process \mathcal{E} evolves the system into a mixed state $\mathcal{E}(\rho_0)$, and we can use state fidelity to compare it with the desired state $U\rho_0U^\dagger$. The state fidelity is

$$F(\rho, \sigma) = \left(\operatorname{tr} \sqrt{\sqrt{\rho}\sigma\sqrt{\rho}} \right)^2 \quad (\text{B.77})$$

in which ρ, σ are density matrices. Let $\rho = U\rho_0U^\dagger$ and $\sigma = \mathcal{E}(\rho_0)$. Denote that $U|\psi_0\rangle = |\psi\rangle$, we can find that $\sqrt{\rho} = \sqrt{|\psi\rangle\langle\psi|} = |\psi\rangle\langle\psi|$ due to the fact that $|\psi\rangle\langle\psi| |\psi\rangle\langle\psi| = |\psi\rangle\langle\psi|$. Hence

$$F(\rho, \sigma) = \left(\operatorname{tr} \sqrt{|\psi\rangle\langle\psi| \sigma |\psi\rangle\langle\psi|} \right)^2 = \langle \psi | \sigma | \psi \rangle \quad (\text{B.78})$$

The transformation can be derived from

$$F(\rho, \sigma) = \left(\operatorname{tr} \sqrt{|\psi\rangle\langle\psi|} f \langle\psi| \right)^2 = \left(\operatorname{tr} \sqrt{f} \sqrt{|\psi\rangle\langle\psi|} \right)^2 = \left(\sqrt{f} \operatorname{tr} |\psi\rangle\langle\psi| \right)^2 = f$$

since the projection of the σ on another state $|\psi\rangle$ is just a number $f = \langle \psi | \sigma | \psi \rangle \in \mathbb{R}$.

Substitute into the formula of quantum operation

$$\begin{aligned} F &= \langle \psi | \sigma | \psi \rangle = \langle \psi_0 | U^\dagger \mathcal{E}(|\psi_0\rangle\langle\psi_0|) U | \psi_0 \rangle \\ &= \sum_{k=0}^{2^n-1} \langle \psi_0 | U^\dagger E_k |\psi_0\rangle\langle\psi_0| E_k^\dagger U | \psi_0 \rangle \\ &= \sum_{k=0}^{2^n-1} c_k |\langle \psi_0 | U^\dagger U_k | \psi_0 \rangle|^2 \end{aligned} \quad (\text{B.79})$$

Use the expression of $E_k = \sqrt{c_k}U_k$ and

$$U_k = \cos\left(\frac{\Omega_k t}{2}\right) - i \sin\left(\frac{\Omega_k t}{2}\right)(\vec{n}_k \cdot \vec{\sigma}) \quad (\text{B.80})$$

Assume we want a pi pulse on X axis, then $U = R_x(\pi) = e^{-i\pi\sigma_x/2} = -i\sigma_x$. The formula can be further simplified for a single quantum gate.

$$\langle \psi_0 | U^\dagger U_k | \psi_0 \rangle = -i \cos\left(\frac{\Omega_k t}{2}\right) \langle \psi_0 | \sigma_x | \psi_0 \rangle - \sin\left(\frac{\Omega_k t}{2}\right) \langle \psi_0 | (\vec{n}_k \cdot \vec{\sigma}) \sigma_x | \psi_0 \rangle \quad (\text{B.81})$$

B.15 Average Gate Fidelity

For any single qubit pure state on the Bloch sphere, it has a form

$$|\psi_0\rangle = \cos(\theta/2) |0\rangle + e^{i\phi} \sin(\theta/2) |1\rangle, \quad (\text{B.82})$$

thus

$$\langle \psi_0 | \sigma_x | \psi_0 \rangle = \sin(\theta) \cos(\phi) \quad (\text{B.83})$$

$$\langle \psi_0 | (\vec{n}_k \cdot \vec{\sigma}) \sigma_x | \psi_0 \rangle = \langle \psi_0 | n_{kx} + n_{kz} \sigma_z \sigma_x | \psi_0 \rangle = n_{kx} + i \sin(\theta) \sin(\phi) n_{kz} \quad (\text{B.84})$$

substitute it into the formula

$$\langle \psi_0 | U^\dagger U_k | \psi_0 \rangle = -i \cos\left(\frac{\Omega_k t}{2}\right) \sin(\theta) \cos(\phi) - \sin\left(\frac{\Omega_k t}{2}\right) [n_{kx} + i \sin(\theta) \sin(\phi) n_{kz}] \quad (\text{B.85})$$

then

$$\begin{aligned} |\langle \psi_0 | U^\dagger U_k | \psi_0 \rangle|^2 &= \sin^2\left(\frac{\Omega_k t}{2}\right) n_{kx}^2 + \sin^2(\theta) \left[\sin\left(\frac{\Omega_k t}{2}\right) \sin(\phi) n_{kz} + \cos\left(\frac{\Omega_k t}{2}\right) \cos(\phi) \right]^2 \\ &= \sin^2\left(\frac{\Omega_k t}{2}\right) [n_{kx}^2 + n_{kz}^2 \sin^2(\theta) \sin^2(\phi)] + \cos^2\left(\frac{\Omega_k t}{2}\right) \sin^2(\theta) \cos^2(\phi) + \\ &\quad 2 \sin\left(\frac{\Omega_k t}{2}\right) \cos\left(\frac{\Omega_k t}{2}\right) \sin^2(\theta) \sin(\phi) \cos(\phi) n_{kz} \end{aligned} \quad (\text{B.86})$$

The average gate fidelity is defined as an ensemble average over all possible initial states

$$\bar{F}(\mathcal{E}, U) = \int F(\mathcal{E}, U, |\psi\rangle) d\psi = \int d\psi \langle \psi | U^\dagger \mathcal{E}(\psi) U | \psi \rangle \quad (\text{B.87})$$

in which

$$\int d\psi = \frac{1}{4\pi} \int_0^\pi \sin\theta d\theta \int_0^{2\pi} d\phi = 1 \quad (\text{B.88})$$

If we use $\langle \dots \rangle_\psi$ to denote the average over the sphere surface $\int d\psi$, then the average of these coefficients are

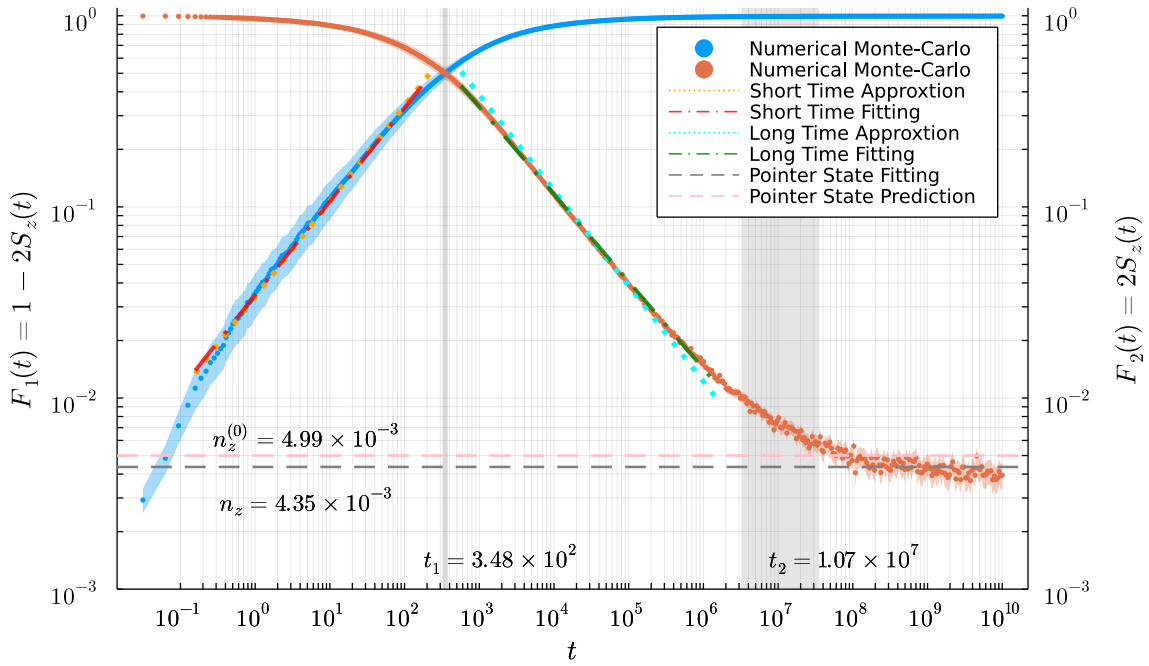
$$\langle \sin^2(\theta) \cos^2(\phi) \rangle_\psi = \langle \sin^2(\theta) \sin^2(\phi) \rangle_\psi = \frac{1}{3}, \quad \langle \sin^2(\theta) \sin(\phi) \cos(\phi) \rangle_\psi = 0 \quad (\text{B.89})$$

Substitute the result into average fidelity

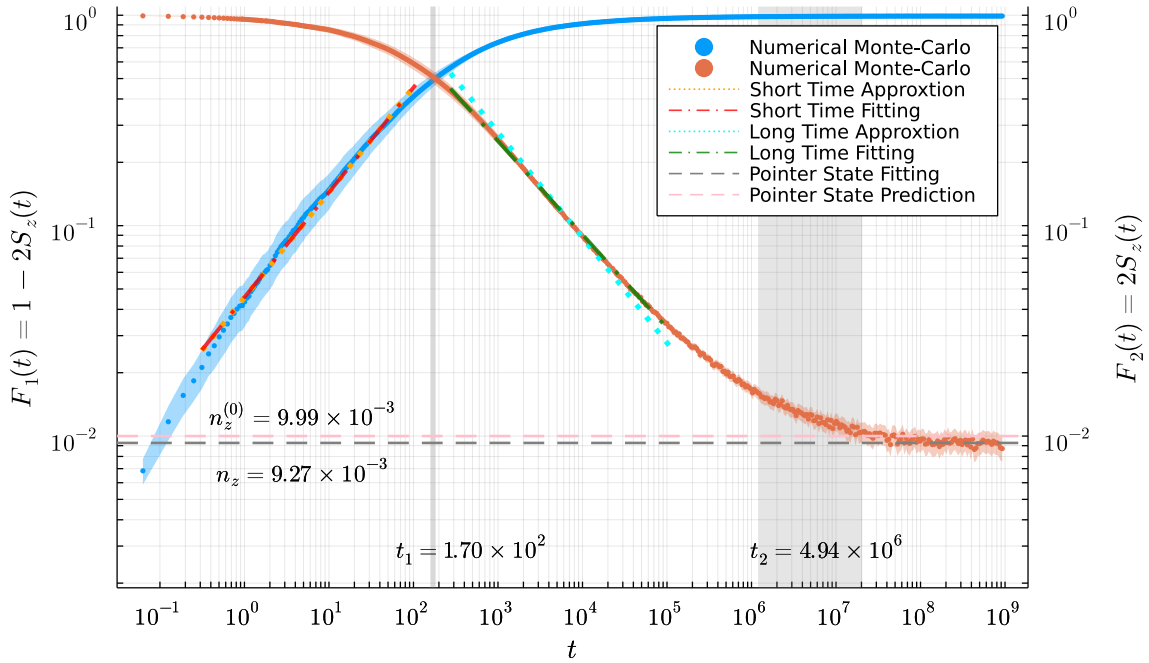
$$\begin{aligned} \bar{F}(\mathcal{E}, U) &= \sum_{k=0}^{2^n-1} c_k \left\{ \frac{1}{3} \cos^2\left(\frac{\Omega_k t}{2}\right) + \sin^2\left(\frac{\Omega_k t}{2}\right) \left[n_{kx}^2 + \frac{n_{kz}^2}{3} \right] \right\} \\ &= \sum_{k=0}^{2^n-1} c_k \left\{ \frac{1}{3} + \frac{2}{3} n_{kx}^2 \sin^2\left(\frac{\Omega_k t}{2}\right) \right\} \end{aligned} \quad (\text{B.90})$$

Appendix C

Supplementary Figures

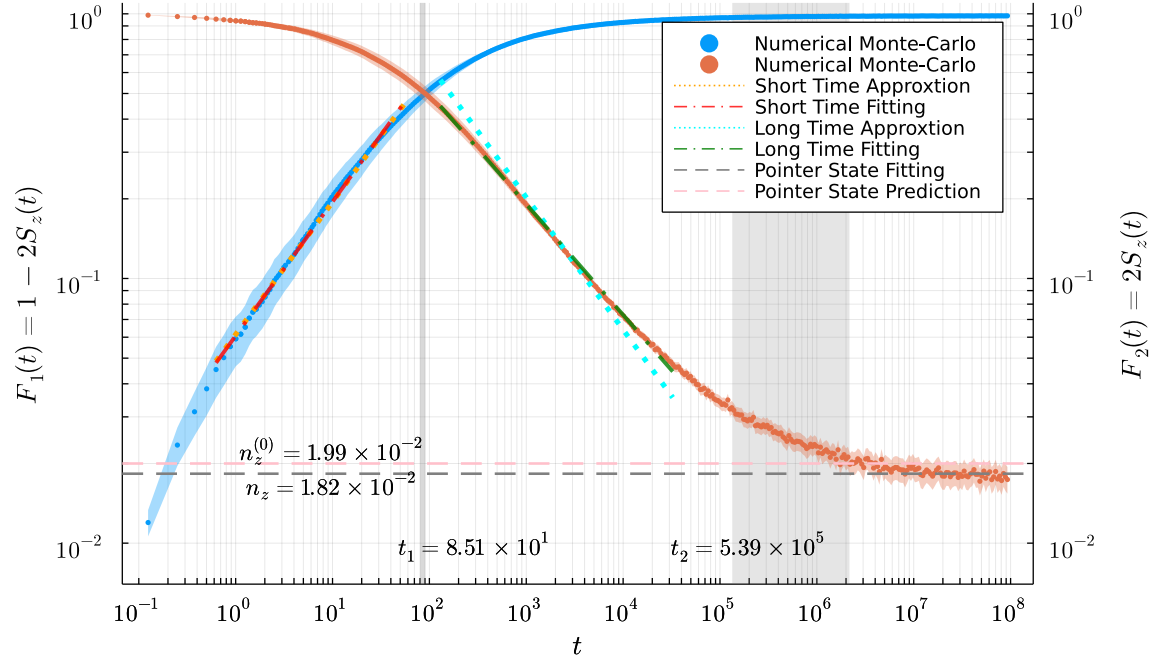


(a) **3D, $h=200$** . Rabi envelope is obtained at $M' = 10000$, $N' = 500$. The short time fitting result is $k = 0.4906$, $b = -1.4622$. The long time fitting result is $k = -0.4566$, $b = 0.8929$.

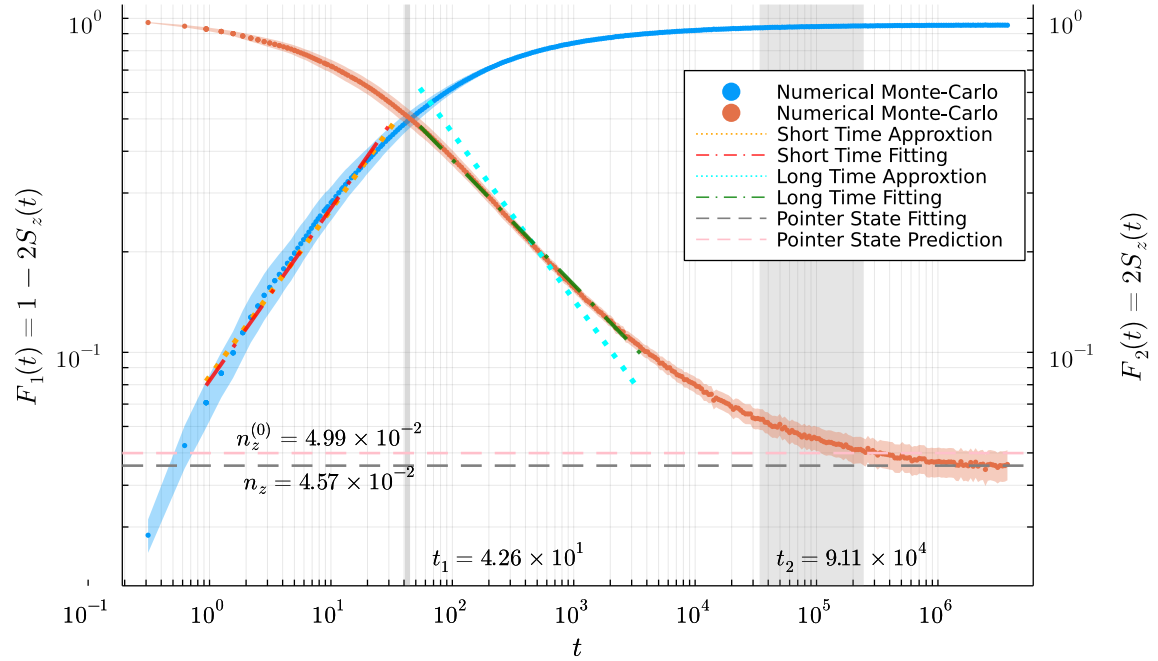


(b) **3D, $h=100$** . Rabi envelope is obtained at $M' = 10000$, $N' = 500$. The short time fitting result is $k = 0.4984$, $b = -1.3401$. The long time fitting result is $k = -0.4442$, $b = 0.7345$.

Figure C.1: 3D ensemble averaged Rabi oscillation envelope in log scale.

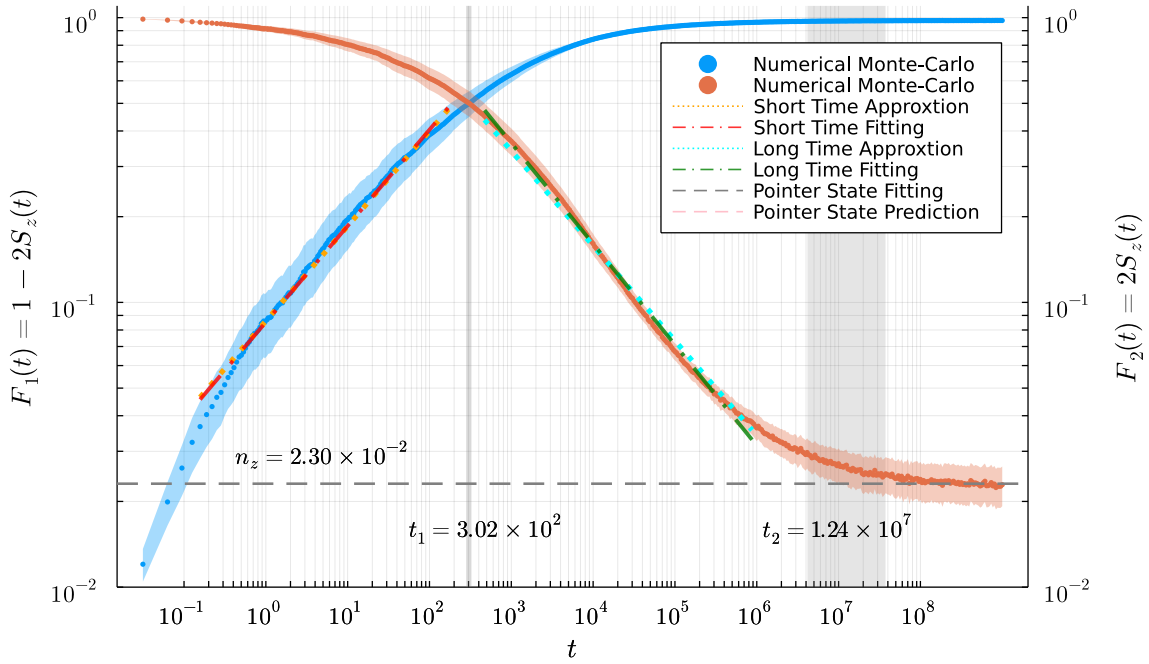


(a) **3D, $h=50$** . Rabi envelope is obtained at $M' = 4000$, $N' = 500$. The short time fitting result is $k = 0.5061$, $b = -1.2163$. The long time fitting result is $k = -0.4182$, $b = 0.5351$.

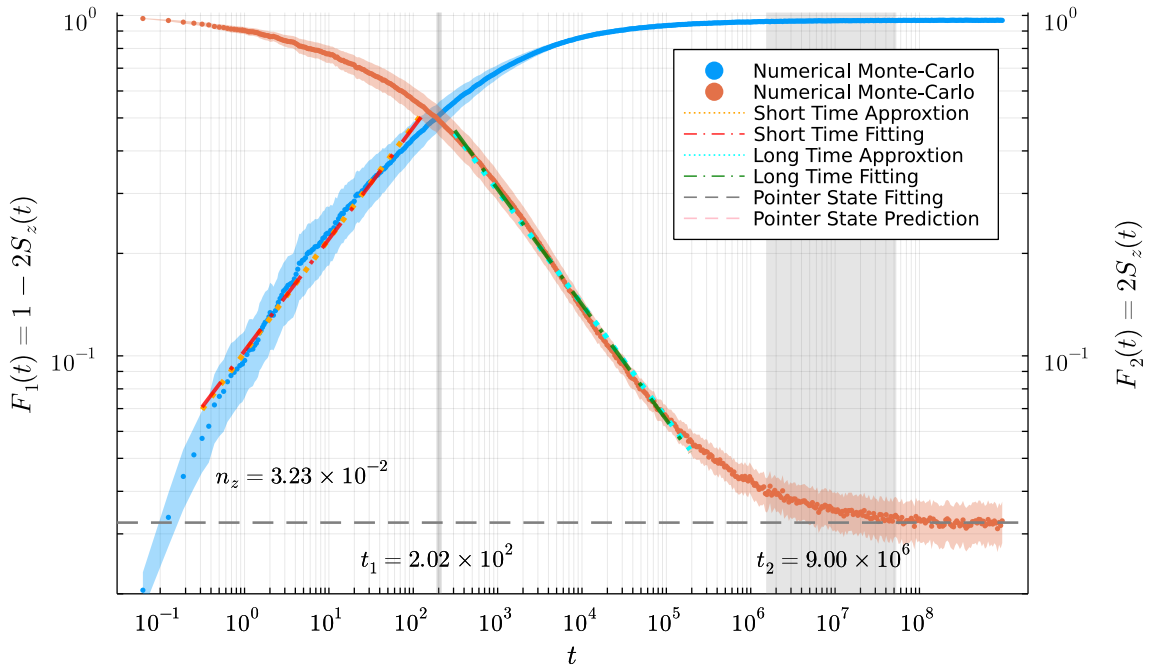


(b) **3D, $h=20$** . Rabi envelope is obtained at $M' = 4000$, $N' = 500$. The short time fitting result is $k = 0.5165$, $b = -1.0849$. The long time fitting result is $k = -0.3744$, $b = 0.3257$.

Figure C.2: 3D ensemble averaged Rabi oscillation envelope in log scale.

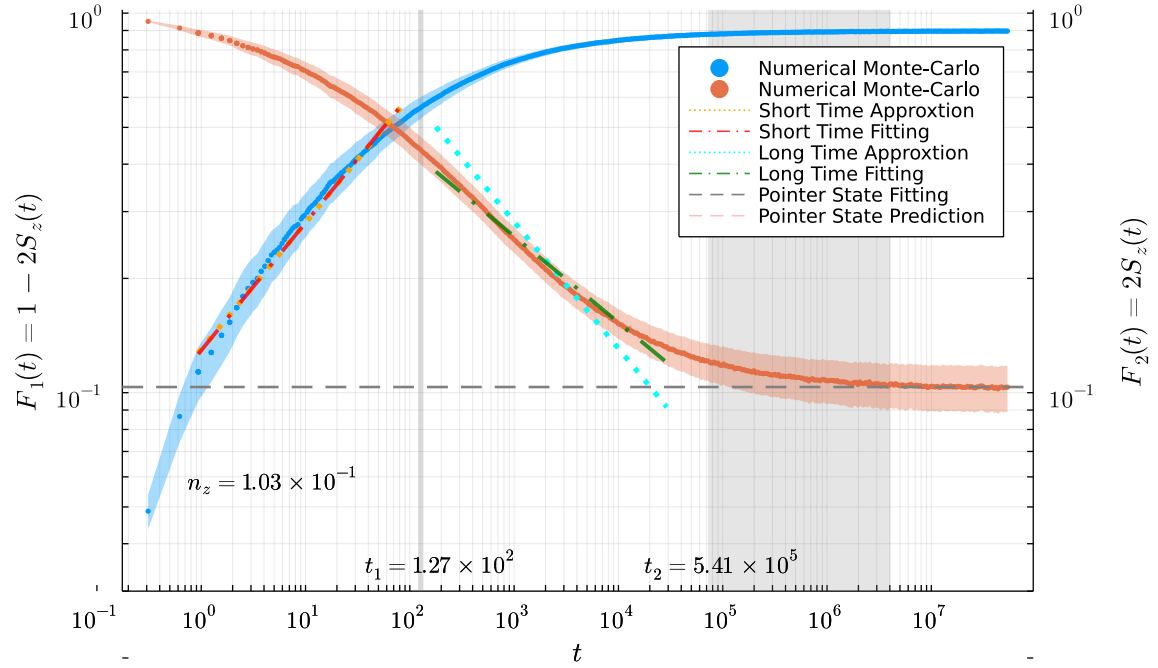


(a) **2D, $h=200$** . Rabi envelope is obtained at $M' = 10000$, $N' = 500$. The short time fitting result is $k = 0.3379, b = -1.0694$. The long time fitting result is $k = -0.354, b = 0.6214$.

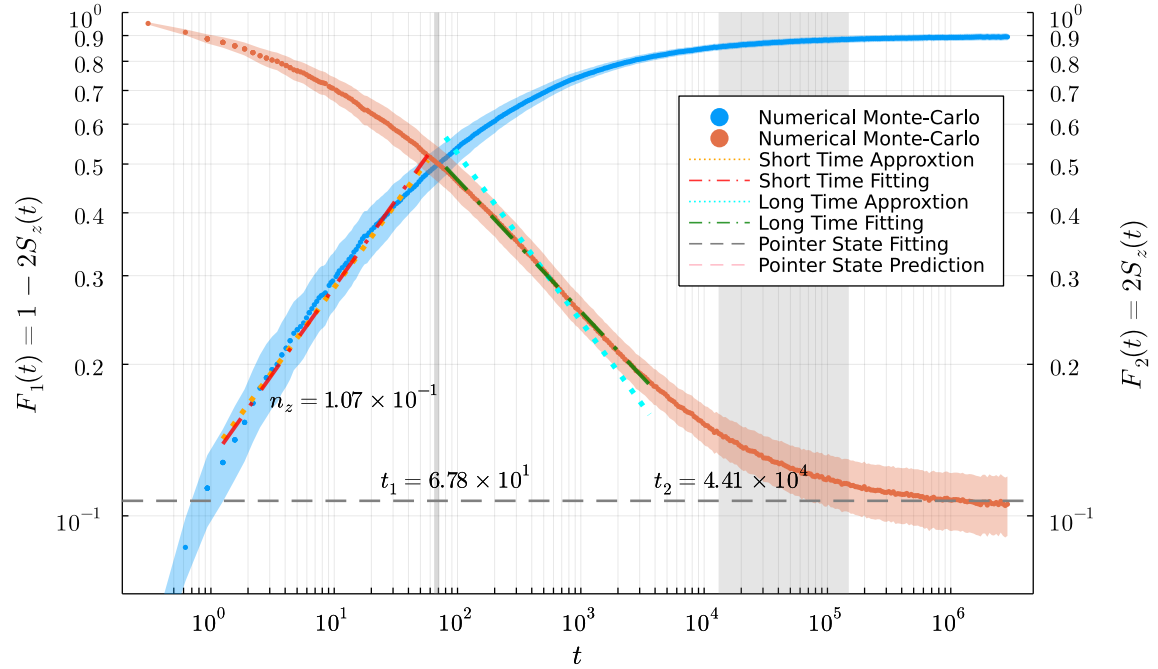


(b) **2D, $h=100$** . Rabi envelope is obtained at $M' = 10000$, $N' = 500$. The short time fitting result is $k = 0.3281, b = -0.9852$. The long time fitting result is $k = -0.339, b = 0.5069$.

Figure C.3: 2D ensemble averaged Rabi oscillation envelope in log scale.

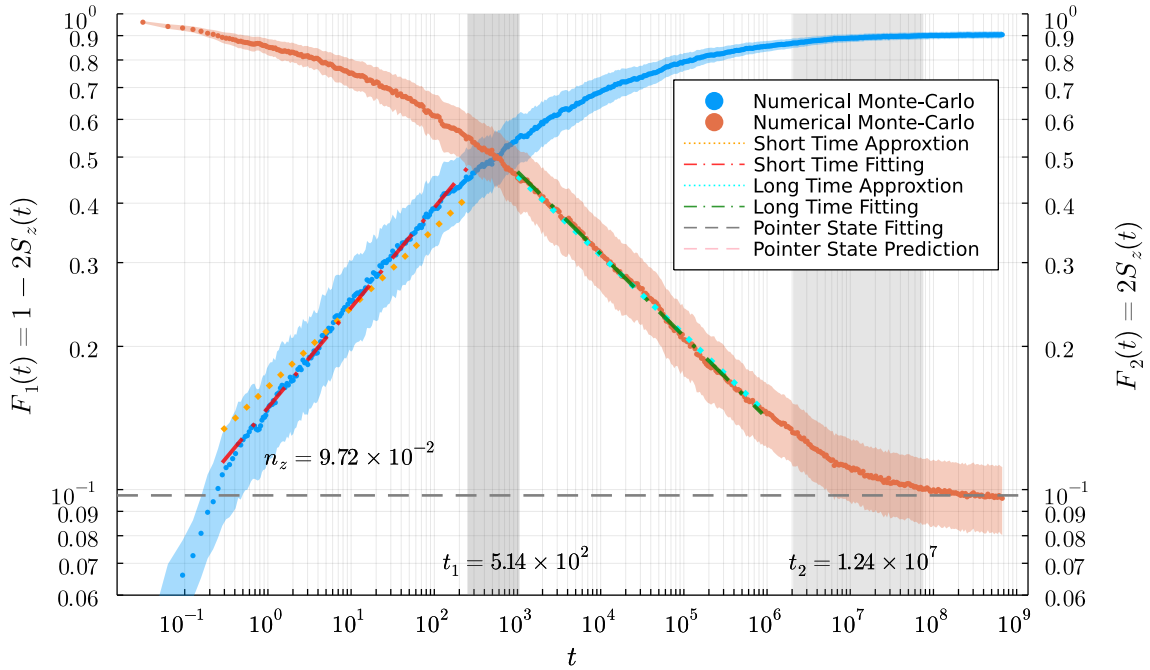


(a) **2D, $h=50$** . Rabi envelope is obtained at $M' = 2500$, $N' = 500$. The short time fitting result is $k = 0.3357$, $b = -0.9353$. The long time fitting result is $k = -0.2909$, $b = 0.3089$.

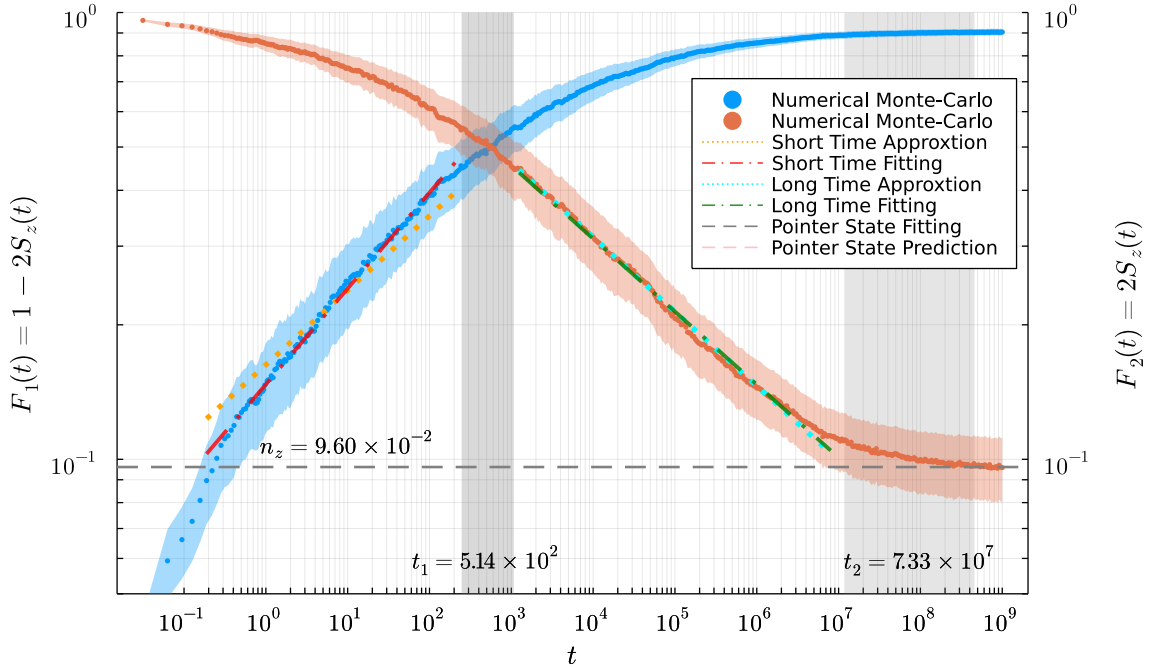


(b) **2D, $h=20$** . Rabi envelope is obtained at $M' = 4000$, $N' = 500$. The short time fitting result is $k = 0.3453$, $b = -0.8906$. The long time fitting result is $k = -0.2613$, $b = 0.1902$.

Figure C.4: 2D ensemble averaged Rabi oscillation envelope in log scale.

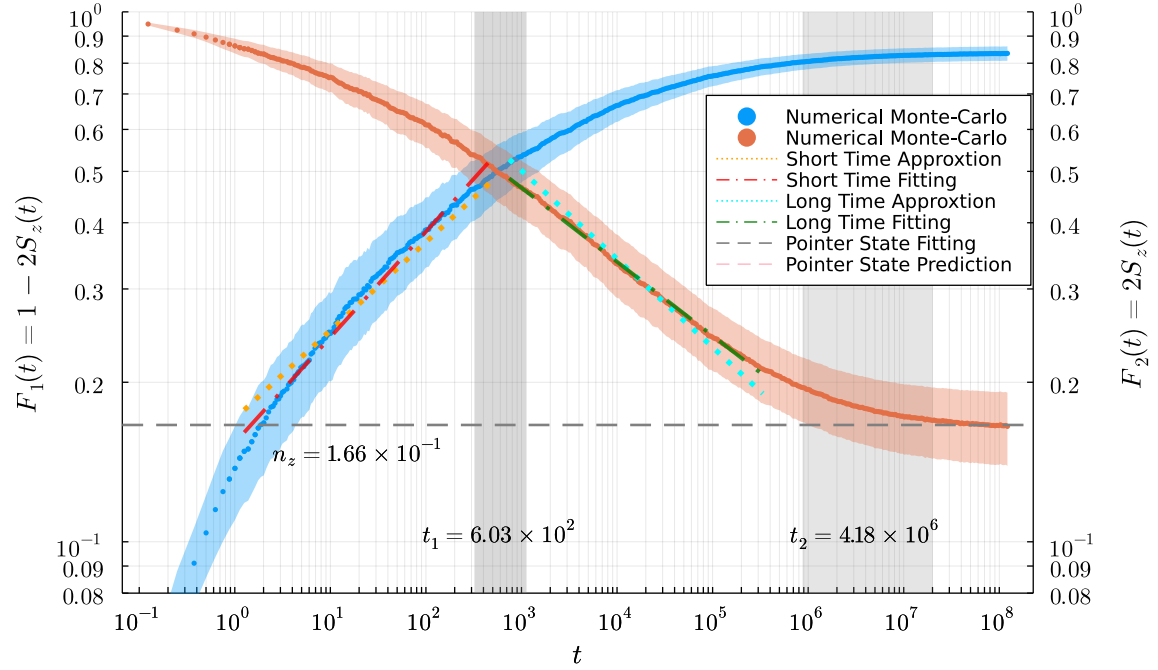


(a) **1D, $h=200$** . Rabi envelope is obtained at $M' = 3000$, $N' = 600$. The short time fitting result is $k = 0.2103$, $b = -0.828$. The long time fitting result is $k = -0.1729$, $b = 0.1869$.

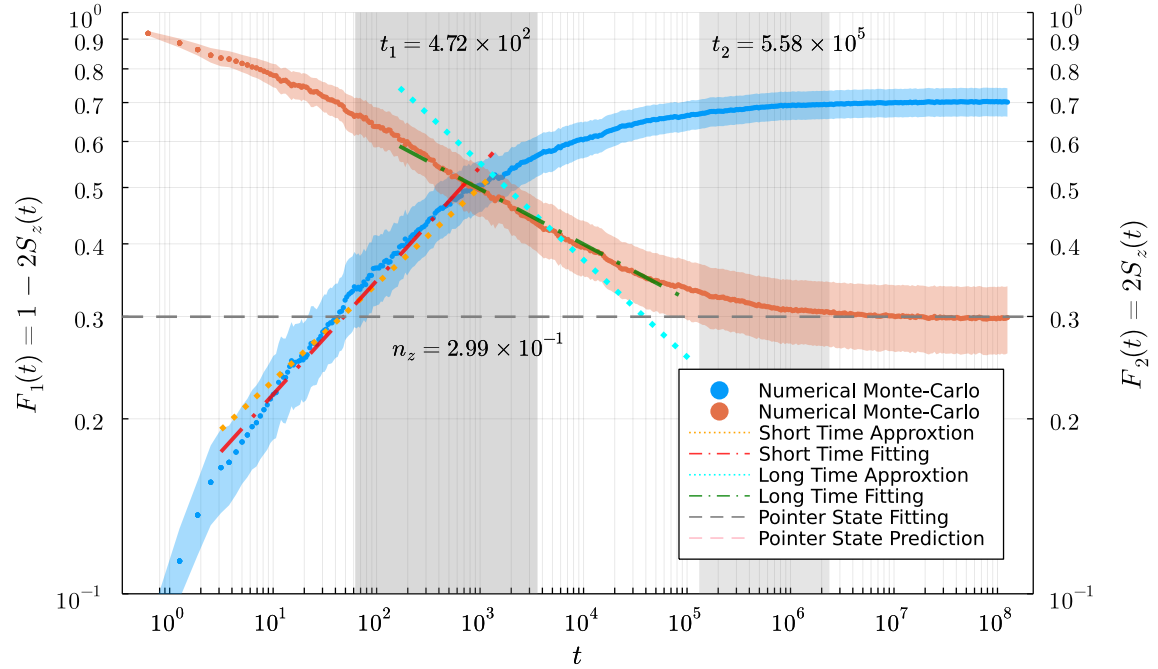


(b) **1D, $h=100$** . Rabi envelope is obtained at $M' = 3000$, $N' = 600$. The short time fitting result is $k = 0.2146$, $b = -0.8323$. The long time fitting result is $k = -0.1633$, $b = 0.1473$.

Figure C.5: 1D ensemble averaged Rabi oscillation envelope in log scale.



(a) **1D, $h=50$** . Rabi envelope is obtained at $M' = 10000$, $N' = 500$. The short time fitting result is $k = 0.1992$, $b = -0.8132$. The long time fitting result is $k = -0.1396$, $b = 0.0867$.



(b) **1D, $h=20$** . Rabi envelope is obtained at $M' = 4000$, $N' = 500$. The short time fitting result is $k = 0.1957$, $b = -0.8527$. The long time fitting result is $k = -0.0948$, $b = -0.0193$.

Figure C.6: 1D ensemble averaged Rabi oscillation envelope in log scale.

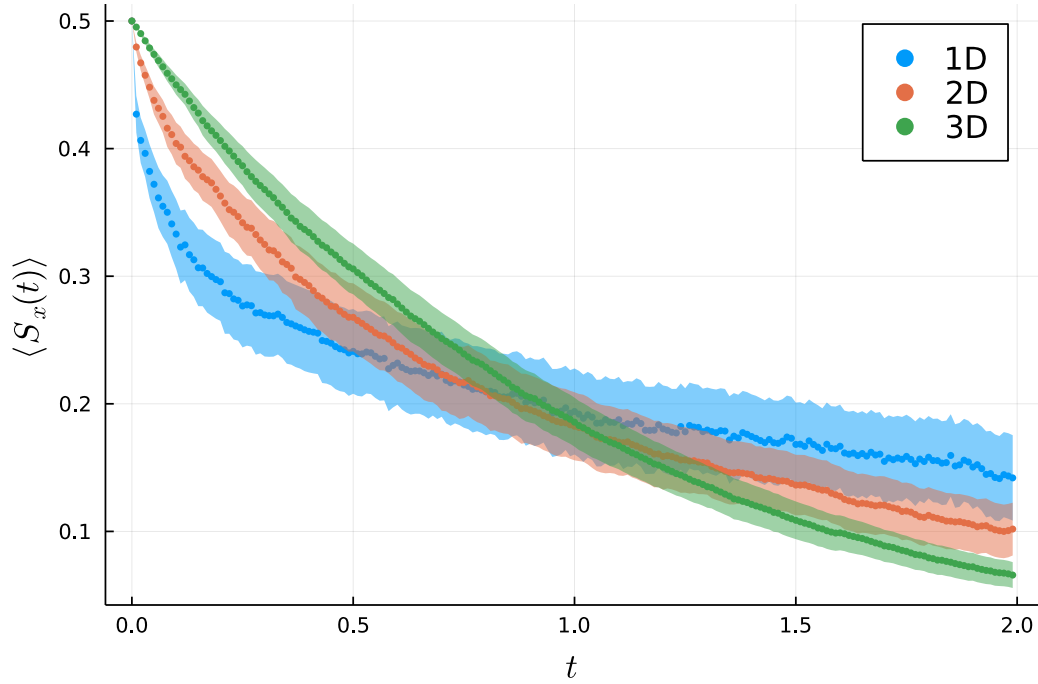


Figure C.7: Ensemble averaged T_2 relaxations with normalized coherence time.

The relaxation curves are evaluated by Monte-Carlo sampling, with $M' = 4000$ disorder realizations (DRs) and $N' = 1000$ spin configurations.

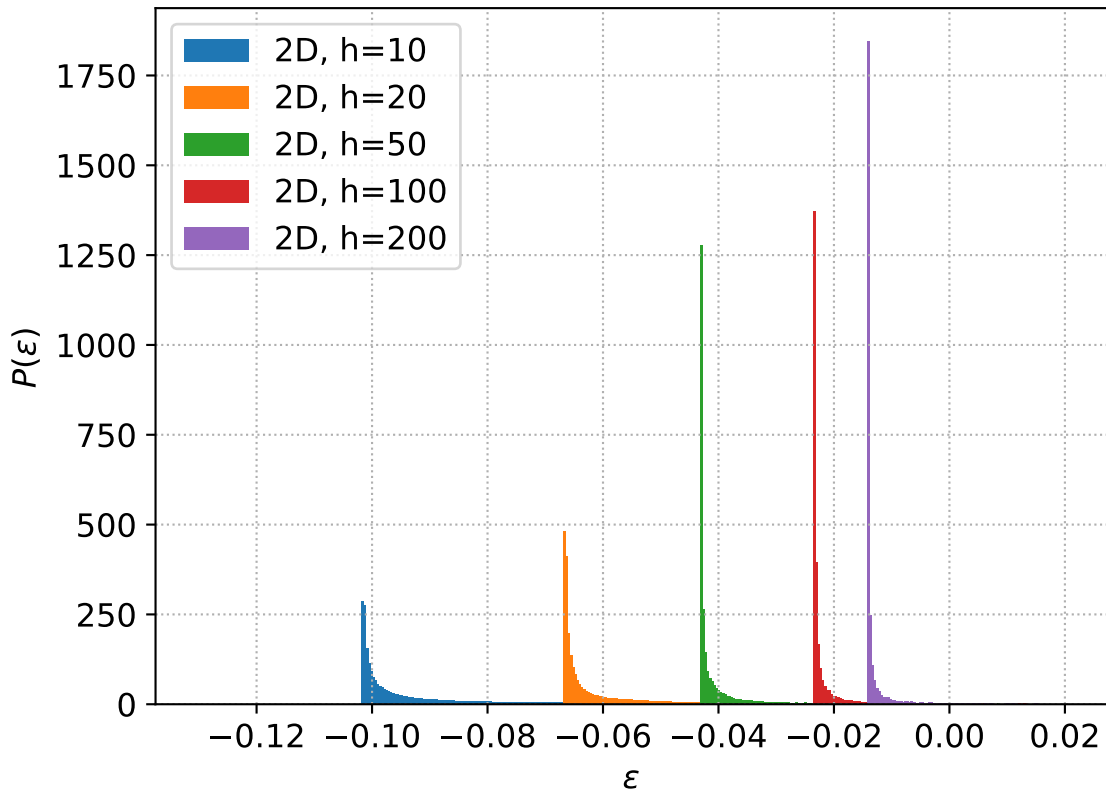


Figure C.8: Distribution of phase error ε under various driving strength in 2D spin ensemble

The error is sampled with $M' = 2000$ disorder realizations, and $N' = 400$. The histogram is obtained from -0.13 to 0.02 with 400 bins in total.

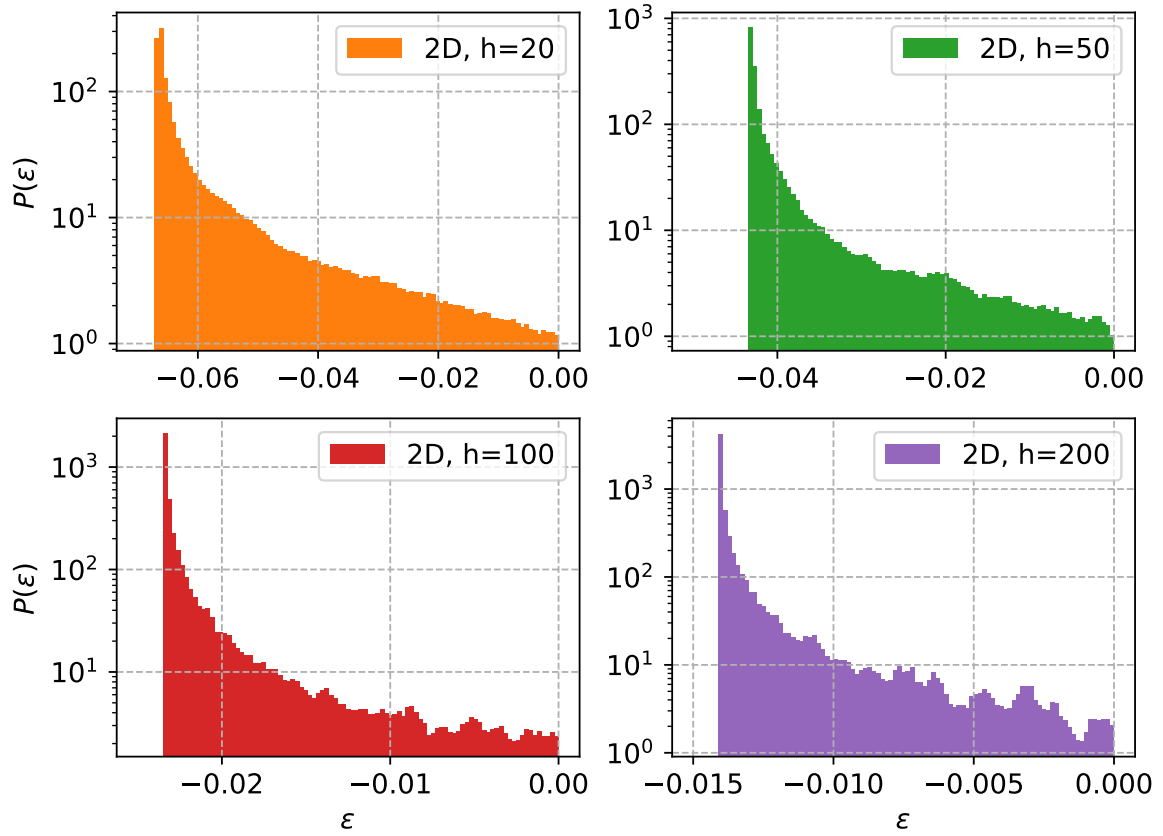


Figure C.9: Probability distribution function of ε in 2D ensemble

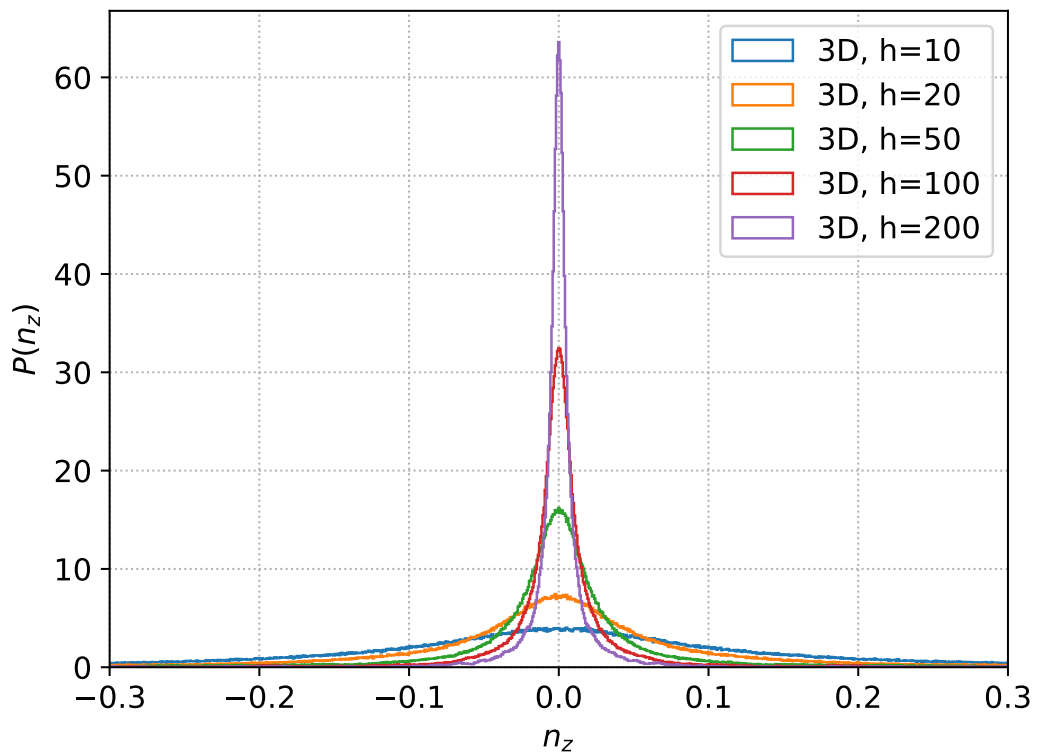


Figure C.10: Distribution of axis error of 3D ensemble under various driving strengths

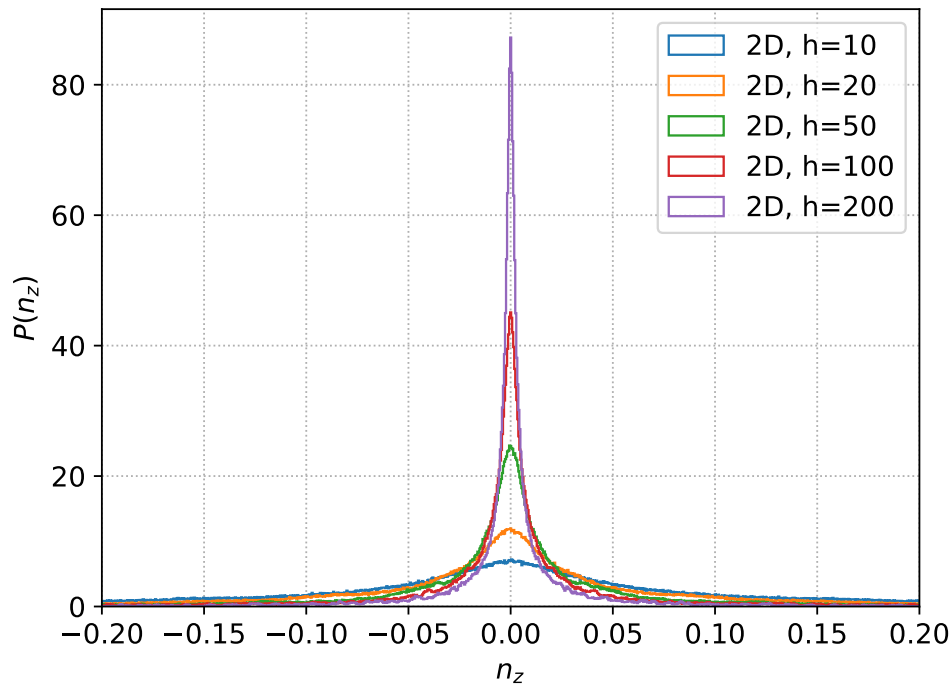


Figure C.11: Distribution of axis error of 2D ensemble under various driving strengths

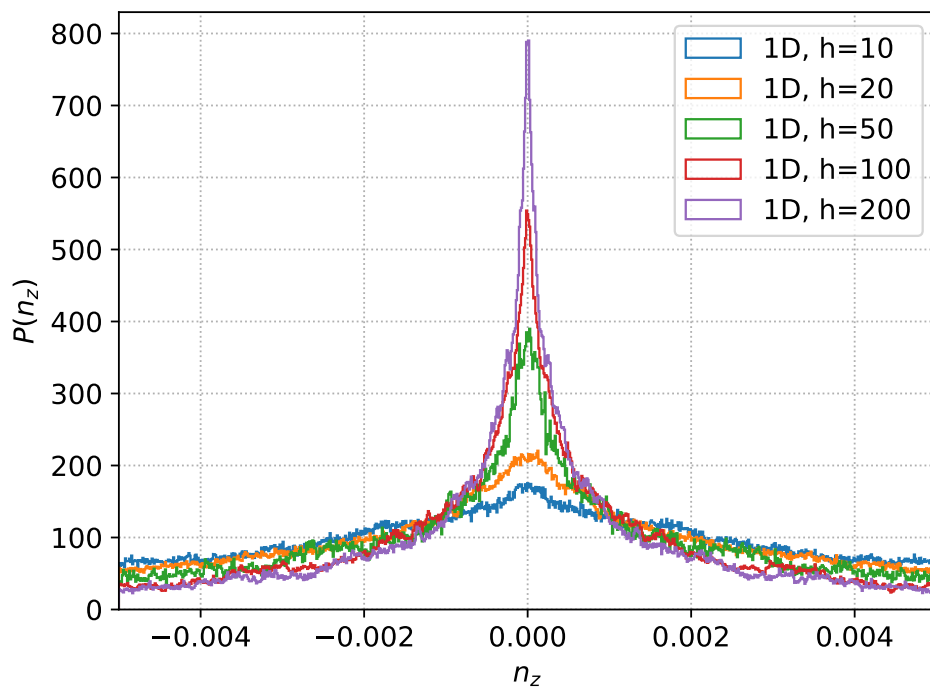


Figure C.12: Distribution of axis error of 1D ensemble under various driving strengths

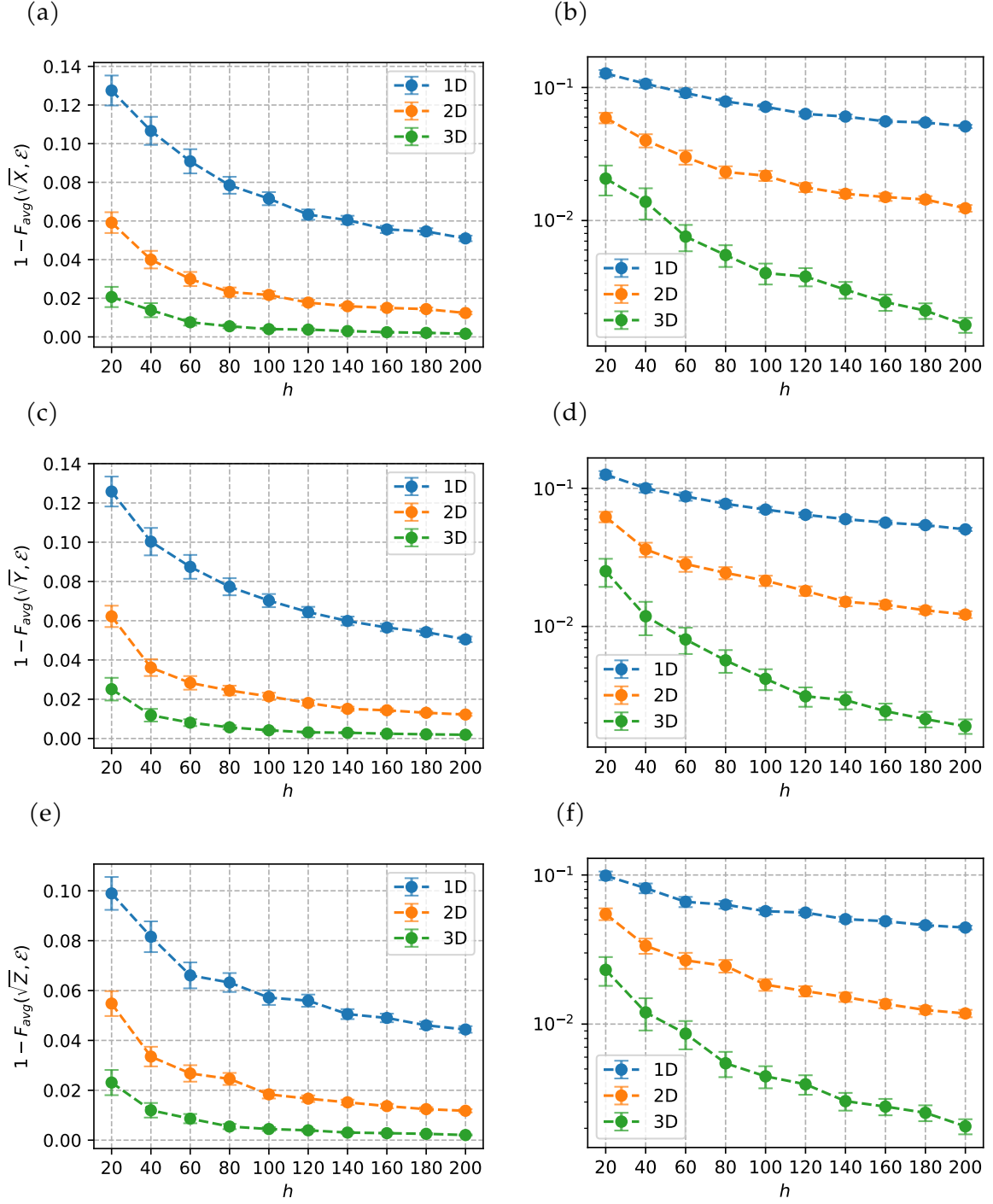


Figure C.13: Average Gate Fidelity of Single Qubit Gates

(a): \sqrt{X} gate infidelity, in normal scale. (b): \sqrt{Y} gate infidelity, in log scale. (c): \sqrt{Y} gate infidelity, in normal scale. (d): \sqrt{X} gate infidelity, in log scale. (e): \sqrt{Z} gate infidelity, in log scale. (f): \sqrt{Z} gate infidelity, in normal scale. The results is obtained from Monte-Carlo sampling with $M' = h^2$, $N' = 1000$. Two fold of the mean error is dispalyed to make the errorbar visible.

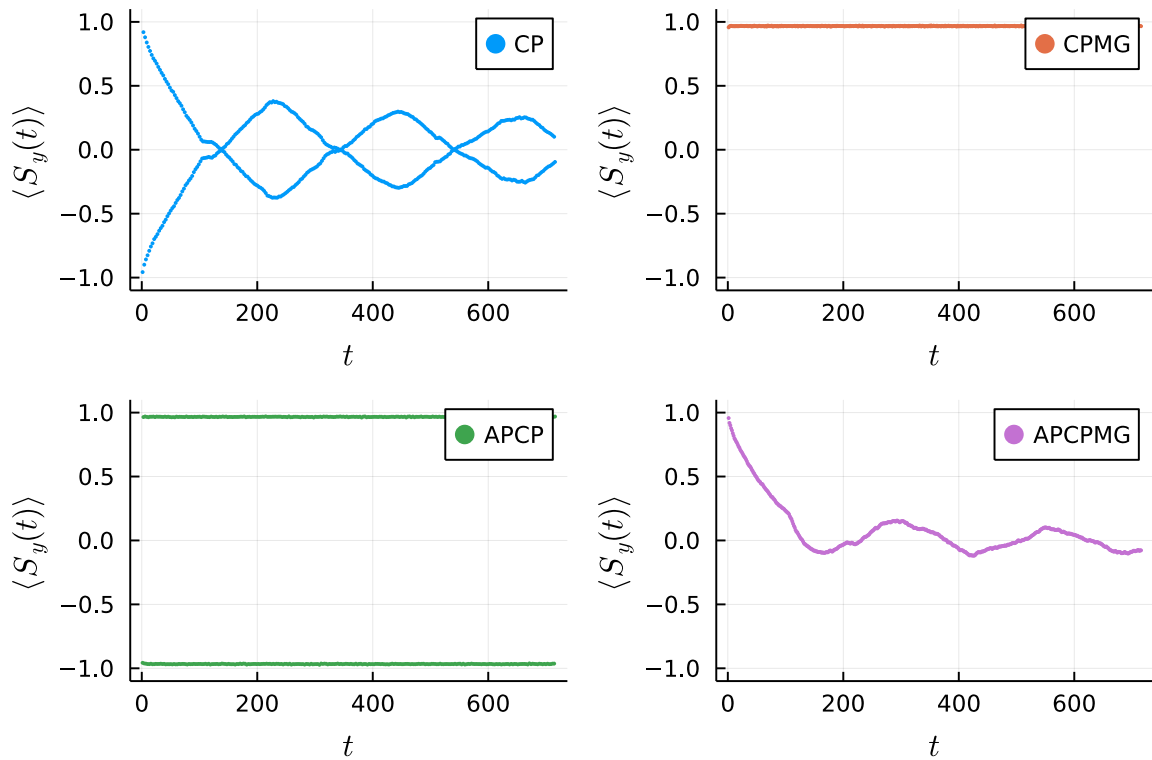


Figure C.14: Spin echos envelope of $S_y(t)$ under different decoupling sequences in 2D. Sequence parameters are set at $h = 100$ $\tau = 0.7$.

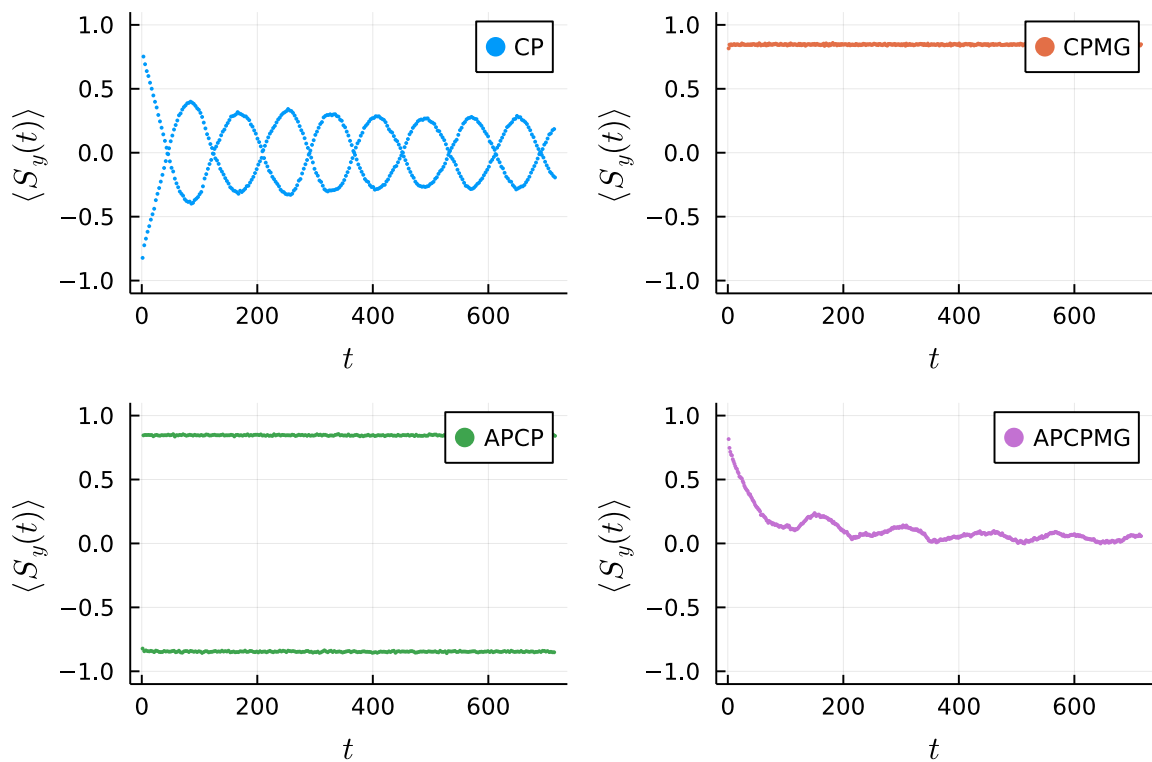


Figure C.15: Spin echos envelope of $S_y(t)$ under different decoupling sequences in 1D. Sequence parameters are set at $h = 100$ $\tau = 0.7$.

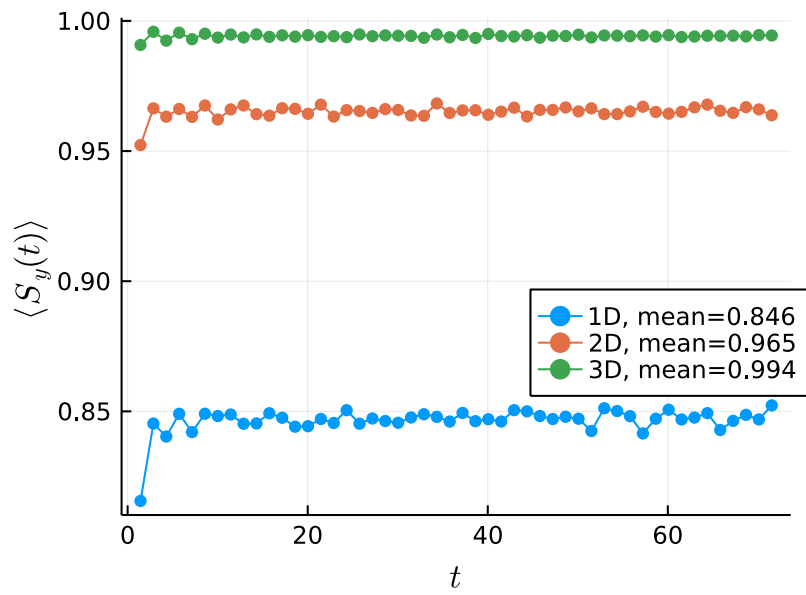


Figure C.16: Spin echos envelope of CPMG driving.

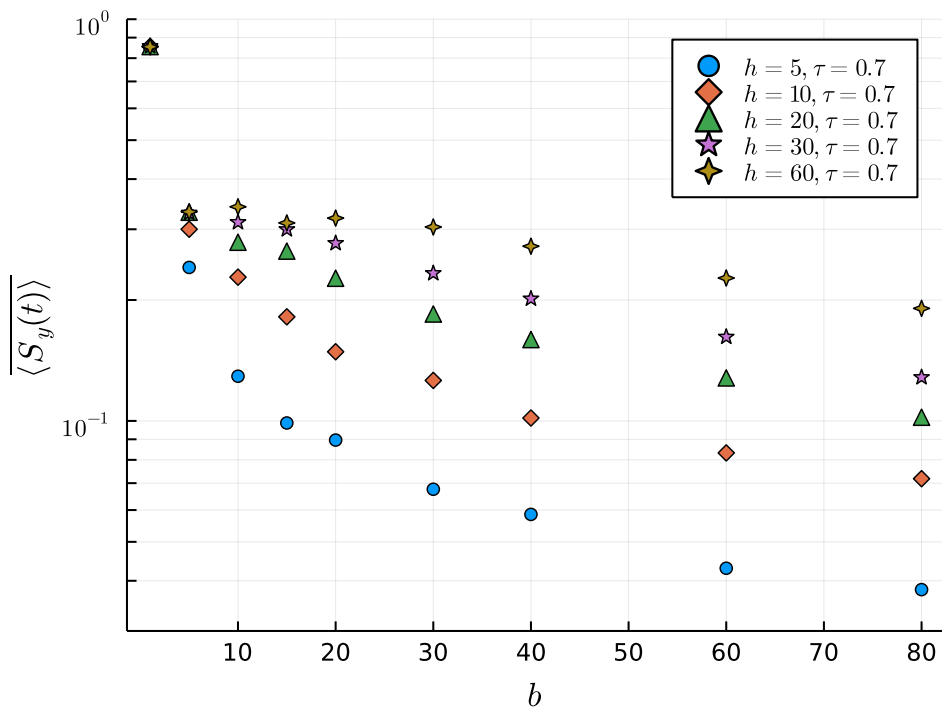


Figure C.17: Average height of signal under different driving strength h and noise linewidth b in a strong noise regime $b > h$.

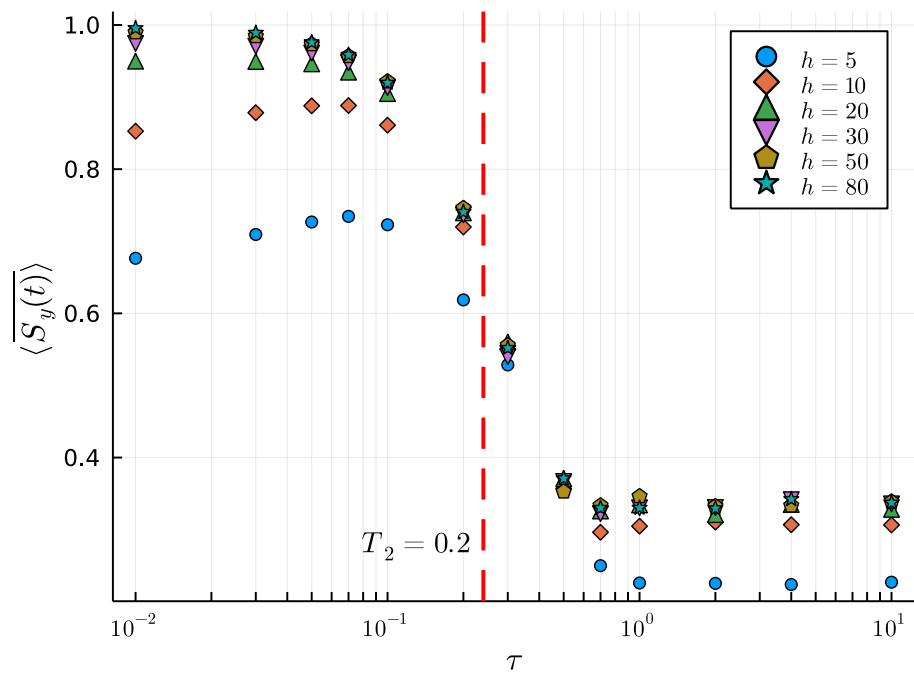


Figure C.18: Average height of spin echos under different driving strength h and noise linewidth τ . The noise linewidth is set at $b = 5$. The height of spin echos shows a sharp drop

Appendix D

Supplementary Table

	h	mean	std	skew	kurtosis
0	10.0	-0.000050	0.304136	0.004367	2.950771
1	20.0	0.000134	0.207064	0.007630	8.724538
2	50.0	-0.000087	0.135213	-0.045515	21.030015
3	100.0	0.000090	0.083268	0.118819	50.514382
4	200.0	-0.000068	0.062385	-0.171311	97.119852

Table D.1: Statistics of 3D axis error

	h	mean	std	skewness	kurtosis
0	10.0	-0.000107	0.401549	-0.002157	1.299047
1	20.0	0.000612	0.325054	0.010417	3.510374
2	50.0	0.000289	0.238899	0.010321	8.747155
3	100.0	0.000135	0.213003	0.014871	11.146226
4	200.0	-0.000180	0.152086	-0.014145	23.993511

Table D.2: Statistics of 2D axis error

	h	mean	std	skewness	kurtosis
0	10.0	0.492398	1.850346	4.529376	22.510094
1	20.0	0.371559	1.685833	5.446609	32.671633
2	50.0	0.167302	1.186249	8.134491	72.961305
3	100.0	0.115516	0.803774	9.989193	125.682360
4	200.0	0.078450	0.711548	11.800746	165.615432

Table D.3: Statistics of 2D phase error

	h	mean	std	skewness	kurtosis
0	10.0	-0.000086	0.586029	-0.000249	-0.468492
1	20.0	0.000127	0.516439	0.000454	0.207183
2	50.0	-0.001101	0.405957	-0.003737	1.865981
3	100.0	-0.000134	0.403200	0.000266	2.177632
4	200.0	0.000068	0.362904	0.000190	3.323167

Table D.4: Statistics of 1D axis error

	gate	dim	m	b	res	h for 1%	h for 0.1%
0	X	1D	-0.00442	-1.85307	0.04286044808385873	623.29754	1144.78890
1	X	2D	-0.00785	-2.62126	0.2684924689483453	252.81750	546.24472
2	X	3D	-0.01190	-3.67716	0.4056663311878712	77.99645	271.52251
3	Y	1D	-0.00467	-1.81795	0.07050728221281014	597.11007	1090.39576
4	Y	2D	-0.00749	-2.65271	0.12962917457792922	260.57625	567.88085
5	Y	3D	-0.01350	-3.44283	0.3613780183169373	86.08766	256.62715
6	Z	1D	-0.00372	-2.14028	0.043585379540038244	662.71113	1281.78419
7	Z	2D	-0.00739	-2.63020	0.17300598765223335	267.28720	578.91350
8	Z	3D	-0.01161	-3.27963	0.4745589251607463	114.19870	312.57188
9	sqrtX	1D	-0.00494	-2.07853	0.046403754024412526	511.57288	977.78061
10	sqrtX	2D	-0.00789	-2.94800	0.19043207744990137	210.12639	502.09096
11	sqrtX	3D	-0.01318	-3.92302	0.3227487317929805	51.74994	226.43084
12	sqrtY	1D	-0.00472	-2.11699	0.0424371802028181	527.57953	1015.80670
13	sqrtY	2D	-0.00811	-2.94794	0.20230260202375913	204.22538	487.98060
14	sqrtY	3D	-0.01320	-3.91178	0.5370930597289919	52.54561	227.03727
15	sqrtZ	1D	-0.00406	-2.37685	0.0495970598345798	548.63615	1115.55610
16	sqrtZ	2D	-0.00778	-3.04736	0.17868995610425392	200.21808	496.15891
17	sqrtZ	3D	-0.01216	-3.95653	0.4316827033630947	53.36189	242.78814

Table D.5: Fitting of pulse gate fidelities versus driving strength in log scale

Appendix E

Reproducibility: Data and Code

All the data and codes developed during the project are uploaded to the 4TU data archive:
Zhang, Yuning (2022): Thesis Project. 4TU.ResearchData. Collection
<https://doi.org/10.4121/19766887>

E.0.1 Code

The code part include two project package.

The first one, SpinControl.jl is a Julia package to generate random spin baths system and simulate its dynamics via Monte-Carlo methods. This package contains highly reusable code with well designed interfaces and data structure.

It's published on GitHub, at: <https://github.com/Neuromancer43/SpinControl.jl>.

The "Simulation" folder is a project collection of all the Julia/Python scripts and notebooks used to deploy computation tasks and process the results. This project is less organized compared with the first one. The directories given in this

- data: folder to store all the experiment data.
- explore: folder to store all the Jupyter notebooks for basic exploration.
- out: folder to store exported images and tables.
- plot: folder to store plotting notebooks.
- src: folder for the reusable source code.
- tasks: folder for the data generation scripts.

Here attached a UML diagram describing the architecture of this package, as shown in Fig. E.1.

E.0.2 Data

This data part includes all the numerical simulation results obtained from Monte-Carlo methods. Part of the simulation results are stored in an array of files in .csv format (comma separated values), named by hash strings of corresponding simulation. Other results are stored in .jld format, which is a binary file that can be loaded and processed by the Julia programming language. There is also a set of .siminfo files named with the same hash strings to store the relevant information of corresponding simulation, such like parameter settings and descriptions of tasks. These files are all generated automatically by program, encoded in text format and can be opened with any text editor.

Unified Modeling Language (UML)
Design for SpinEnsemble.jl

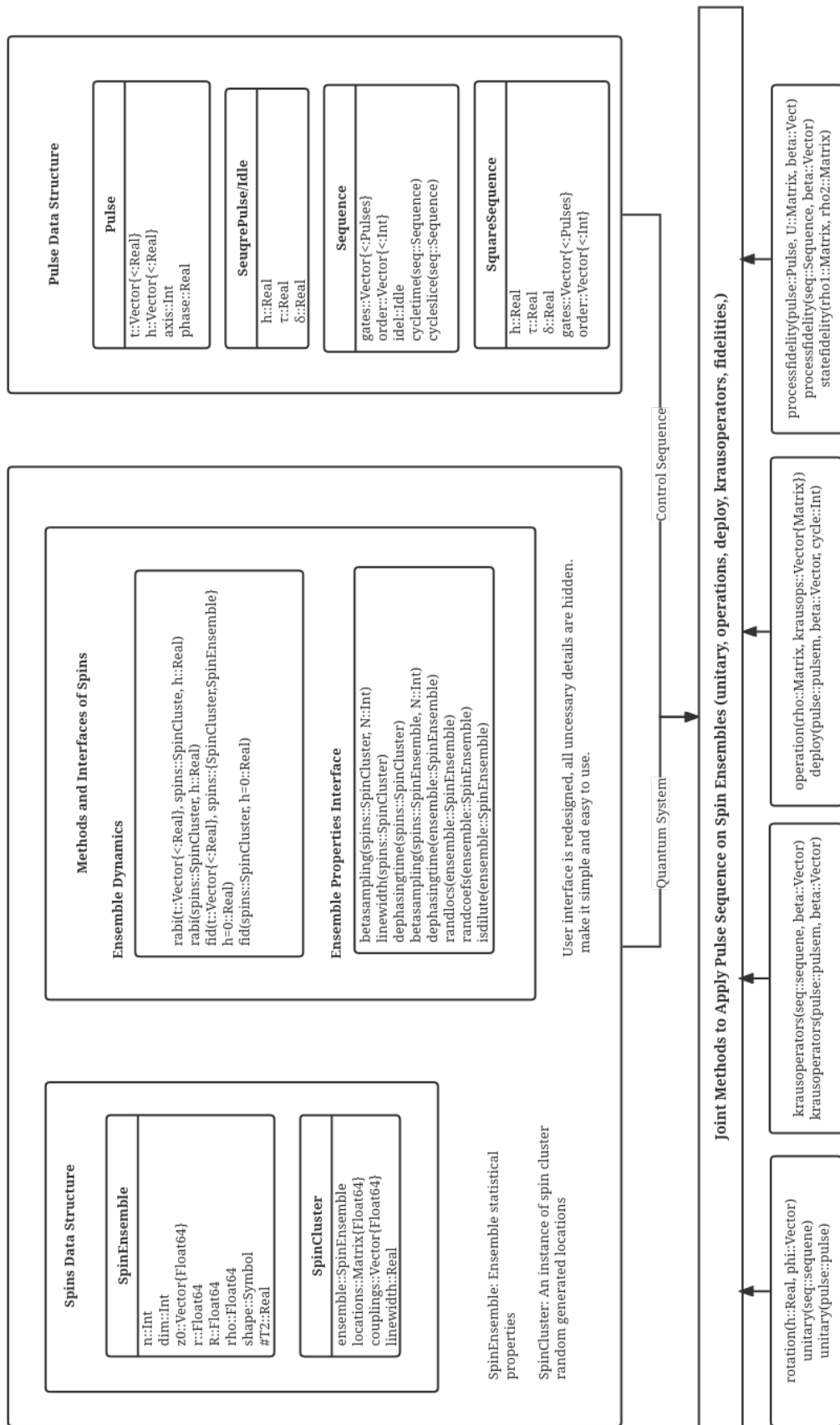


Figure E.1: A UML diagram on the architecture of the software.